Microstructures and Compressive Strength of Lake Ice in Sweden

A structural Documentation and Compressive Strength Analysis of Lake Ice Cores from Uppsala, using the SonReb Method

Julia Ladefoged

Degree of Master of Science (120 credits)
with a major in Earth Sciences
45 hec

Department of Earth Sciences
University of Gothenburg
2023 B1252

Faculty of Science

UNIVERSITY OF GOTHENBURG

UNIVERSITY OF GOTHENBURG
Department of Earth Sciences
Geovetarcentrum/Earth Science Centre

Microstructures and Compressive Strength of Lake Ice in Sweden

A structural Documentation and Compressive Strength Analysis of Lake Ice Cores from Uppsala, using the SonReb Method

Julia Ladefoged

ISSN 1400-3821

B1252
Master of Science (120 credits) thesis
Göteborg 2023

Abstract

Lake ice have been utilized by humans through centuries, as transportation routes and recreational activities to name a few (Sharma et al., 2019). Despite our frequent usage of lake ice there is a lack of extensive knowledge of it.

In contrast to sea ice and continental ice, microstructures of lake ice have been sparsely investigated (Kirillin et al., 2012), and current research lack visual documentations and extensive descriptions. microstructures in lake ice and their relation to compressive strength could increase our understanding of different ice characteristics and mechanical properties of lake ice, and furthermore provide valuable information to minimize the risks of traveling on ice.

This thesis provides a high resolution documentation of microstructures and grain geometries of 5 lake ice cores from 3 different lakes. Furthermore, the thesis explore the possibilities of using the SonReb method to determine the compressive strength of lake ice.

The 5 investigated ice cores display two distinct structural patterns. The first pattern consist of large grained transparent ice with preferred vertical *c*-axis distribution, interpreted as a S1 ice. On top of the S1 ice there is a fine grained opaque ice with randomly oriented *c*-axes, interpreted as a superimposed T1 ice from Michel's(1971) classification. The second type consist of a layered ice with lenses of larger grains with varying sizes, with preferred vertical *c*-axis orientation. The lenses are enclosed in a matrix and alternating layers of a smaller grained ice with a preferred *c*-axis orientation superimposed on a random orientation. No existing formation model can fully explain the observed layered structure, which clearly demonstrates the necessity of further research of microstructures in lake ice.

Due to instrumental complications with the Schmidt hammer and the uniaxial press, only relative uncalibrated strengths could be determined with the ultra sound.

The measurements indicate a slightly larger vertical compressive strength compared to other orientations(30°, 60°, Horizontal, 120° & 150°), as well as an increased strength in litoral samples compared to pelagic ice samples.

Contents

Chapter 1

Introduction

Throughout history, frozen lakes have been a medium of great importance and widely utilized by humans, as fuel for non electrical refrigerators (Desideri et al., 2009), transportation routes and recreational activities, to name a few (Sharma et al., 2019). Still to this day most of us living in a colder environment utilize lake ice whether it is for ice fishing, ice skating or as transportation routes.

Although humans have utilized lake ice for centuries, there is and always will be a certain risk associated with moving on ice. Even with great knowledge of ice conditions, lake ice can be unpredictable and cause severe injuries or deaths. Drownings due to failing ice conditions is unfortunately not unusual, and countries with winter temperatures closer to 0°C are more affected than others (Sharma et al., 2020). Increasing temperatures negatively affect the ice thickness, consequently altering the ice strength. Additionally, recent research indicate increasing temperatures change the ice composition, which also negatively influence the lake ice strength (Weyhenmeyer et al., 2022). Considering the ongoing climate change we can expect increasing winter temperatures in several countries, consequently weakening the strength of ice of numerous lakes.

In broad terms there are mainly two varieties of lake ice, a stronger transparent ice, (also known as black ice, lake ice or congleation ice) and a weaker opaque ice(also known as white ice or snow ice)(Barrette, 2011). With increasing temperatures more opaque ice will form, consequently decreasing the stability of the ice, thus a thicker ice cover is needed for the same stability (Weyhenmeyer et al., 2022). Due to the lack of extensive knowledge of lake ice and the changing ice conditions, there is a potential future risk of increased injuries for people traveling on ice, both experienced and inexperienced. Increasing our understanding of lake ice and their mechanical properties is thus warranted, both as a pursuit of knowledge and to effectively minimize future risk to societal health.

The compressive strength of lake ice have been measured at numerous locations with a wide variety of recorded strengths, from 0.4-14MPa (Michel, 1978). The strength of ice is dependent on several different external and internal factors including, temperature, loading, structures and ice varieties. However, in most strength tests of lake ice a complete description of prevailing ice conditions have not been recorded.

In contrast to sea ice and continental ice, microstructures of lake ice have been sparsely investigated, most documentations are from the 70-80s (Kirillin et al., 2012), with lacking visual documentations. Furthermore, comparisons between microstructures of lake ice and mechanical properties of lake ice are scarce. Further knowledge of microstructures, such as grain geometry and preferred crystal orientations, could add valuable information of different ice characteristics and further aid future investigations of mechanical properties of different ice types.

An additional challenge of measuring the compressive strength of lake ice is the extensive work of ice preparation, as well as transferring large quantities of lake ice to preform compression tests in the lab. There are portable field based equipment to ease this process, however the measurements from these instruments require extensive calculations and assumptions. A possible instrument to further reduce the preparation time and avoid sample destruction could be an Ultra sonic device, which only requires one piece of ice. The instrument measures the P-wave propagation time to determine the compressive strength, however requires calibration from lab based compression tests of lake ice to be a possible contender in field.

1.1 Aim

The aim of this thesis is to provide a high resolution documentation of microstructures of ice cores from 3 different lakes, as well as explore the possibilities to using the SonReb method to determine the compressive strength of lake ice in different orientations. The thesis will thus be separated in to two main sections, a structural documentation followed by an investigation of mechanical properties.

The structural section will provide a high resolution documentation of microstructures of 5 ice cores from 3 different lakes and define different ice types, structures and their significant characteristics. The thesis will also briefly discuss possible formation conditions of observed structures.

The second section will explore the possibilities of using the non destructive SonReb method for determining the compressive strength of lake ice in different orientations as well as the microstructurally investigated ice cores. Possible correlations between the measurements and microstructures will be discussed.

1.2 Ice Crystal Properties

In contrast to most materials, ice have the ability to form various different thermodynamically stable polymorphs (Haji-Akbari, 2020). However, the only stable polymorph on planet earth is ice I, which consists of arranged ice tetrahedons forming layers of hexagonal ice(Ih), as well as occurrences of cubic ice (Ic)(Petrenko & Whitworth, 1999). Thus, the focus of this thesis will be on the crystallographic structures of Ice Ih.

There are two crystallographic axes of the hexagonal ice, the *c*-axis as well as the perpendicular a-axis which extends in 3 directions and form the basal plane (Ramløv & Friis, 2020), see Figure 1.1.

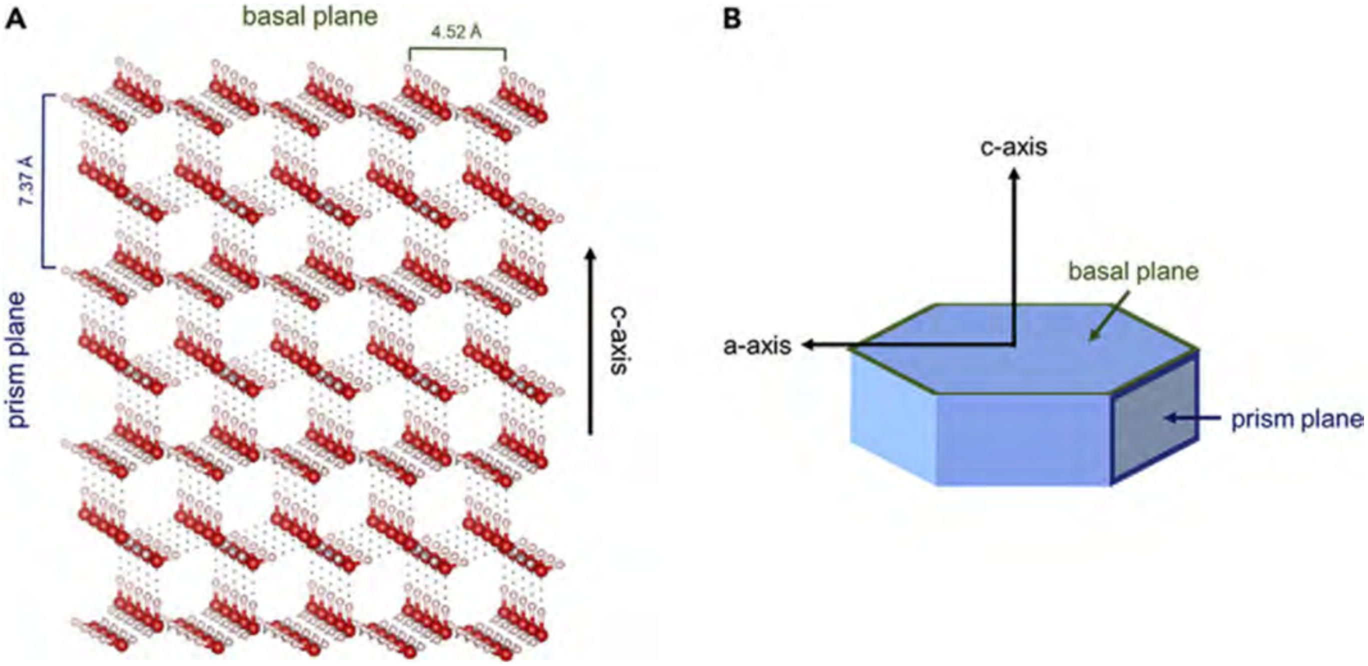

Figure 1.1: A) Crystal lattice of hexagonal ice. B) Hexagonal ice crystal, with indicated *c*-axis, a-axis and basal plane (Delesky & Srubar, 2022).

1.3 Ice Crystal Formation In Lakes

Ice is able to begin crystallization when water becomes supercooled, however a large amount of energy is required for a phase transition from liquid to solid. Consequently water can stay liquid for long periods of time, even when supercooled. Thus, the more frequent process to facilitate this is for the ice to crystallize on nuclei of suspended particles or already crystallized particles, for instance snow (Leppäranta, 2014).

The first crystallized ice, derived from these suspended particles both at the surface, bellow the surface or from already crystallized nuclei, is called primary ice(Leppäranta, 2014). Underneath the primary ice, grains will continue to crystallize parallel to the heat flow, which is usually perpendicular to the primary ice, this is called secondary ice or congleation ice (Michel & Ramseier, 1971). The formation of the secondary ice is completely dependent on the primary ice and can form structures such as columnar ice or snow slush(Michel & Ramseier, 1971). On top of the primary ice a third type of ice can accumulate, superimposed ice, which include snowice, recrystallized melt ponds or flooding covering the primary ice(Leppäranta, 2014)

1.3.1 Ice Varieties

Depending on the water turbulence and temperature gradients, different ice types can crystallize with contrasting characteristics. The most extensive and established river and lake ice classification is from Michel(1971), where he describes the ice and allocate factions based on genesis, ice type(primary, secondary, superimposed), texture and structure. The informal and broad classification of ice as transparent or opaque is originally based on the three ice types, where the transparent ice represent the secondary ice and opaque ice the superimposed ice (Bengtsson, 1986). However, the detailed classification and description from Michel(1971) highlight a wide variety of ice within these ice types, as well as recurrences of ice groups within different types, for instance columnar ice as both secondary and superimposed ice. This could lead to misinterpretations, as the terms is usually referred to as a distinction between snow and slush ice with an opaque appearance and transparent ice with generally large grains, which will be the continued definition of opaque and transparent ice for this thesis.

Michel(1971) describes 4 primary ices; P1 - Calm surface with small temperature gradient, P2 - Calm surface with Large temperature gradient, P3 - Agitated surface and P4 - Nucleation from snow. Where calm surfaces with small temperature gradients produce large grains with preferred vertical c-axis orientations. Calm surfaces with large temperature gradients produce medium to large grains, sometimes with tabular or needle shaped grains, with randomly oriented c-axis orientations. Agitated surfaces produce small, tabular grains with randomly oriented c-axis orientation. Nucleation from snow produce fine to medium grains with randomly oriented c-axis orientation, the properties of the grains are largely dependent on the snow.

Michel also describes 5 secondary ices; S1 - Columnar ice with preferred vertical c-axis orientation, S2 - Columnar ice with preferred horizontal c-axis orientation, S3 - Columnar ice with horizontal parallel preferred c-axis orientation, S4 - Congealed frazil slush and S5 - drained congealed frazil slush.

S1 usually originates from P1 or P2 in lakes with limited movement, the ice consist of large-extra large, irregular grains with vertical c-axes. S2 originates from P2, P3 or P4 and are similar to S1, apart from the more rapidly increasing grain sizes with depth and the preferred c-axis orientation below 5-20cm is horizontal. S3 - mainly occurs at great depths, where columnar grains with dominant c-axes gradually transitions to grains with almost parallel c-axes orientations. S4 - Originate in agitated waters and form fine to medium tabular or equiaxed grains with random c-axis orientation. The ice can form a separate unit or as layers in between columnar ice. S5 - originate from water drained ice which refreezes and form fine to medium angular grains. There are different frazil ice shape characteristics, the most common varieties include discoids $\leq$ 1mm, needles and pancakes. Needles form in water with relatively low turbulence (Hanley & Rao, 1982). Pancake ice is the result of smaller sheets of frazil slush bumping in to each other, due to slower movement of the ice relative to the water beneath, producing circular ice sheets with slightly upward tilting edges (Ashton, 1986).

Experimental studies from (Gow, 1986) demonstrate that S2 ice form when seeding of frozen nuclei have occurred, however if no seeding occur S1 ice will form. Strongly indicating the c-axis orientations in calm lakes are influenced by meteorological conditions. This is supported by (Müller-Stoffels et al., 2009).

Furthermore Michel(1971) describes 3 superimposed ices; T1 - Snow-ice, T2 - Drained snow-ice and T3 - Surface ice. T1 - originates from accumulating snow on top of the ice which gets water saturated and freeze. The crystals are fine to medium grained equiaxed with random c-axis orientation. T2 - Originate from snow which have been repeatedly drained and recrystallized. The grains are fine to medium rounded and the ice is usually very homogeneous with randomly oriented c axes. T3 - Columnar ice produced on top of the primary ice.

Lastly Michel describe a separate group of Agglomerate ice, which usually originates from turbulent water and consists of refrozen ice segments, which means there is a substantial variety of grain shapes and sizes.

Michel concludes the factors determining the ice type is primarily dependent on temperature, wind and nucleation mode.

1.4 Mechanical Properties of Lake Ice

The following section will address the mechanical properties of lake ice, with a focus on the load-bearing strength and the SonReb method.

The strength of ice is defined as the maximum stress ice can support prior to ice failure. There are two different modes of failure, brittle, where the applied stress induce an abrupt breakage releasing all stress as a fracture, and ductile, where the strain of the ice increase even when the applied stress remain constant or decrease (Michel, 1978; Ashton, 1986).

The compressive strength is usually determined with a uniaxial compression test, where a cylindrical, cubic or prismatic sample is exposed to an increasing load until failure is reached, the maximum load represent the strength of the ice, however due to friction it is difficult to conduct a completely uniaxial compression test without any segments influenced by triaxial compression (Schwarz et al., 1981). To ensure reliable data the friction can be minimized by using a lubricant and several specimens needs to be tested.

Investigations of lake ice using variations of uniaxial compression tests indicate a generally increasing strength of ice with temperature, as well as a larger vertical strength than horizontal strength (Lian et al., 2017). These trends have been observed in both opaque ice and transparent ice, however the difference of vertical and horizontal strength is significantly larger in transparent ice (Butkovich, 1954b, 1954a). Depending on temperature, sample size, orientation and ice type the compressive strength can range from 0,4-14MPa.

An additional factor influencing the uniaxial compressive strength of natural ice is the amount of impurities, such as bubbles, which negatively affect the strength (Qi, Lian, Ouyang, & Zhao, 2017).

Additionally to the traditional lab situated tests, there are a few field based methods for determining ice strength, for example Flaking strength, which measures compressive strength of edge loading (Kivisild & Iyer, 1976), Borehole jack, an instrument which is lowered into a borehole and puts pressure against the ice walls to measure the strength (Masterson, 1996), and Pressuremeter, where a metal cylinder covered with an expandable membrane is lowered into a borehole and measures the fluid pressure needed to expand the membrane (Murat et al., 1989).

There are however certain limitations and difficulties with these methods, Flaking strength can only be used near the surface, Borehole jack measures the horizontal strength not the vertical strength, and the Pressuremeter require several assumptions and post-processing calculations.

In bedrock sciences another method of measuring strength is the nondestructive SonReb method, which combines the P-wave propagation time, measured with the ultra sonic, and the rebound number, determined with the Schmidt hammer (Selçuk & Nar, 2016). The method is both nondestructive and only requires a relatively small specimen, however the measurements also require a calibration curve derived from compression tests of a similar material.

Using the SonReb method for lake ice could possibly be a great in situ method to determine the compressive strength of ice.

Ultra sonic pulse methods have been used in several previous lake ice investigations, although primarily with the focus of determining ice thickness and to calculate elastic constants for both single crystals (Green Jr & Mackinnon, 1956) and polycrystaline ice (Brockamp & Querfurth, 1964; Roethlisberger, 1966). Recent investigations of glacial ice have also attempted to use the ultra sonic to determine the crystal orientation fabric, with predominantly positive results, however not yet enough to replace existing COF analyses (Hellmann et al., 2021).

The SonReb method could be an additional way of utilizing ultra sound. Additionally, the compressive strengths of lake ice have been widely recorded and related to different ice conditions, these measurements could be useful to determine suitable calibration curves for a variety of different circumstances. However, comprehensive testing is necessary to evaluate the suitability of using this method on lake ice.

Chapter 2

Method

2.1 Ice Core Sampling

For the microstructural analyses 5 cores were investigated, the cores were collected from three different lakes in Uppsala and Stockholm municipality. For the mechanical properties, 15 additional ice blocks were collected from an adjacent lake, see Figure 2.1.

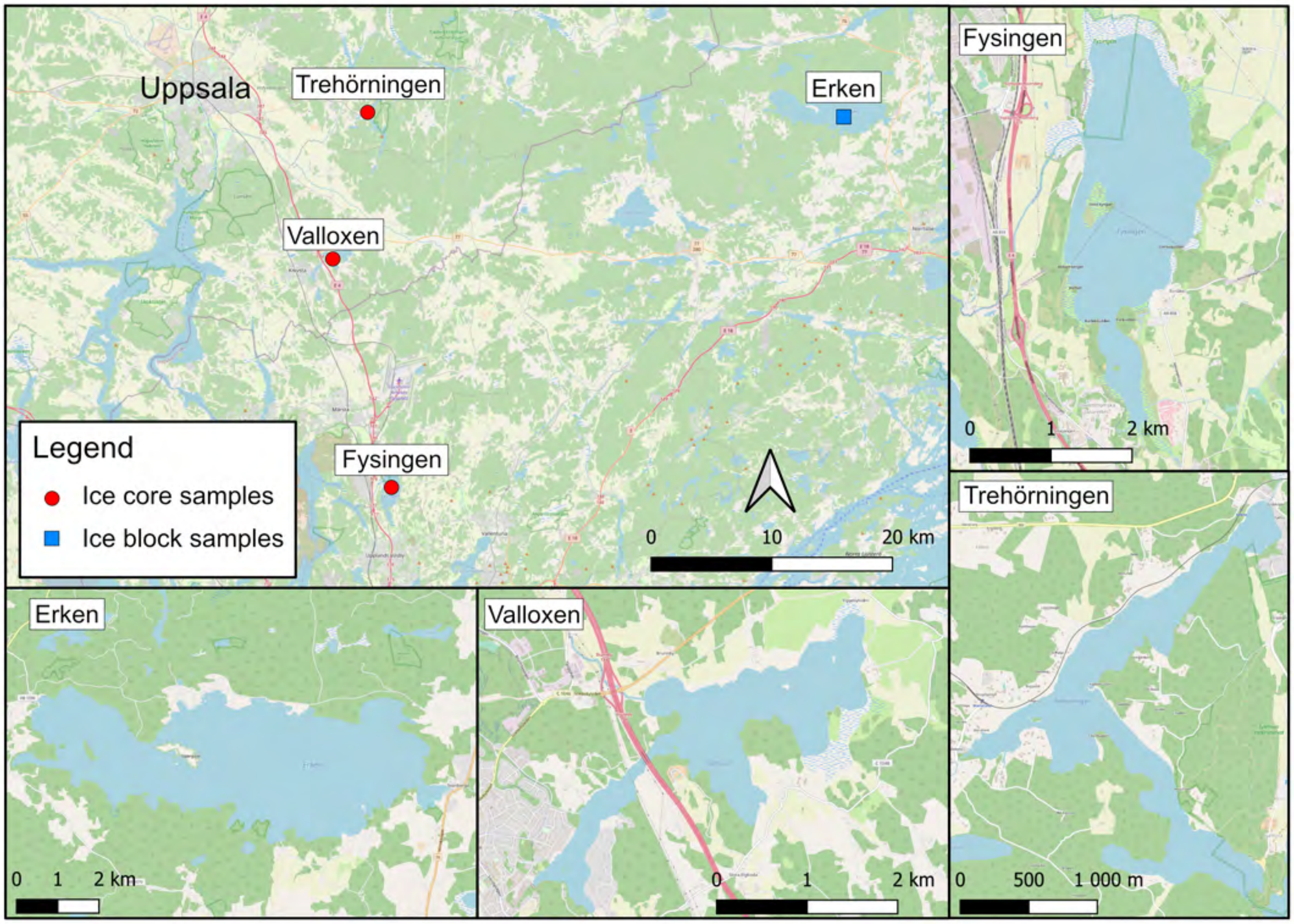

Figure 2.1: Map of sample locations, red circles represent sample locations for the ice core and the blue square represent the sample location for the ice blocks.

The ice cores were drilled and collected by Ellinor Jakobsson and Carina Liebl in spring 2022. The cores were wrapped in aluminum foil as well as plastic foil, during transportation to Gothenburg the cores were preserved in a -18°C (±1°C) environment. Upon arrival to Gotheburg the cores were continuously stored in a -35°C environment prior to the micro stuctural investigation. Due to difficulties with drilling equipment, different radius of ice cores were collected.

The ice blocks were collected in spring 2023, from 2 localities from lake Erken. Similarly to the ice cores, the blocks were wrapped in aluminum foil as well as plastic foil and during transportation to Gothenburg the cores were preserved in a -18°C (±1°C) environment.

The following ice cores and blocks have been collected, see Table 2.1

Table 2.1: Overview of collected samples, the first five entries represent ice cores and the lower two ice blocks

Location ID	Location	Locality	Date	Diameter	Dimensions(bxhxl)	Number of samples
Trh 1	Trehörningen	Pelagic	22-02-12	7cm	-	1
Trh 2	Trehörningen	Litoral	22-02-12	7cm	-	1
VO	Valloxen	Litoral	22-02-12	5cm	-	1
Fys 1	Fysingen	Pelagic	22-02-12	5cm	-	1
Fys 2	Fysingen	Litoral	22-02-12	5cm	-	1
E 1	Erken	Pelagic	23-02-14	-	10x10x23cm	7
E 2	Erken	Litoral	23-02-14	-	10x10x23cm	9

The investigated ice cores and ice blocks were collected from 4 different lakes in Uppsala- and Stockholm municipality. The lakes are considerably different in size ranging from the smallest lake Trehörningen to the largest lake Erken, see Table 2.2. The lakes are at relatively close proximity to each other and during the winter season 2022 Trehörningen, Valloxen and Fysingen had a similar climate, with identical number of days with precipitation as well as days below 0°C, see Figure 2.2.

Table 2.2: Overview of lake properties (SMHI & HavsVatten myndigheten, n.d.)

Lake	Max Depth	Average Depth	Lake Area	Lake Volume
Trehörningen	6.2m	3.2m	1.268km^2	4 700 000m^3
Valloxen	9.1m	3.8m	2.7882km^2	11 100 000m^3
Fysingen	4.5m	2m	4.896km^2	10 000 000m^3
Erken	20m	9.1m	23.2km^2	210 800 000m^3

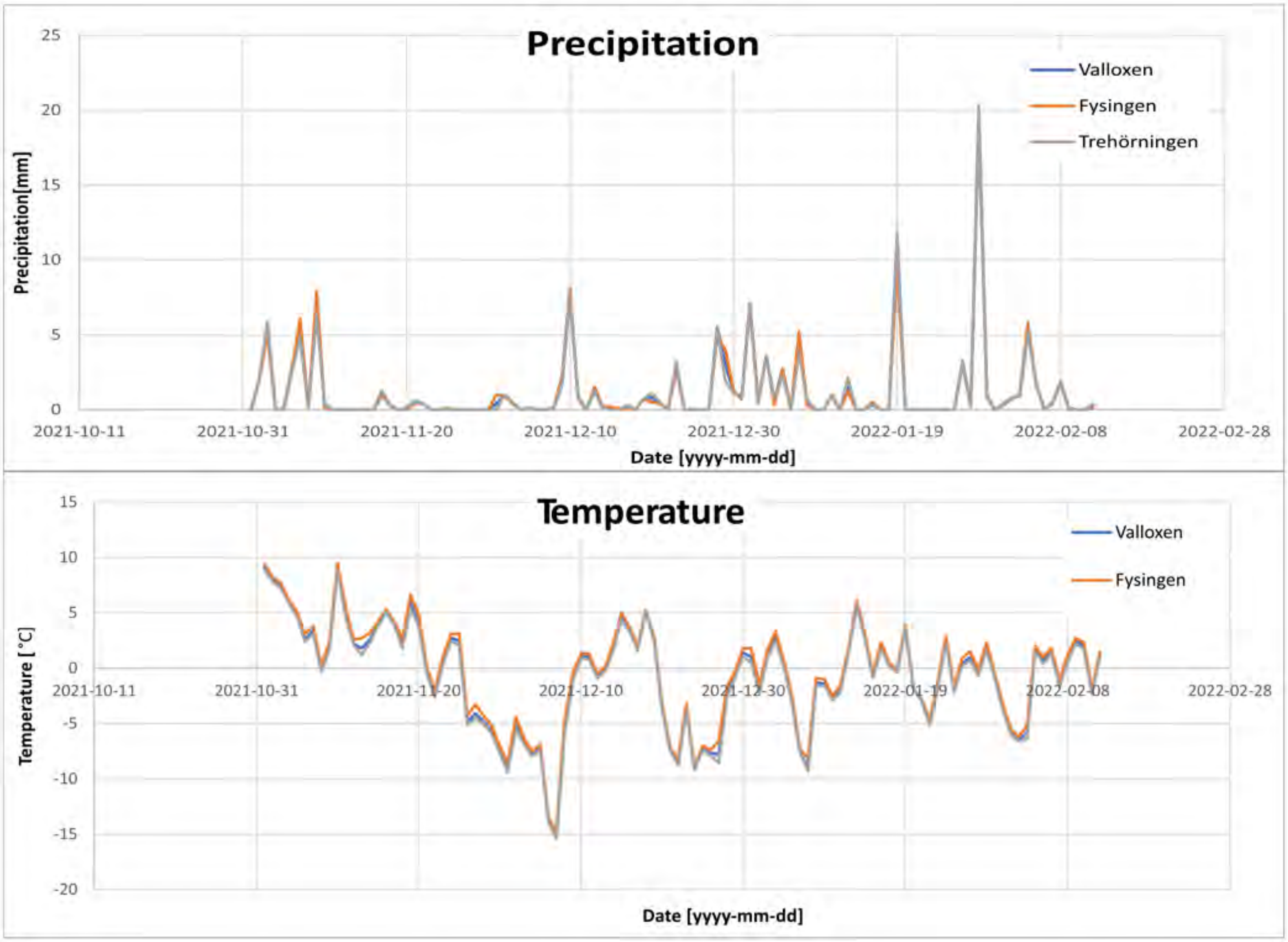

Figure 2.2: Precipitation and temperature data from weather stations nearby lake Valloxen, Trehörningen and Fysingen, during the winter season 2021-2022 (SMHI, n.d.).

2.2 Microstructural Documentation & Thin Sections

In conjunction to the P-wave propagation time measurements, structures and lengths of each segment of all cores were recorded. From this documentation, a log for respective ice core could be produced and suitable locations could be selected for thin sections.

From each core, 4 thin sections were produced, a horizontal slice from the opaque ice, a vertical slice from the opaque ice/transition zone, a horizontal slice from the transparent ice and a vertical slice from the transparent ice, see Figure 2.3. 3 of the cores did not have a distinct layer of opaque ice or a transition zone, in those instances thin sections were produced from segments as close to each ice core edge as possible.

The thin sections were produced by sawing thick ice sections from the cores and attaching the ice sections to glass plates. Each thick section was thereafter shaved with a microtome to obtain a perfectly smooth surface, see Figure 2.4. The even surface was attached to another piece of glass by slightly heating up the surface with a heating table at a temperature of ca 23-25°C, which corresponds to approximately 1-3°C on the glass surface. The heat will melt a segment of the ice crystals, however not the whole crystal, thus the most accessible way for the ice to recrystallize is in their original position. Thereafter, the first glass plate was heated up and removed. Furthermore, the ice was polished with sandpapers of various grain sizes (80-300mm), and lastly shaved with the microtome to a thickness of 250-400 microns.

The final thin sections were analysed in a G60 fabric analyser. The G60 fabric analyser is a polarizing light microscope, which can produce a set of high resolution images (5.08-20µm/pixel)(Peternell et al., 2009; Wilson et al., 2007; Peternell et al., 2011). For this thesis a set of 8 images were produced, PPL - plain polarized light, lambda, XPL - cross polarized light, orientation of the c-axis, trend of the c-axis, retardation, GQ - geometric quality, RQ - retardation quality, see Figure 2.4C-J. Most images were shot with a resolution of 20µm/pixel, however thin sections with fine grained matrices were shot with a resolution of 5.08µm/pixel.

The analyzer contains one light source connected to a prism, acting as a light source in different directions. Furthermore, the analyzer includes 2 polarizers which automatically rotate. By combining the rotating polarizers a set of 18 images is produced for each light source direction. Each image contains a plane with the c-axis and by overlapping these images, the intersection point of the planes indicate the c-axis orientation (Peternell et al., 2009; Wilson et al., 2007; Peternell et al., 2011). Depending on the similarity of the planes the quality of c-axis orientation can vary, where similar planes indicate a high quality(100) and scattered planes low quality(0). This parameter is visualized in the geometric quality image.

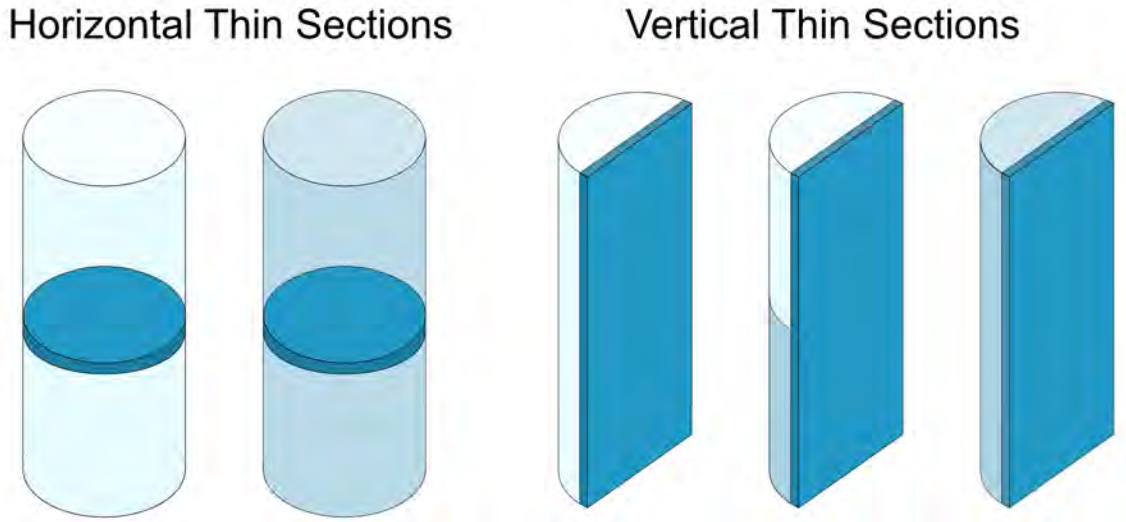

Figure 2.3: Schematic picture of the produced thin sections, where the dark blue sections illustrates the thin sections. From left to right; horizontal thin section through opaque ice, horizontal thin section through transparent ice, vertical thin section through opaque ice, vertical thin section through a transition zone from opaque ice to transparent ice & vertical thin section through transparent ice.

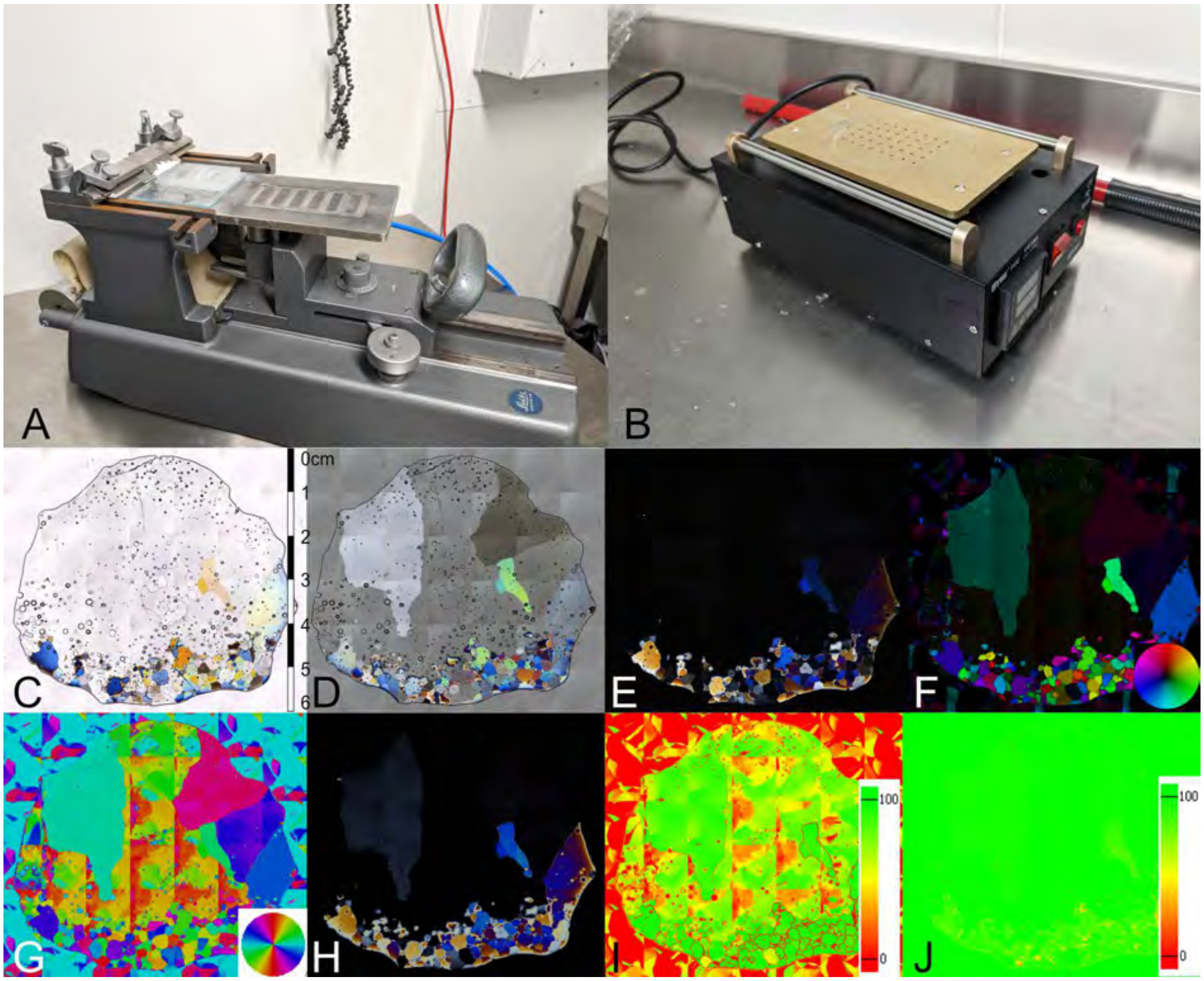

Figure 2.4: A) Photograph of the Microtome. B)Photograph of the heating table. C-J)The produced set of images from the fabric analyser G60. C) Plain polarized light. D) Lambda. E) Cross polarized light. F) *c*-axis orientation. G) *c*-axis trend. H) Retardation. I) Geometric quality. J) Retardation quality.

2.3 Data Processing

To obtain statistical data of both *c*-axis orientations and grain geometry, a variety of software programs were used to process and analyse the high resolution images, see Figure 2.5.

The *c*-axis orientations were analysed in the investigator software and plotted in stereonets.

Prior to the grain geometry analysis, the grains from the images were modelled in the FAME software and noise from the thin sections were removed in Adobe Photoshop. The grain geometry could then be analysed in ImageJ and presented in diagrams and rosediagrams.

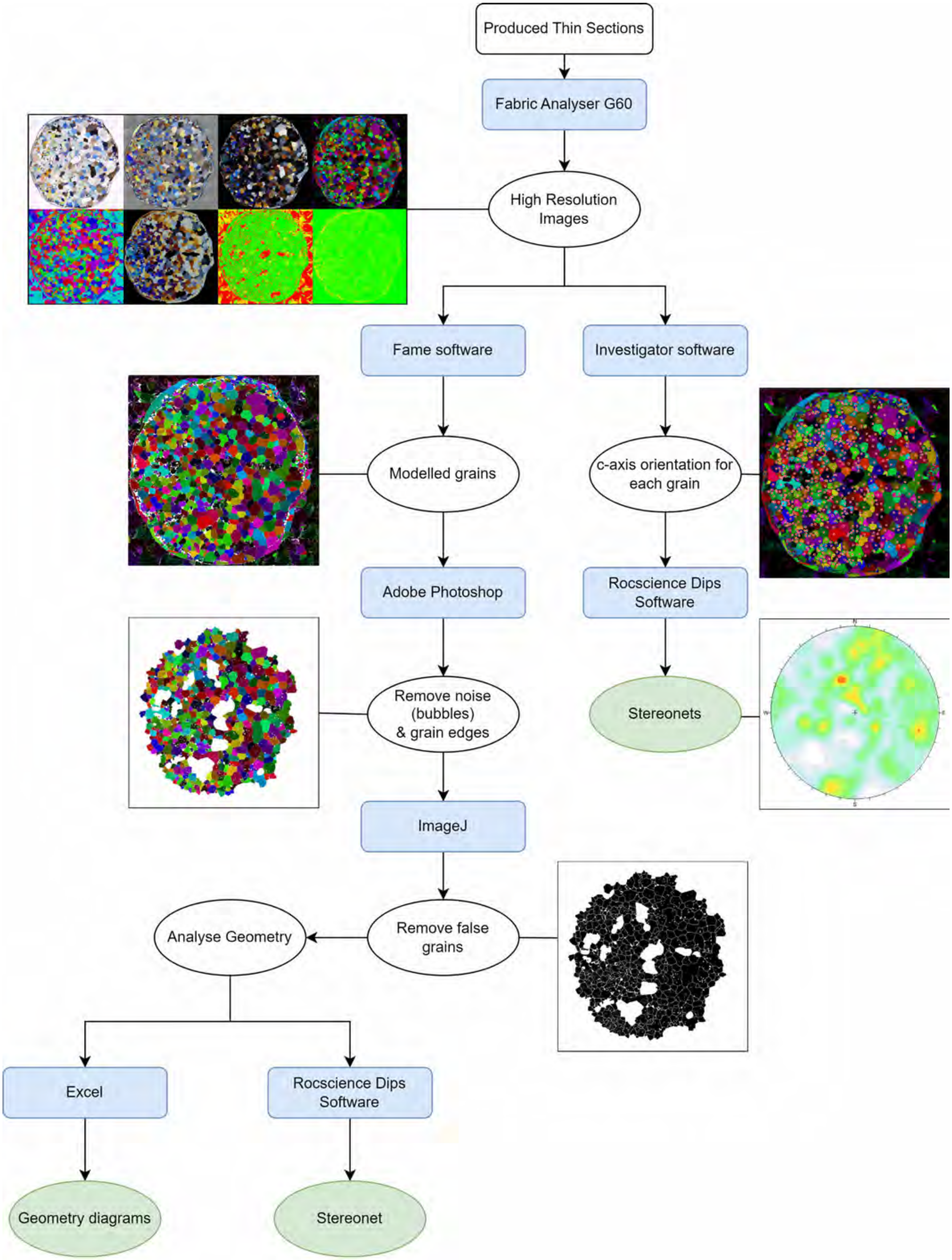

Figure 2.5: Overview flowchart of the processing procedure of the *c*-axis orientation analysis and the grain geometry analysis. The blue boxes represent software and the ovals represent the operations done in the software.

2.3.1 *c*-axis Orientation Analysis

Initially, the Investigator software was used to obtain the *c*-axis orientations for each grain from the produced *c*-axis orientation images. The grains were manually selected and divided into groups of small(<3mm$^{\mathbf{2}}$), medium(3-40mm$^{\mathbf{2}}$) and large grains(>40mm$^{\mathbf{2}}$). For thin sections with a very fine matrix a smaller area was scanned with a higher resolution(5,08µm/pixel), which was used to represent the whole matrix.

The colour and shade of each grain corresponds to a point in the colour wheel, which also represents a point in the projection plane in a stereonet. Thus, each colour indicate a linear feature in a stereographic projection, with a trend and plunge. The *c*-axis orientations could therefore be plotted in stereonets with the Rocscience Dips software, with separated stereonets for different grain sizes and sections, see Figure 2.6.

In order to produce directly comparable stereonets for both vertical and horizontal thin sections, the *c*-axis orientations from the vertical thin sections were rotated 90° around the E-W axis, into the reference frame of the horizontal sections. Accordingly, the center of all plotted stereonets represent the vertical z-axis, see Figure 2.7.

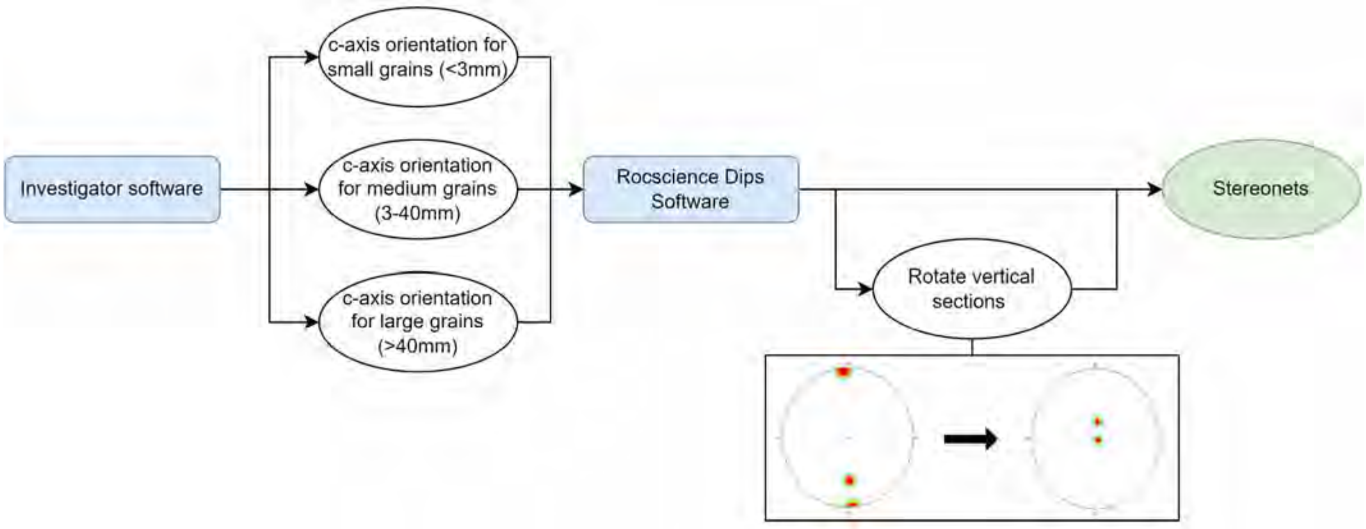

Figure 2.6: Flowchart of the processes used for the analysis of the *c*-axis orientation images. The blue boxes represent software and the ovals represent the operations done in the software.

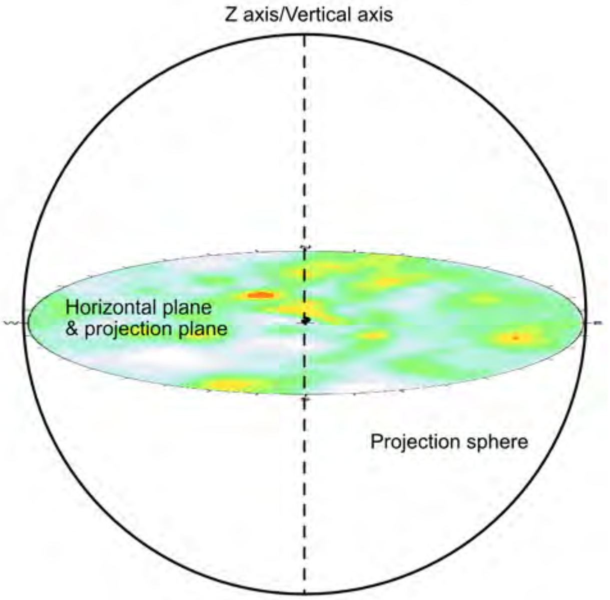

Figure 2.7: Illustration of the orientation of the stereonet projection which is used for all thin sections. The coloured area show the horizontal projection plane and the dotted line indicate the z-axis through the center of the projection plane.

2.3.2 Grain Geometry Analysis

In order to perform the grain geometry analysis, the grains required prior processing.

Firstly the grains were modelled in the Matlab based Fame software (Hammes & Peternell, 2016) from the *c*-axis orientation images. Different combinations of angle criterion, minimum grain radius, grain growth and angle threshold was tested in order to produce a grainmap similar to the original image. Once a finished grainmap was completed noise was removed from the grainmap, which had been manually selected in Adobe Photoshop from the high resolution images. This includes bubbles larger than 5 pixels and grains bordering the perimeter which might be affected by melting and thus creating grains with inaccurate geometry. However, it is important to note the difficulty of distinguishing bubbles from organic material and condensation, which might influence the results.

The modelled grainmaps could thereafter be processed in the software ImageJ. Initially the grains were adjusted to the same colour by processing the image in three steps, and in order to fully distinguish the grains, the grain boundaries required to be dilated by one pixel. To ensure no false grains generated from the FAME software were analysed, grains with an area smaller than 0.1mm^2 and grains with an elongation larger than 0.9 were removed.

Following the grainmap processing, the grain geometry was preformed in ImageJ, the analysis generated the following parameters; Grain area, Area equivalent circle diameter - the diameter of a circle with the corresponding area as the grain, Elongation - the elongation of a grain where 0 represent a circular grain and 1 is a very elongated grain, Holes/area - the number of holes i.e the manually selected bubbles divided by the area, Aspect ratio - longest axis compared to the shortest axis of the grain, Thinnes ratio - the roundness of a grain which is determined by the ratio of area compared to the perimeter, and grain orientation - the orientation of the major axis of each grain.

Lastly, all parameters except the grain orientations were prepared and plotted in diagrams, while the grain orientations were plotted in a rosediagram with the Rocscience Dips software.

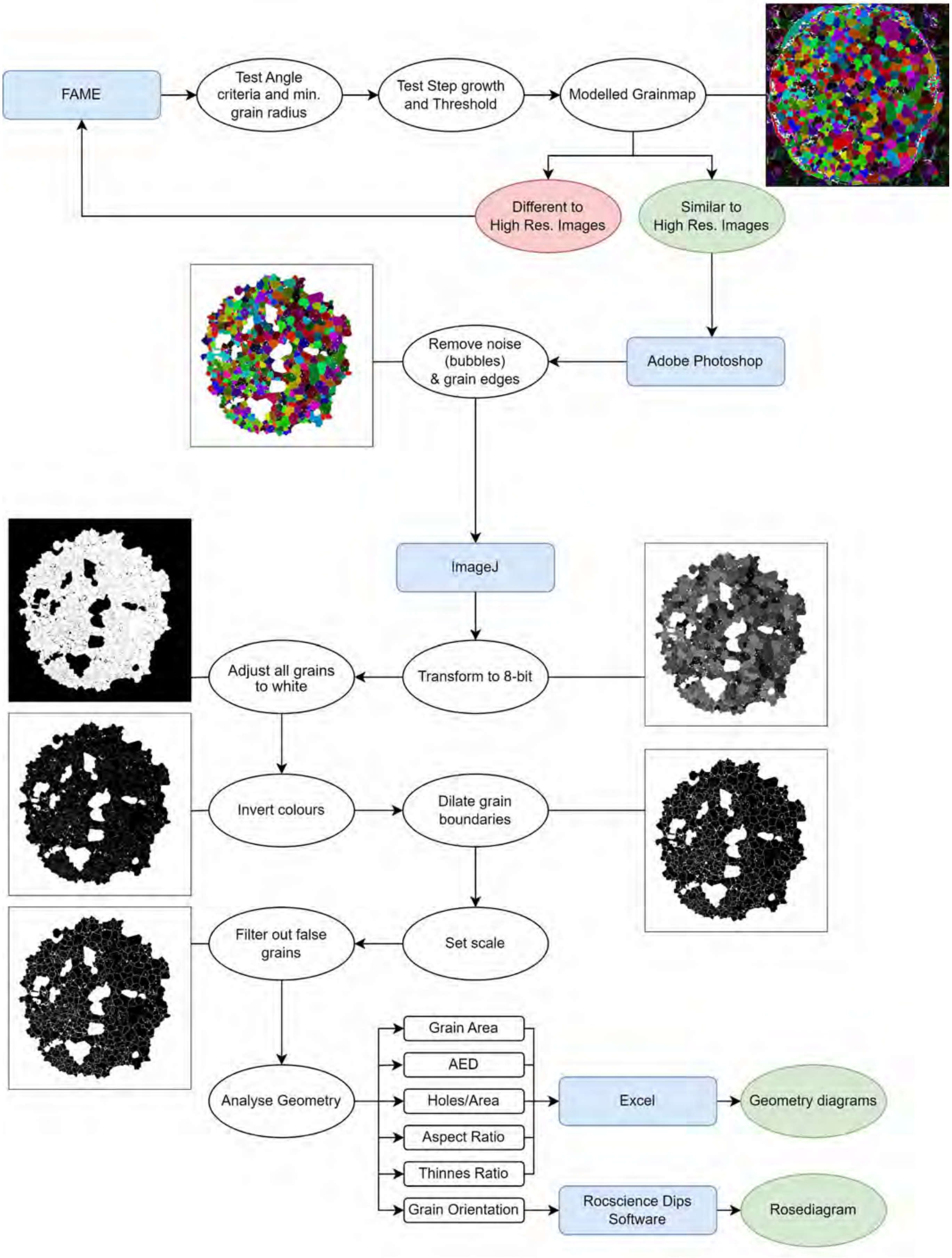

Figure 2.8: Flowchart of the processes used to analyse the grain geometry. The blue boxes represent software and the ovals represent operations done in the software.

2.4 Mechanical Properties of the Ice Cores

For the mechanical properties, the vertical P-wave propagation time through each core segment was measured with the Pundit 200 Ultrasonic pulse velocity instrument. Due to equipment complications, neither Schmidt hammer nor a Uniaxial press was possible to use for calibration of the P-wave propagation time. Thus, the absolute strength could not be determined and the thesis will only compare the uncalibrated compression strengths.

Prior to measuring, the length of each segment was recorded and smooth surfaces were polished on both sides of each segment. The ice core segments were split into 3 groups, opaque ice, transparent ice and segments with a transition zone of both opaque ice & transparent ice. The transition segments were firstly measured and thereafter split into opaque and transparent ice, and additionally measured respectively. However, most cores had very thin sections of opaque ice (<5cm) including the transition zone segments, which entailed a significant restriction since segments less than 5cm were not possible to successfully measure. Consequently, only segments with transparent ice and transition zones were measured in affected cores.

To measure the vertical P-wave propagation time both the 54kHz exponential transducers and the 54kHz transducers were used. As the 54kHz exponential transducers were optimal for a reliable contact surface, however they were not capable of successfully measure segments thinner than 8cm. In contrast, the 54kHz transducers could measure down to a thickness of 5cm, although a reliable contact surface was difficult to achieve. Thus, both transducers were used to complement each other.

2.5 Mechanical Properties of the Ice Blocks

To determine the P-wave propagation time through different orientations of lake ice, cubes of ice were measured with the Pundit 200 Ultrasonic pulse velocity instrument. However, similarly to the mechanical properties of the ice cores, the absolute compressive strength could not be determined due to equipment complications.

Firstly, the acquired ice blocks were sawed in to 5x5x5cm cubes. To determine the P-wave propagation time in different orientations, 4 cubes in 4 different orientations were produced from each locality; vertical, horizontal, 30°, 60°, 120° and 150°, see Figure 2.9. The P-wave propagation time of each cube was measured with the Pundit 200 Ultrasonic pulse velocity instrument and the 54kHz transducers. The average of 10 measurements from each orientation and locality was used. All Ultra sonic measurements of the ice cubes were conducted with an ice temperature of -17°C.

The P-wave propagation time can be calibrated with lab based compression tests and rebound number to determine the absolute compressive strength. However, due to equipment complications, measurements from the Schmidt hammer and the Uniaxial press were unusable. The impact energy of the Schmidt hammer was to large and destroyed the samples, while the uniaxial press had a measuring range larger than the scope of the ice strength. Hence, this thesis will only compare the relative uncalibrated compressive strengths for different orientations.

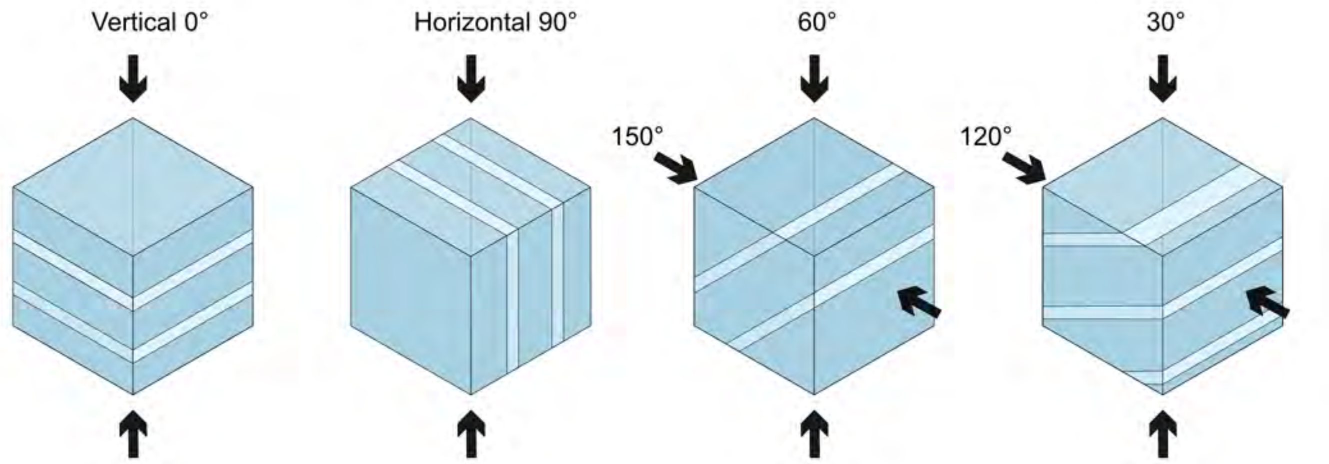

Figure 2.9: The orientations used for the Ultra sonic measurements of the cubes.

Chapter 3

Results

3.1 Microstructures

The pelagic ice core from Trehörningen was 36.1cm and was detached in 4 segments. The first segment consisted of a thin layer(4.5cm) of opaque ice with small grains and layers of slightly finer crystals, followed by a layer of transparent ice with large crystals, see Figure 3.1. The remaining segments also consisted of transparent ice with very large crystals.

The litoral ice core from Trehörningen was 30.2cm and was detached in 8 segments. Similarly to the pelagic Trehörningen 1 ice core, the first segment consisted of a thin layer (4cm) of opaque ice with small grains and layers of slightly finer crystals and bubbles, followed by a layer of transparent ice with large crystals, see Figure 3.2. The remaining segments also consisted of transparent ice with very large crystals.

The litoral ice core from Valloxen was 42.7cm long and was detached in 9 segments. The first segment consisted of transparent ice with large crystals. However, the following segments were mostly layered ice, where lentils of larger crystals were surrounded by a matrix of smaller grains, see Figure 3.3. The sizes of the lenses varied slightly and ranged from 0.5-1.5cm. At the base of the core there was also a segment with opaque ice with smaller grains and fragments of organic material.

The pelagic ice core from Fysingen was 41.7cm long and was detached in 3 segments. All of the segments consisted of layered ice, where lentils of larger crystals were surrounded by a matrix of smaller grains. The lentils ranged from 0.5-2cm, with thinner lentils at the top of the core and larger crystals towards the base, see Figure 3.4.

The litoral ice core from Fysingen was 36.3cm long and was detached in 5 segments. The first segment consisted of transparent ice with large crystals and the following segments consisted of layered ice, where lentils of larger crystals were surrounded by a matrix of smaller grains, see Figure 3.5. The lentils ranged from 1-3cm, with thinner lentils at the base of the core and slightly thicker lentils towards the top.

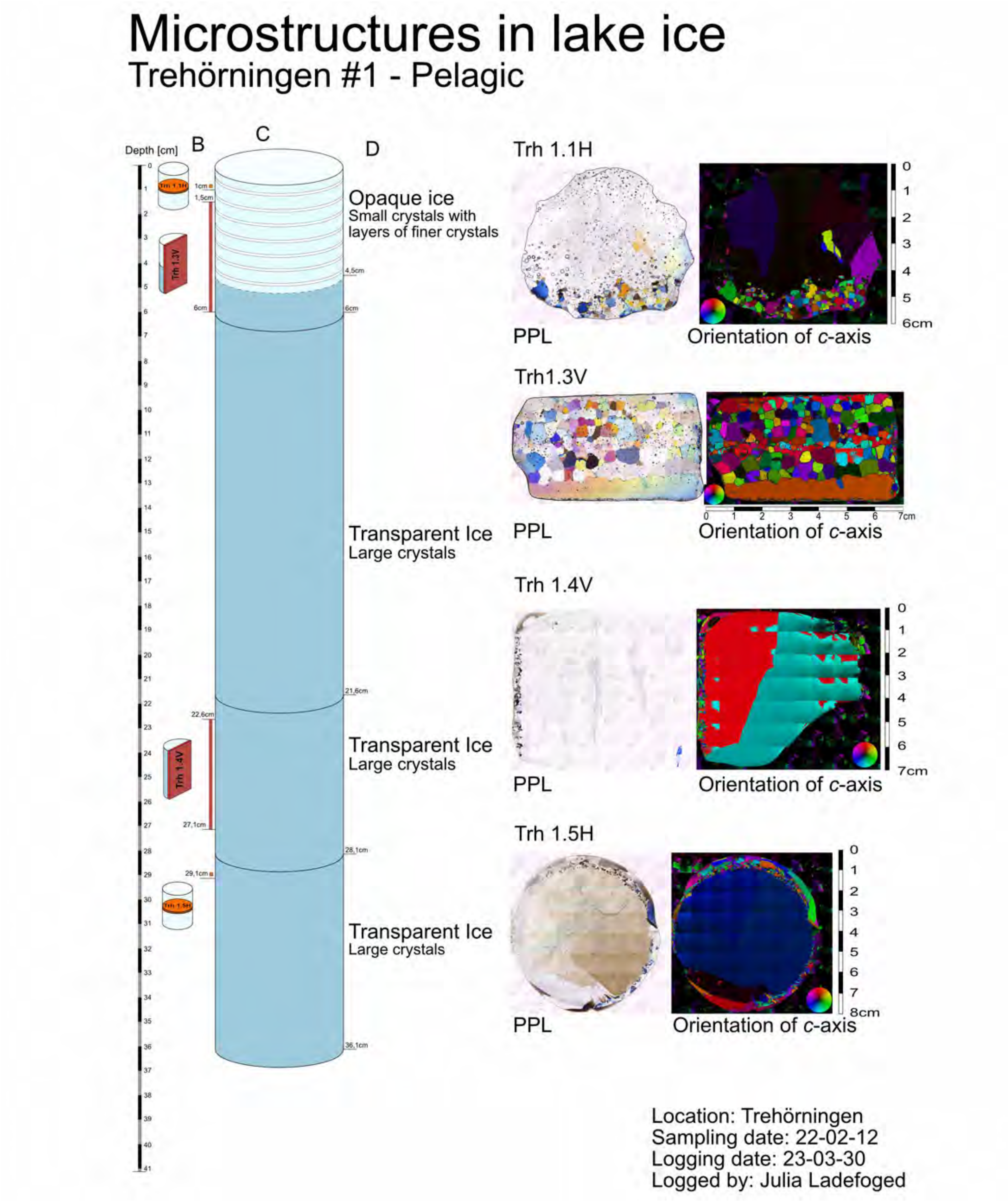

Figure 3.1: Illustrated representation of the Trehörningen #1 ice core. A) The location samples were retrieved from. B) Illustrated representation of the ice core. c) Brief description of the ice core units. D) A plain polarized light(PPL) photo and a *c*-axis orientation photo from each sample.

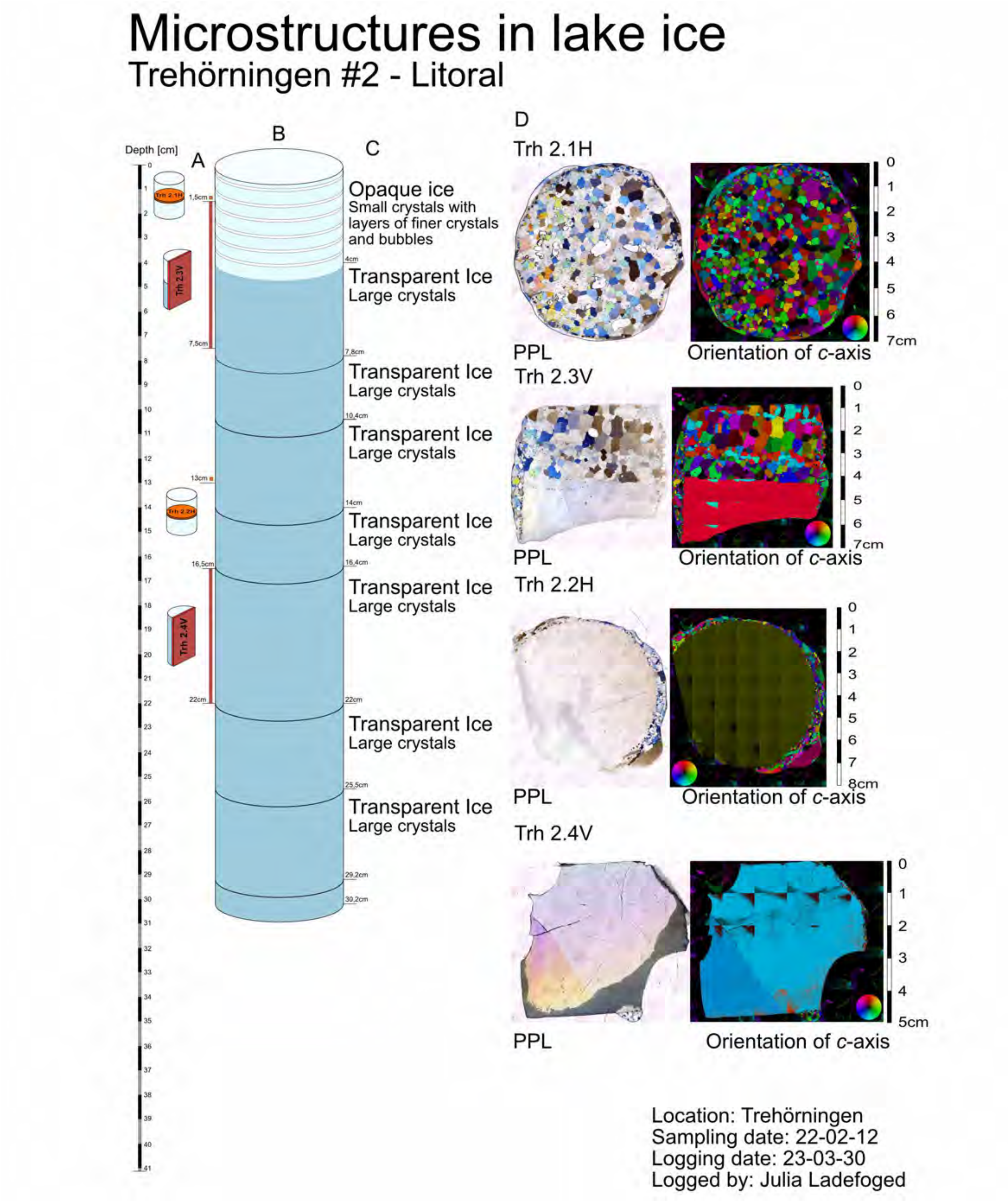

Figure 3.2: Illustrated representation of the Trehörningen #2 ice core. A) The location samples were retrieved from. B) Illustrated representation of the ice core. c) Brief description of the ice core units. D) A plain polarized light(PPL) photo and a *c*-axis orientation photo from each sample.

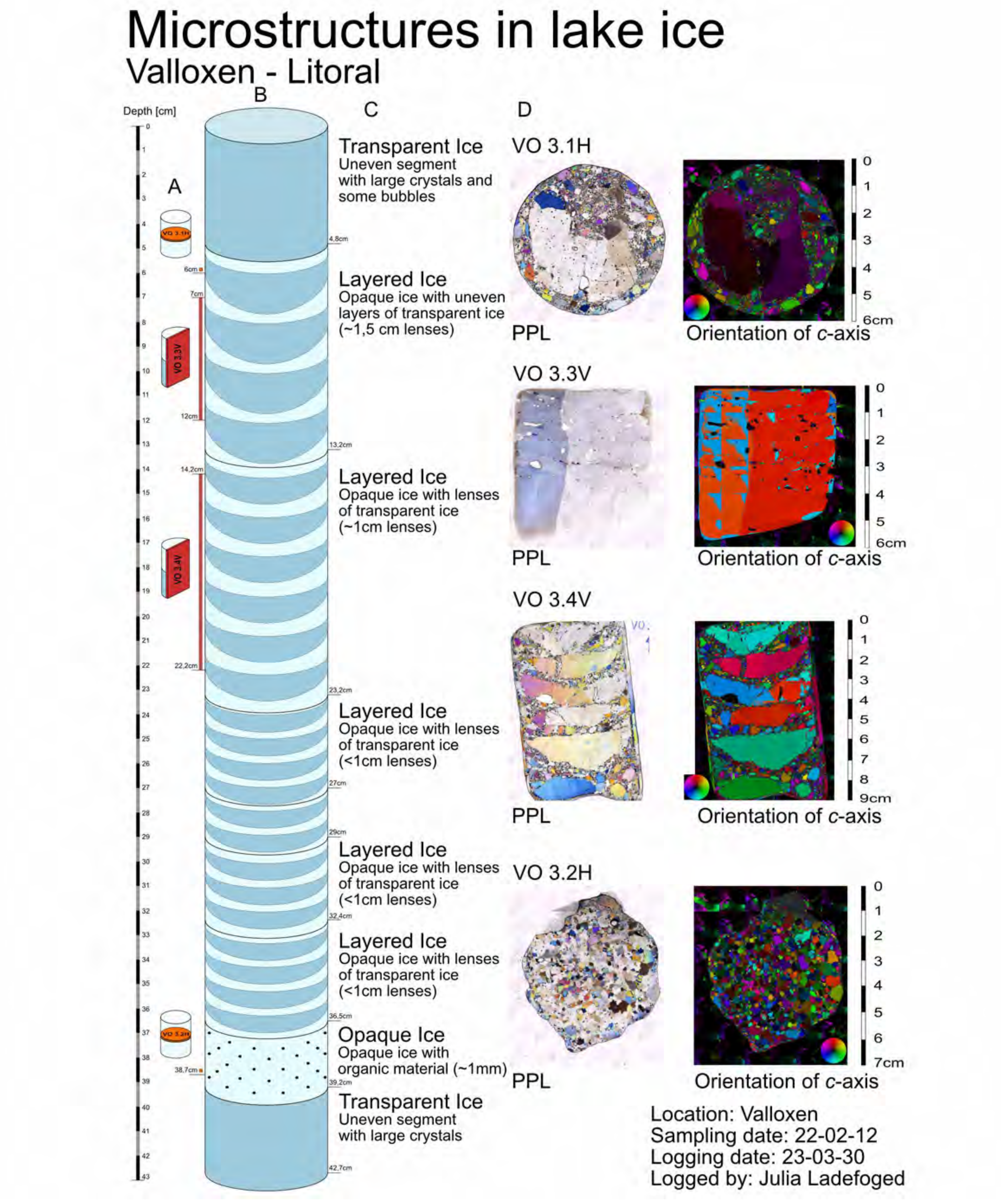

Figure 3.3: Illustrated representation of the Valloxen ice core. A) The location samples were retrieved from. B) Illustrated representation of the ice core. c) Brief description of the ice core units. D) A plain polarized light(PPL) photo and a *c*-axis orientation photo from each sample.

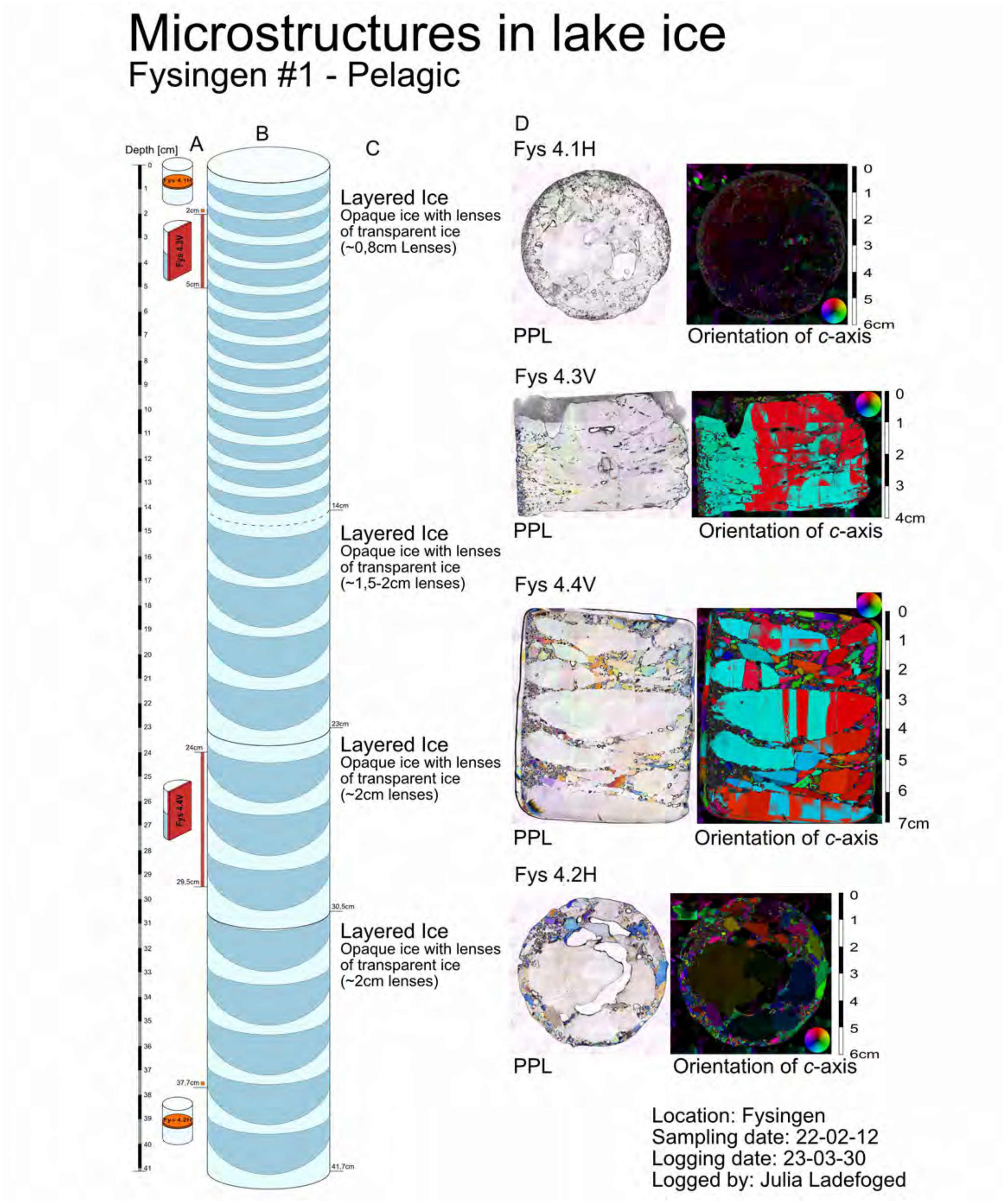

Figure 3.4: Illustrated representation of the Fysingen 1 ice core. A) The location samples were retrieved from. B) Illustrated representation of the ice core. c) Brief description of the ice core units. D) A plain polarized light(PPL) photo and a *c*-axis orientation photo from each sample.

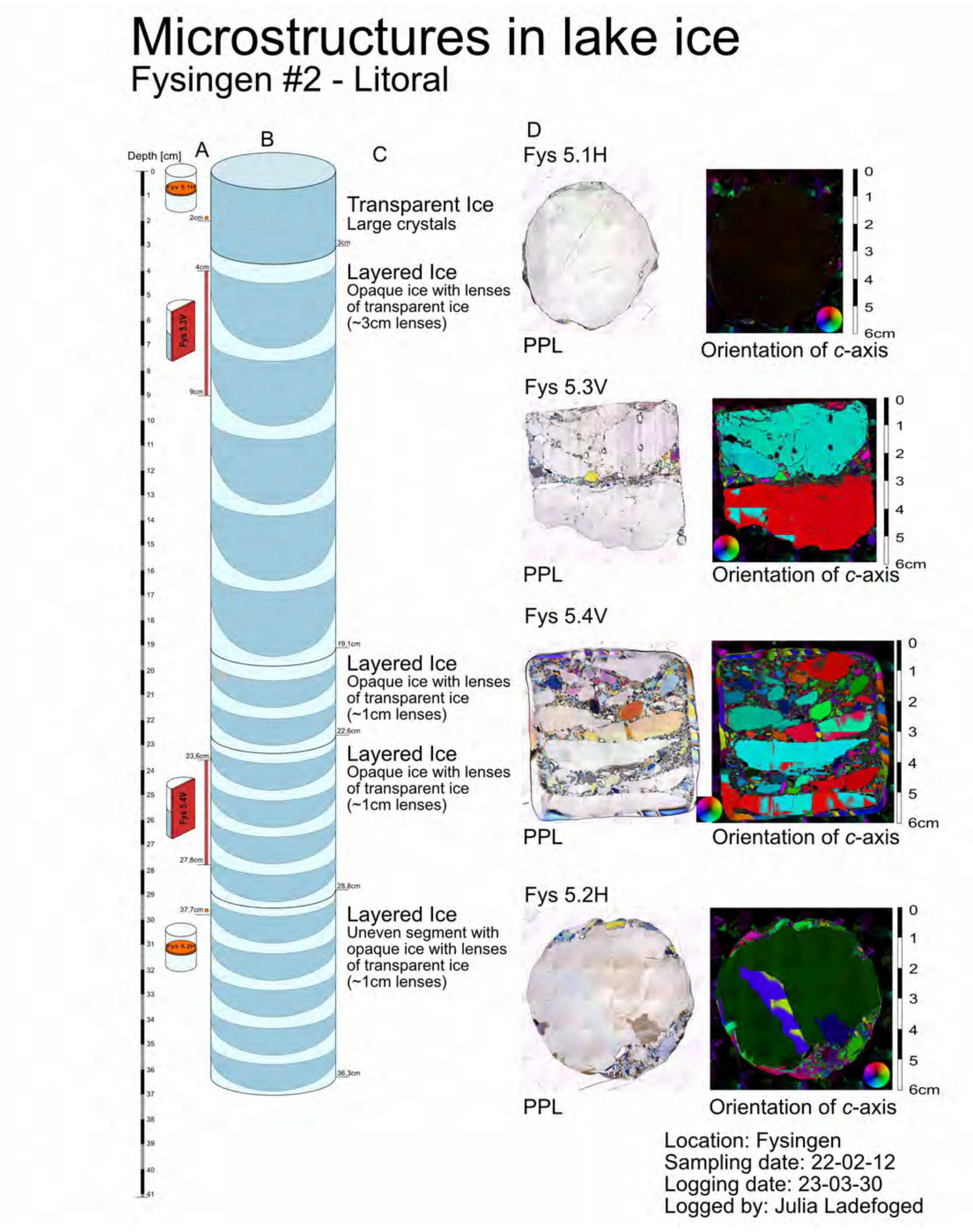

Figure 3.5: Illustrated representation of the Fysingen 2 ice core. A) The location samples were retrieved from. B) Illustrated representation of the ice core. c) Brief description of the ice core units. D) A plain polarized light(PPL) photo and a *c*-axis orientation photo from each sample.

3.1.1 *c*-axis Orientations

The *c*-axis orientations of the grains in the horizontal sections Trehörningen(Trh) 1.1H and Trh 2.1H, show a similar pattern of a dispersed maxima, see Figure 3.6 & 3.8. Consistently with the horizontal sections, the corresponding vertical sections, Trh 1.3V and Trh 2.3V, displays a similar trend of a dispersed *c*-axis orientation maxima in the small grains, see Figure 3.6 & 3.8. However, in both vertical thin sections Trh 1.3V and Trh 2.3V there are layers within the domain of smaller grains, with slightly finer grains. The *c*-axis distribution of these finer grained layers all indicate a clear maxima in the center, i.e. the z-axis, see Figure 3.6 & 3.8.

The *c*-axis orientations of grains in the horizontal sections Trh 1.5H and Trh 2.2H, both show a clear maxima in the center, see Figure 3.7 & 3.9. The corresponding vertical sections Trh 1.4V and Trh 2.4V show a similar trend of a clear maxima in the center, see Figure 3.7 & 3.9. However, these results can be misleading due to a low number, larger crystals, analysed.

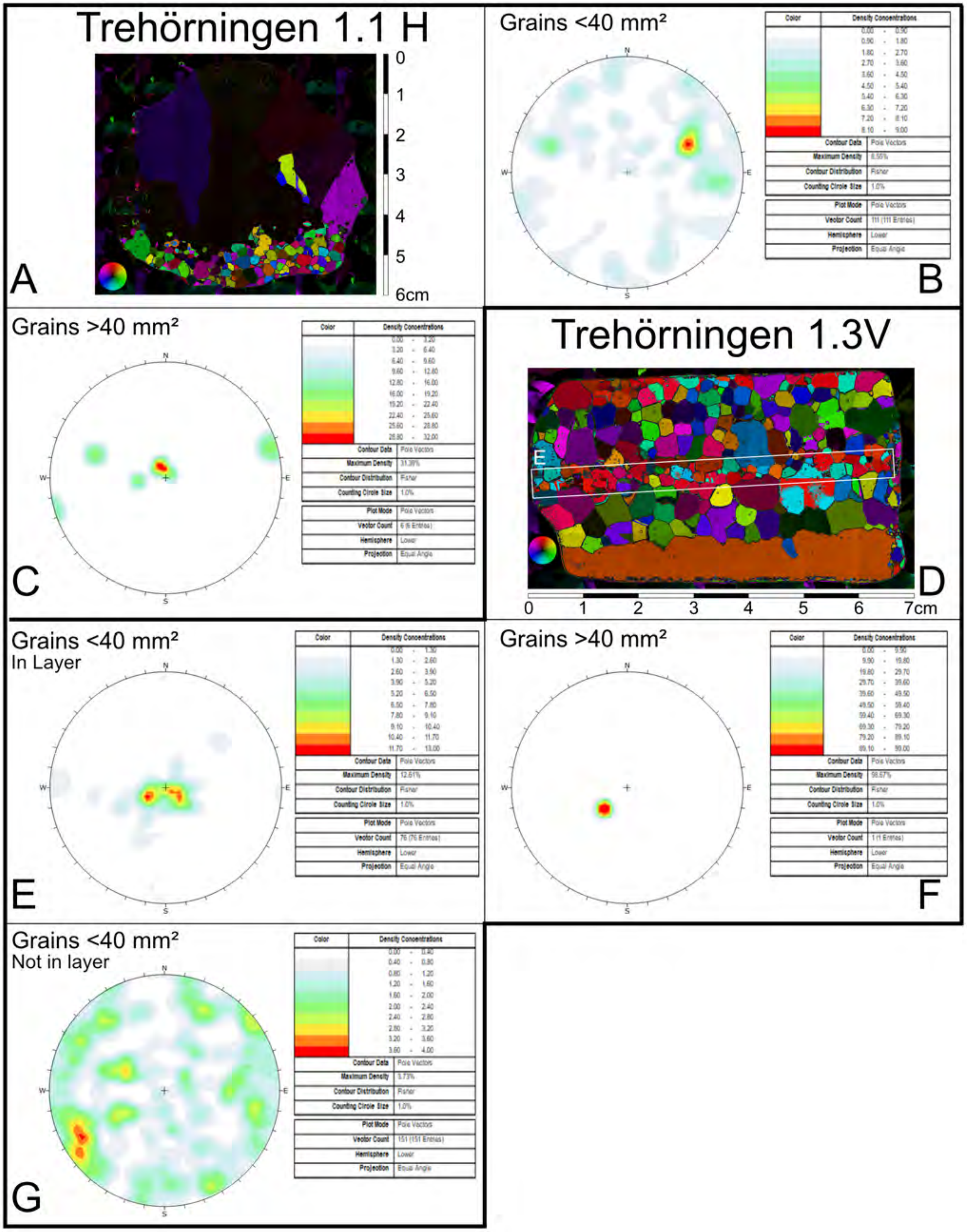

Figure 3.6: A) *c*-axis orientation image from thin section Trh 1.1H. B) Stereonet displaying *c*-axis orientation distribution of all small and medium grains <40mm^2 in thin section Trh 1.1H. C) Stereonet displaying *c*-axis orientation distribution of all grains >40mm^2 in thin section Trh 1.1H. D) *c*-axis orientation image from thin section Trh 1.3V. E) Stereonet displaying *c*-axis orientation distribution of all small and medium grains <40mm^2 in the marked layer in thin section Trh 1.3V. F) Stereonet displaying *c*-axis orientation distribution of grains >40mm^2 in marked layer, in thin section Trh 1.3V. G) Stereonet displaying *c*-axis orientation distribution of all grains <40mm^2 in thin section Trh 1.3V, except the grains in marked layer.

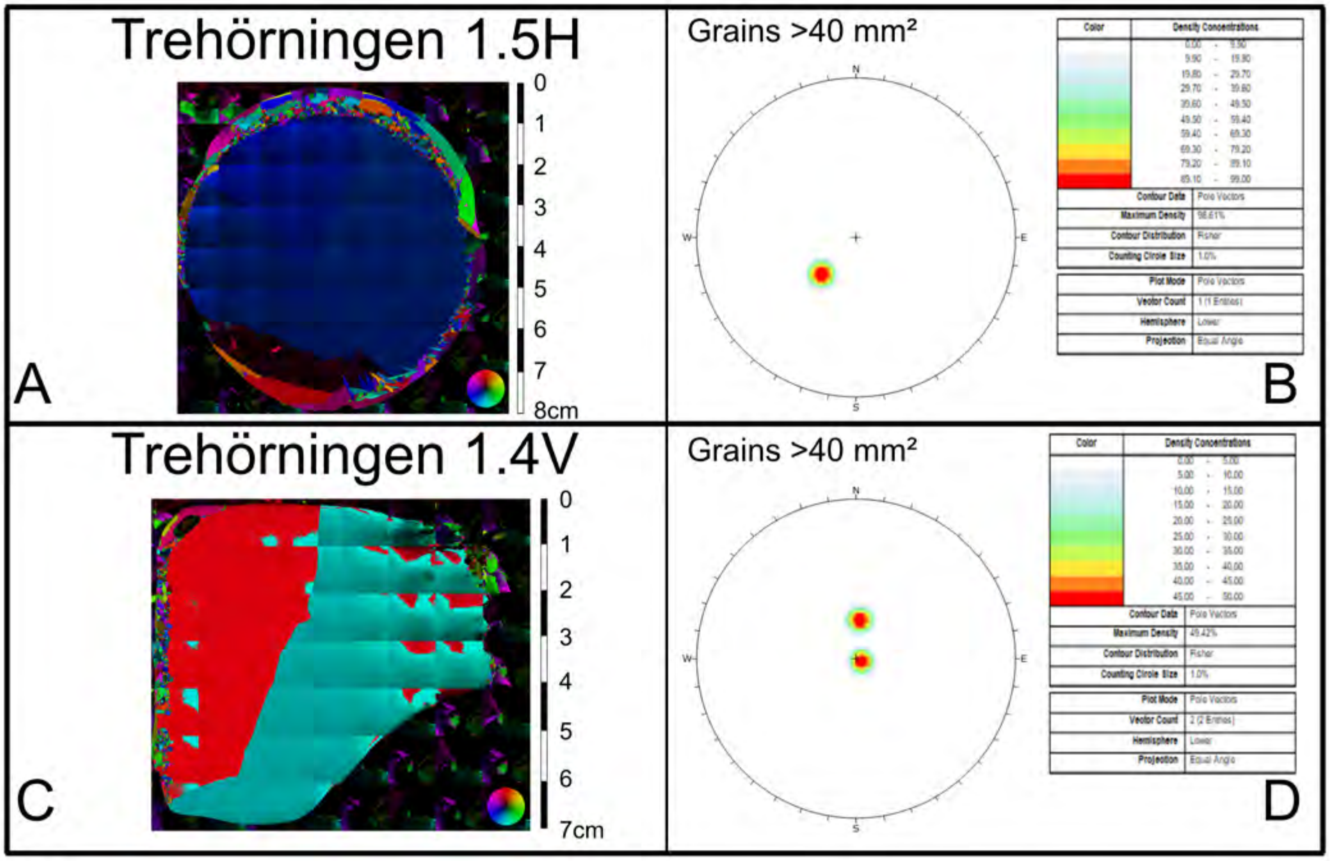

Figure 3.7: A) *c*-axis orientation image from thin section Trh 1.5H. B) Stereonet displaying *c*-axis orientation distribution of all grains in thin section Trh 1.5H. C) *c*-axis orientation image from thin section Trh 1.4V. D) Stereonet displaying *c*-axis orientation distribution of all grains in thin section Trh 1.4V.

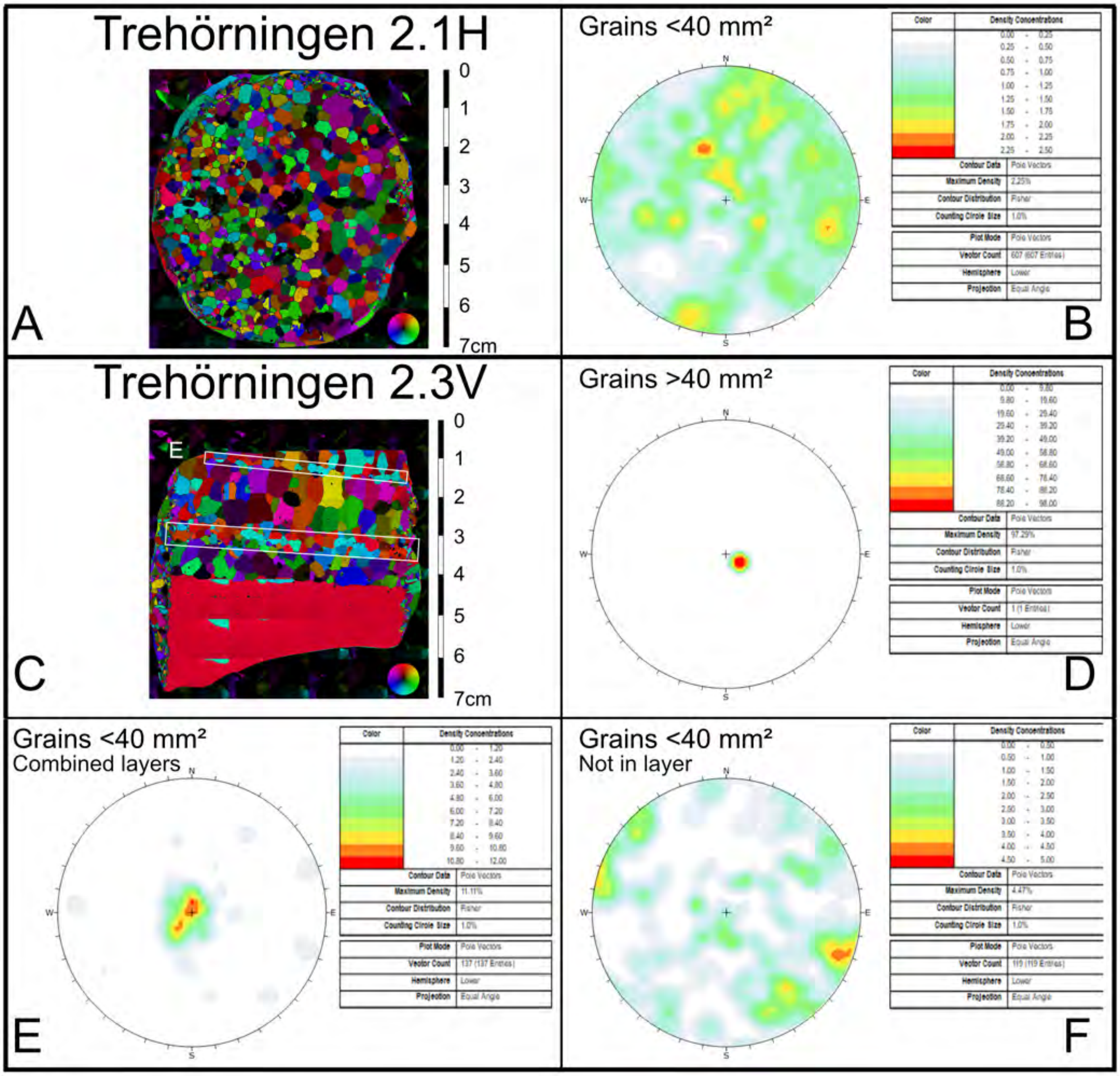

Figure 3.8: A) *c*-axis orientation image from thin section Trh 2.1H. B) Stereonet displaying *c*-axis orientation distribution of all grains in thin section Trh 2.1H. C) *c*-axis orientation image from thin section Trh 2.3V. D) Stereonet displaying *c*-axis orientation distribution of all grains >40mm^2 in thin section Trh 2.3V. E) Stereonet displaying *c*-axis orientation distribution of grains <40mm^2 in marked layer, in thin section Trh 1.3V. F)Stereonet displaying *c*-axis orientation distribution of grains <40mm^2 in thin section Trh 1.3V, except the grains in marked layer.

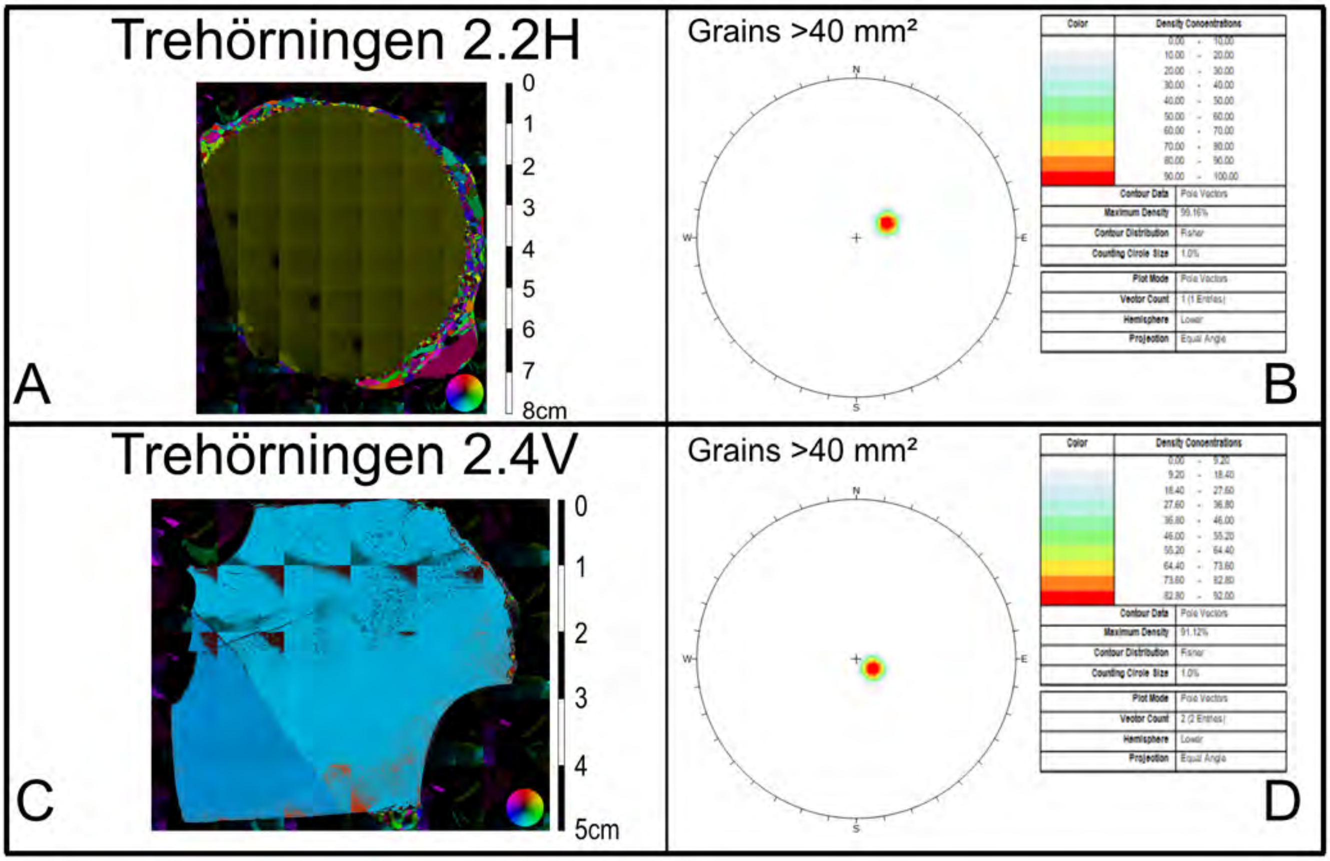

Figure 3.9: A) c-axis orientation image from thin section Trh 2.2H. B) Stereonet displaying c-axis orientation distribution of all grains in thin section Trh 2.2H. C) c-axis orientation image from thin section Trh 2.4V. D) Stereonet displaying c-axis orientation distribution of all grains in thin section Trh 2.4V.

In contrast to the samples from Trehörningen, the horizontal section from Valloxen(VO) 3.1H have a few larger grains embedded in a matrix of medium and smaller grains. The C axis orientation of the larger grains display a clear maxima in the center, while the medium grain sizes have a more disperse maxima, see Figure 3.10. The finer grains at the edge show a very dispersed maxima, however the finer grains near the center of the thin section show a weak, yet clear, maxima to the North-South. The corresponding vertical section VO3.3V mainly consists of a single large grain and a few layers of finer crystals. The c-axis orientation of the large grain show a clear maxima in the center, while the finer grains have a quite dispersed maxima with an absence of orientations in the North and South, see Figure 3.10.

The horizontal section VO3.2H consists of grains similar in size to the horizontal sections Trh1.1H & Trh2.1H, however the distribution of c-axis orientations differs. The c-axis orientations of the grains in VO3.2H indicate a weak, yet clear, maxima in the center, see Figure 3.11. The corresponding vertical section VO3.4V displays a layered structure, with larger lenses surrounded by medium and smaller grains. The c-axis orientation of the larger grains displays a clear maxima in the center, while the medium and smaller grain sizes show a more disperse maxima, see Figure 3.11.

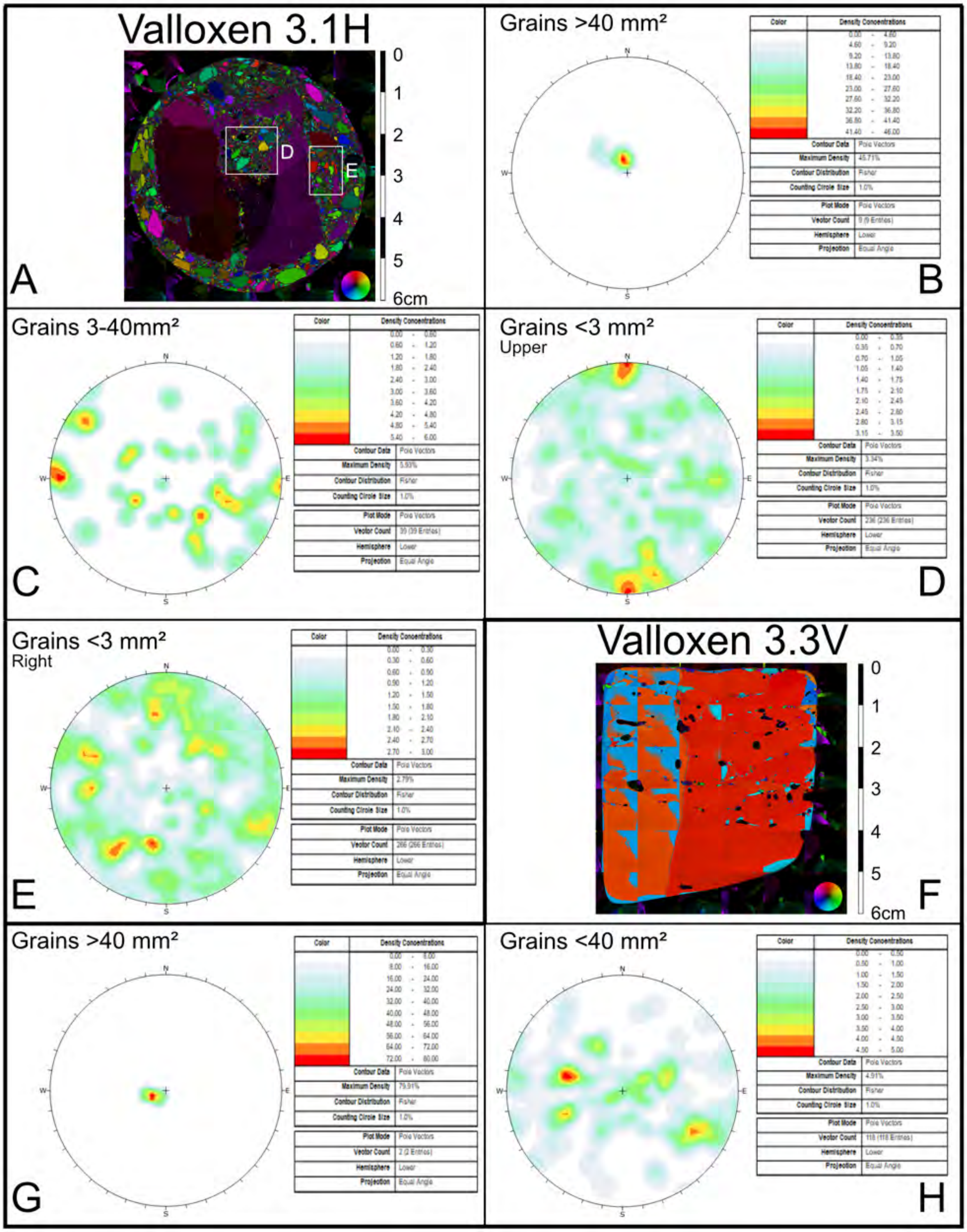

Figure 3.10: A) *c*-axis orientation image from thin section VO3.1H. B) Stereonet displaying *c*-axis orientation distribution of all grains $>40\text{mm}^2$ in thin section VO3.1H. C) Stereonet displaying *c*-axis orientation distribution of grains 3-40mm^2 in thin section VO3.1H. D) Stereonet displaying *c*-axis orientation distribution of all grains $< 3\text{mm}^2$ within the marked area in thin section VO3.1H. E) Stereonet displaying *c*-axis orientation distribution of all grains $< 3\text{mm}^2$ within the marked area in thin section VO3.1H. F) *c*-axis orientation image from thin section VO3.3V. G) Stereonet displaying *c*-axis orientation distribution of all grains $>40\text{mm}^2$ in thin section VO3.1H. H) Stereonet displaying *c*-axis orientation distribution of all grains $<40> 40\text{mm}^2$ in thin section VO3.1H.

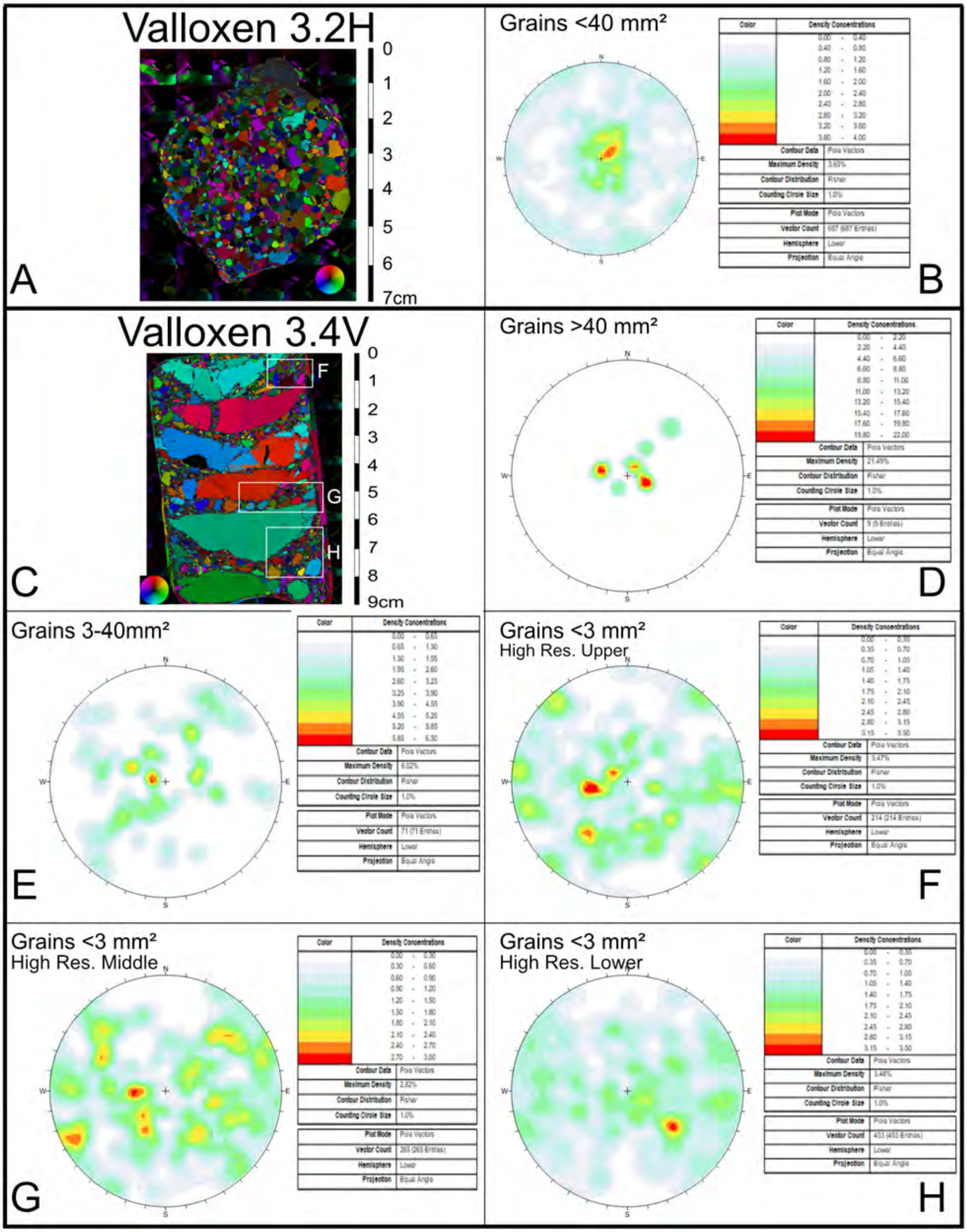

Figure 3.11: A) *c*-axis orientation image from thin section VO3.2H. B) Stereonet displaying *c*-axis orientation distribution of all grains in thin section VO3.2H. C) *c*-axis orientation image from thin section VO3.4V. D) Stereonet displaying *c*-axis orientation distribution of all grains >40mm^2 in thin section VO3.4V. E) Stereonet displaying *c*-axis orientation distribution of all grains 3-40mm^2 in thin section VO3.4V. F) Stereonet displaying *c*-axis orientation distribution of all grains <3mm^2 within the marked area in thin section VO3.4V. G) Stereonet displaying *c*-axis orientation distribution of all grains <3mm^2 within the marked area in thin section VO3.4V. H) Stereonet displaying *c*-axis orientation distribution of all grains <3mm^2 within the marked area in thin section VO3.4V.

The horizontal section Fysingen(Fys) 4.1H show a similar pattern to Trh1.5H and Trh2.2H, with a single large crystal with a *c*-axis orientation in the center, see Figure 3.12. The vertical section Fys4.3V consists of a large grain and a few layers of smaller grains. The large crystal have a *c*-axis orientation in the center and the *c*-axis orientation distribution of the small grains are quite dispersed, with a weak, yet clear maxima in the center, see Figure 3.12.

The thin sections Fys4.2H and Fys4.4V displays almost identical structures as VO3.1H and VO3.3V. Where the horizontal section Fys4.2H consists of a few larger grains in a matrix of smaller grains and the corresponding vertical section have layers of larger grains in between medium and smaller grains, see Figure 3.13. The *c*-axis orientation distribution of the larger and medium grains from both thin sections show a clear maxima in the center, while the smaller grains show a more dispersed maxima. The smaller grains from thin section Fys4.4V indicate a weak maxima in the center respective North.

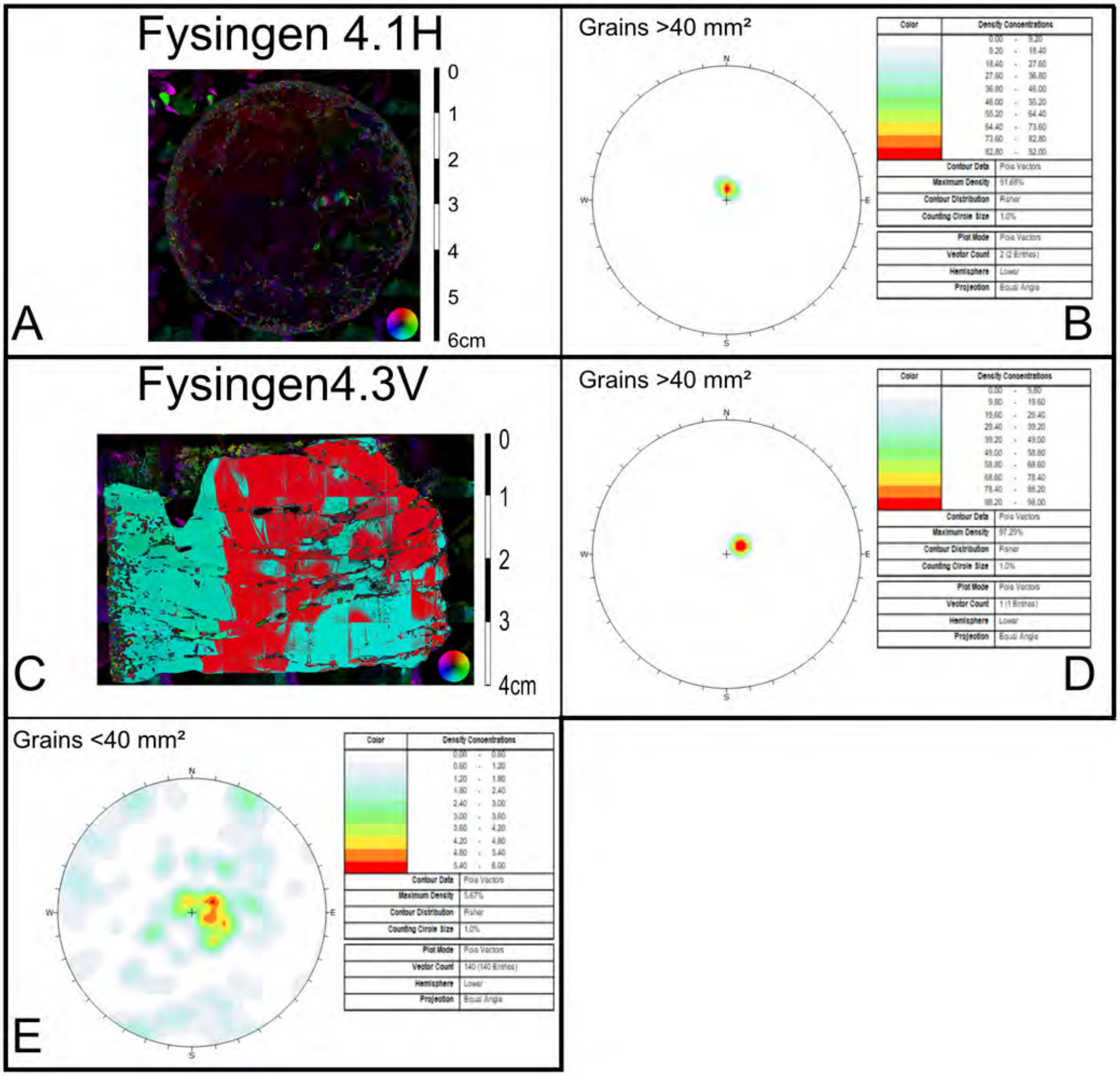

Figure 3.12: A) *c*-axis orientation image from thin section Fys4.1H. B) Stereonet displaying *c*-axis orientation distribution of all grains in thin section Fys4.1H. C) *c*-axis orientation image from thin section Fys4.3V. D) Stereonet displaying *c*-axis orientation distribution of all grains >40mm² in thin section Fys4.3V. E) Stereonet displaying *c*-axis orientation distribution of all grains <40mm² in thin section Fys4.3V.

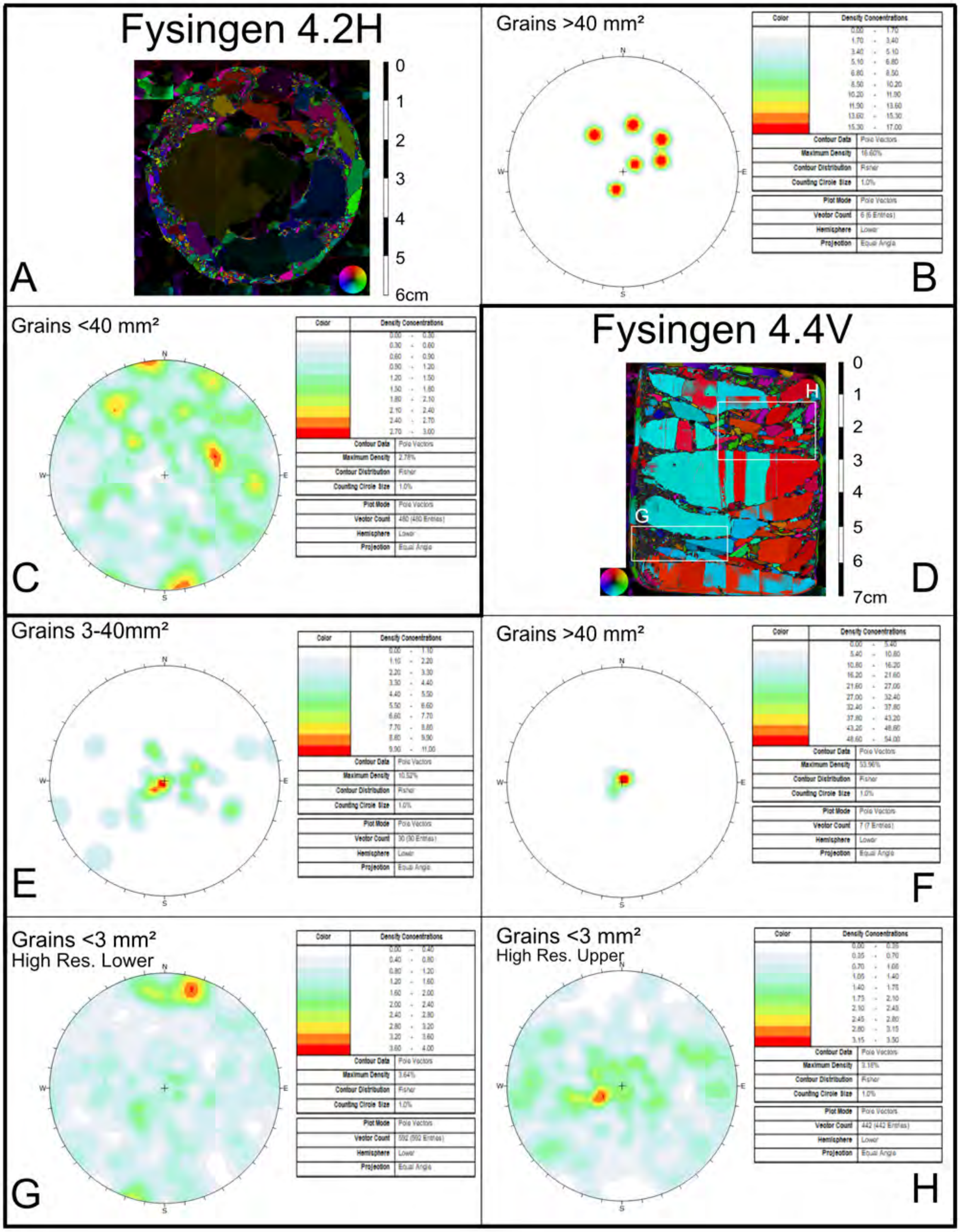

Figure 3.13: A) *c*-axis orientation image from thin section Fys4.2H. B) Stereonet displaying *c*-axis orientation distribution of all grains >40mm^2 in thin section Fys4.2H. C) Stereonet displaying *c*-axis orientation distribution of all grains <40mm^2 in thin section Fys4.2H. D) *c*-axis orientation image from thin section Fys4.4V. E) Stereonet displaying *c*-axis orientation distribution of all grains 3-40mm^2 in thin section Fys4.4V. F) Stereonet displaying *c*-axis orientation distribution of all grains >40mm^2 in thin section Fys4.4V. G) Stereonet displaying *c*-axis orientation distribution of all grains <3mm^2 within the marked area in thin section Fys4.4V. H) Stereonet displaying *c*-axis orientation distribution of all grains <3mm^2 within the marked area in thin section Fys4.4V.

The horizontal thin section Fys5.1H is made up by one large grain with a c-axis orientation in the center, see Figure 3.14, similarly to Trh 1.5H, Trh 2.2H and Fys4.1H. The corresponding vertical section also mainly consist of two large grains with a c-axis orientation in the center and a layer of finer grains with a more dispersed c-axis orientation distribution, with a very weak maxima in the center, see Figure 3.14.

Thin section Fys5.2H consists of a few large grains with a slightly dispersed c-axis orientation distribution, see Figure 3.15. The corresponding vertical section Fys5.4V show a similar structure as VO3.4V and Fys4.4V, with lenses of larger crystals surrounded by a matrix of medium and smaller grain sizes. The large grains show a strong and clear c-axis orientation distribution maxima in the center, the medium grains show a slightly more dispersed distribution with a weak maxima in the center, while the small grains have a very dispersed maxima, see Figure 3.15.

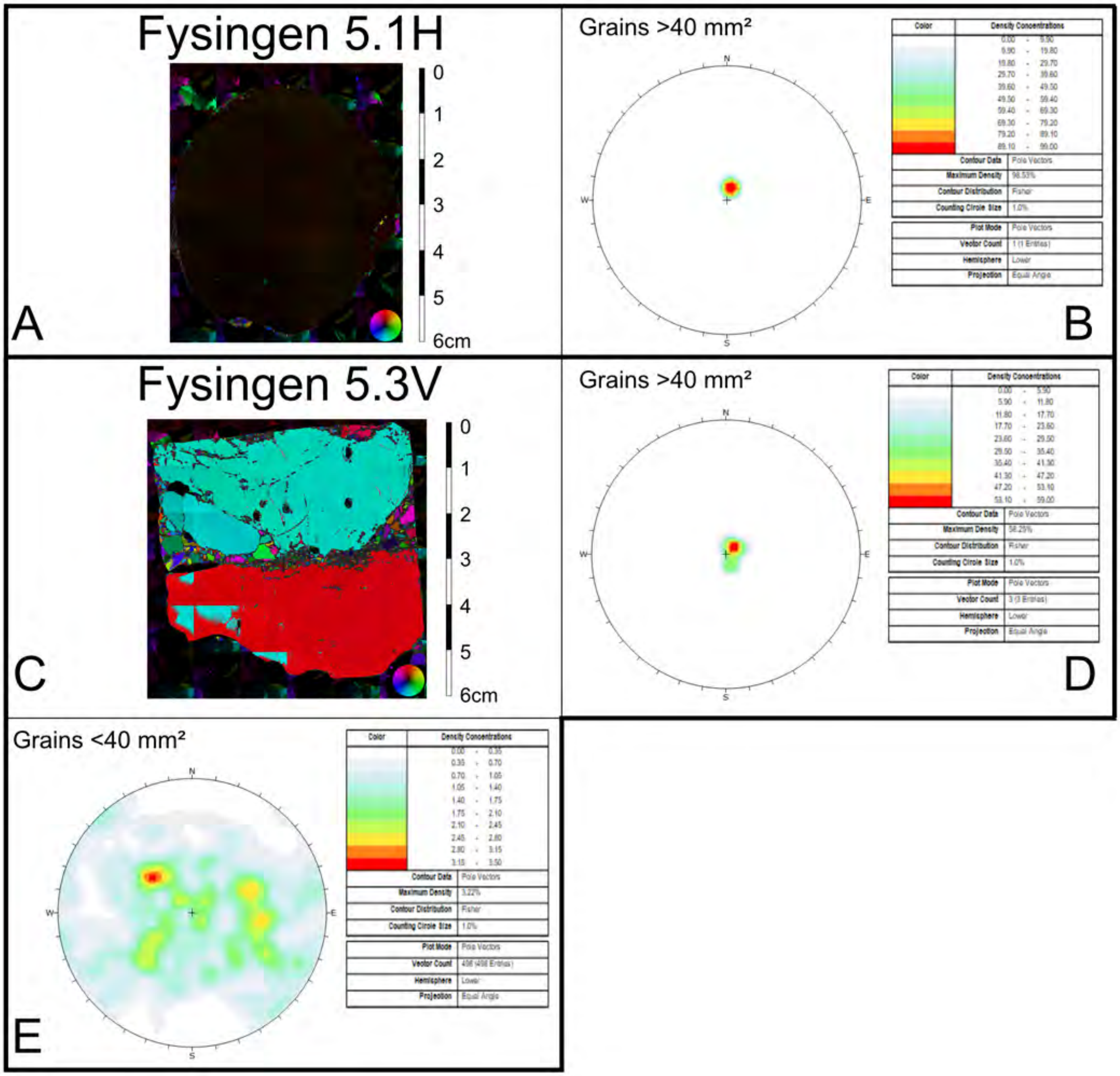

Figure 3.14: A) c-axis orientation image from thin section Fys5.1H. B) Stereonet displaying c-axis orientation distribution of all grains in thin section Fys5.1H. C) c-axis orientation image from thin section Fys5.3V. D) Stereonet displaying c-axis orientation distribution of all grains >40mm² in thin section Fys5.3V. E) Stereonet displaying c-axis orientation distribution of all grains <40mm² in thin section Fys5.3V.

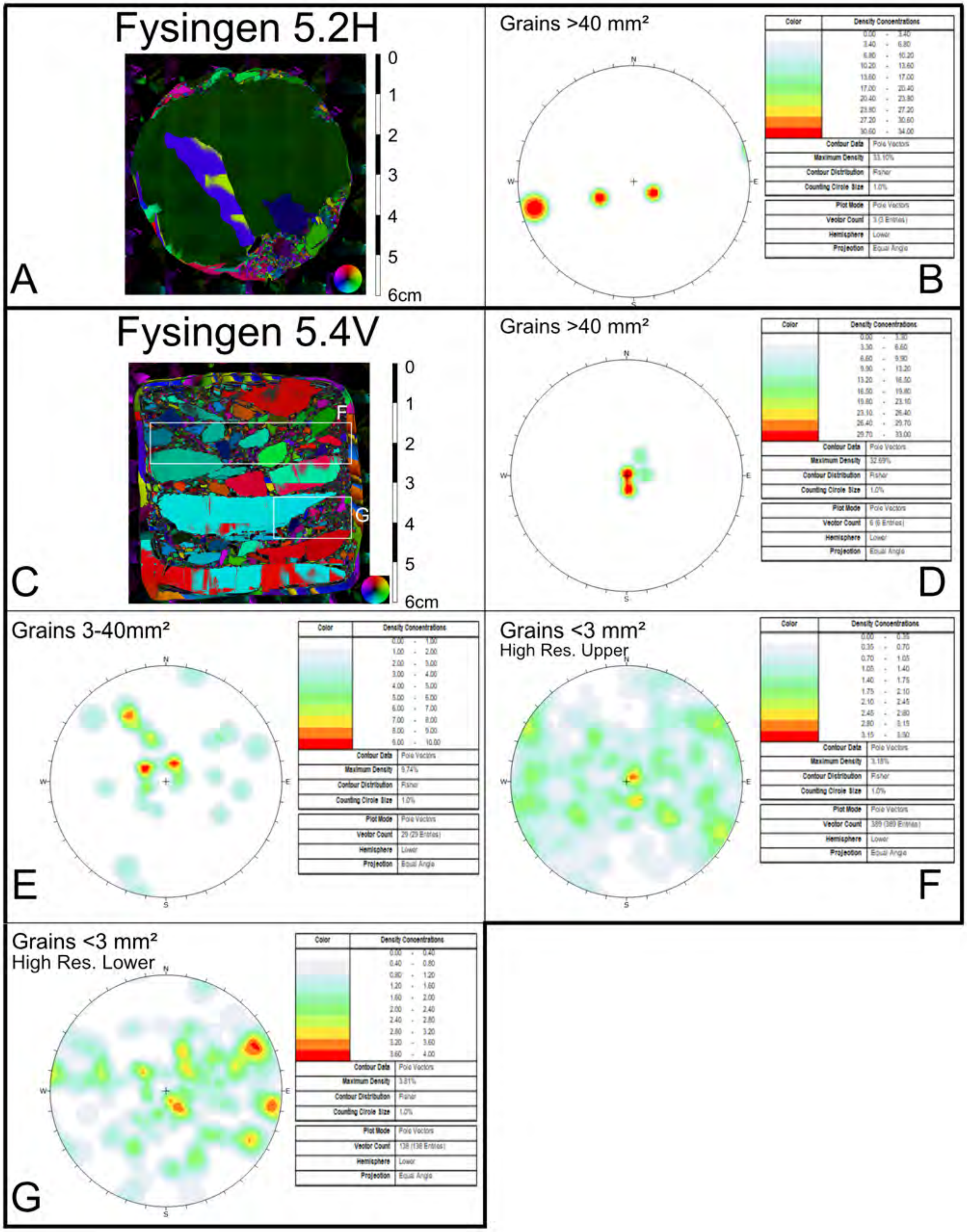

Figure 3.15: A) *c*-axis orientation image from thin section Fys5.2H. B) Stereonet displaying *c*-axis orientation distribution of all grains in thin section Fys5.2H. C) *c*-axis orientation image from thin section Fys5.4V. D) Stereonet displaying *c*-axis orientation distribution of all grains >40mm² in thin section Fys5.4V. E) Stereonet displaying *c*-axis orientation distribution of all grains 3-40mm² in thin section Fys5.4V. F) Stereonet displaying *c*-axis orientation distribution of all grains <3mm² within the marked area in thin section Fys5.4V. G) Stereonet displaying *c*-axis orientation distribution of all grains <3mm² within the marked area in thin section Fys5.4V.

3.1.2 Grain Geometry

The grain area distribution from all analysed thin sections display two contrasting trends; Well distributed grain sizes with a low frequency & small grain sizes with a clear frequency maxima.

The grain area distribution of grains from Trh1.1H, Trh1.3V, Trh2.1H and Trh2.3V display similar trends of well distributed grainsizes ranging from $<1\mathbf{mm^2}$ to approximately $10\mathbf{mm^2}$. However, the frequency of grains $<1\mathbf{mm^2}$ is larger in Trh1.3V compared to Trh1.1H, Trh2.1H and Trh2.3V, see Figure 3.16A-B.

The grain area distribution of grains from VO3.1H, VO3.3V, VO3.2H, VO3.4V, Fys4.2H, Fys4.4V, Fys 4.3V, Fys5.3V and Fys5.4V display a similar trend of high frequency of smaller grain areas. The grain areas are predominantly $<0.5\mathbf{mm^2}$, with a frequency of 0.7-0.9, and the frequency is decreasing with size, see Figure 3.16C-H.

All thin sections show similar grain size characteristics in both vertical and corresponding horizontal section.

Similarly to the grain area distribution, there are two distinct trends of the Area equivalent diameter(AED) distribution; Grains with a well distributed AED with a low frequency & Small AED with a clear frequency maxima.

The majority of the equal area diameter(EAD) of the grains from Trh1.1H, Trh1.3V, Trh2.1H, Trh2.3V ranges from <0.4-4mm with a consistent frequency of approximately 0.1-0.2, with the exception of Trh1.1H, where the frequency gradually decreases with increasing diameter, see Figure 3.17A-B.

The majority of the AED of the grains from VO3.1, VO3.3V, VO3.2H, VO3.4V, Fys4.2H, Fys4.4V, Fys4.3V, Fys5.3V and Fys5.4V ranges from <0.4-1.6mm, with the exception of VO3.2H which ranges from 0.8-2.8mm. There is a clear frequency maxima of an AED ranging from 0.4-0.8mm, see Figure 3.17C-H.

All thin sections, apart from Trh1.1H, Trh1.3V, VO3.2H and VO3.4V, show similar AED characteristics in both vertical and corresponding horizontal section.

The elongation distribution from all analysed thin sections show a similar trend in frequency and with a maxima ranging from 0.5-0.75.

The elongation of grains from section Trh1.1H, 2.1H and 2.3V almost displays an extended normal distribution curve, where the maxima ranges from 0.45-0.65, see Figure 3.18A-B.

Trh1.3V, VO3.1H, VO3.3V, VO3.2H, VO3.4V, Fys4.2H, Fys4.4V, Fys5.3V and Fys5.4V also display an extended normal distribution curve, however with a maxima slightly shifted towards 1 and a gradual increase in frequency with the elongation, see Figure 3.18A,C-H. Fys4.3V display an irregular pattern with a frequency maxima at 0.65.

All thin sections, apart from Trh1.1H and Trh1.3V show similar elongation characteristics in both vertical and corresponding horizontal section.

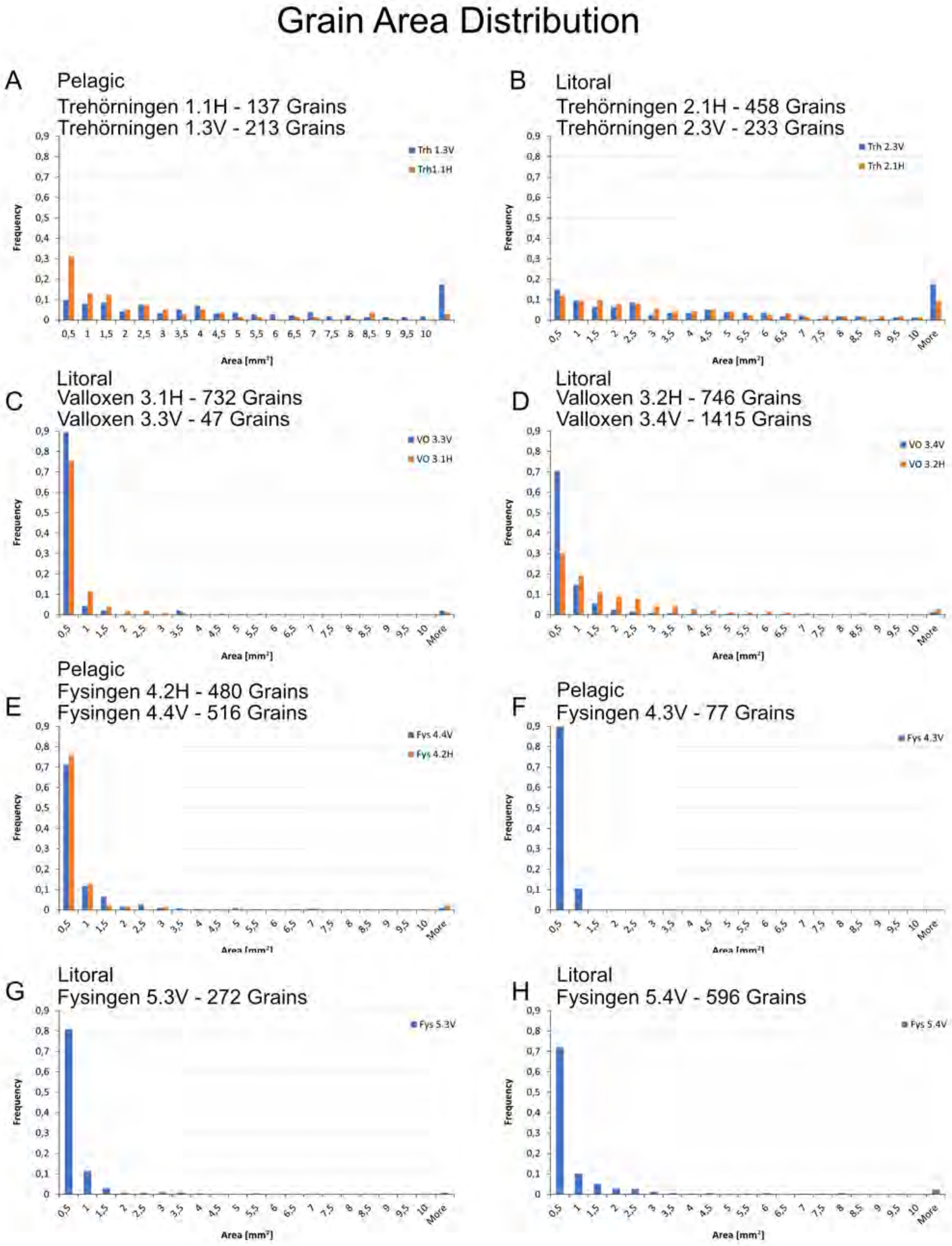

Figure 3.16: A) Grain area distribution and frequency of grains from section Trh1.1H & Trh1.3V. B) Grain area distribution and frequency of grains from section Trh2.1H & Trh2.3V. C) Grain area distribution and frequency of grains from section VO3.1H & VO3.3V. D) Grain area distribution and frequency of grains from section VO3.2H & VO3.4V. E) Grain area distribution and frequency of grains from section Fys4.2H & Fys4.4V. F) Grain area distribution and frequency of grains from section Fys4.3V. G) Grain area distribution and frequency of grains from section Fys 5.3V. H) Grain area distribution and frequency of grains from section Fys5.4V.

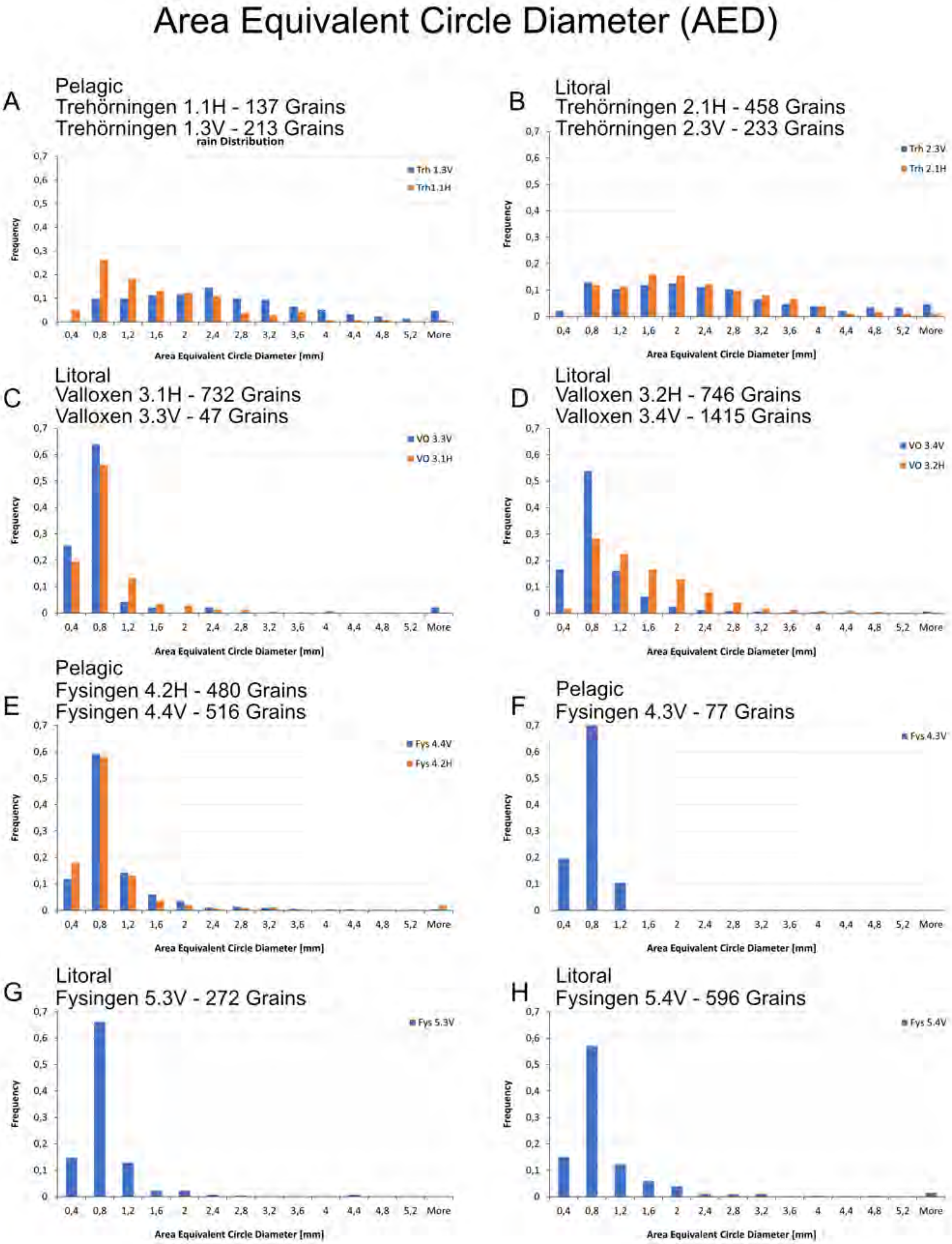

Figure 3.17: A) Area equivalent diameter(AED) distribution and frequency of grains from section Trh1.1H & Trh1.3V. B) Area equivalent diameter distribution and frequency of grains from section Trh2.1H & Trh2.3V. C) Area equivalent diameter distribution and frequency of grains from section VO3.1H & VO3.3V. D) Area equivalent diameter distribution and frequency of grains from section VO3.2H & VO3.4V. E) Area equivalent diameter distribution and frequency of grains from section Fys4.2H & Fys4.4V. F) Area equivalent diameter distribution and frequency of grains from section Fys4.3V. G) Area equivalent diameter distribution and frequency of grains from section Fys 5.3V. H) Area equivalent diameter distribution and frequency of grains from section Fys5.4V.

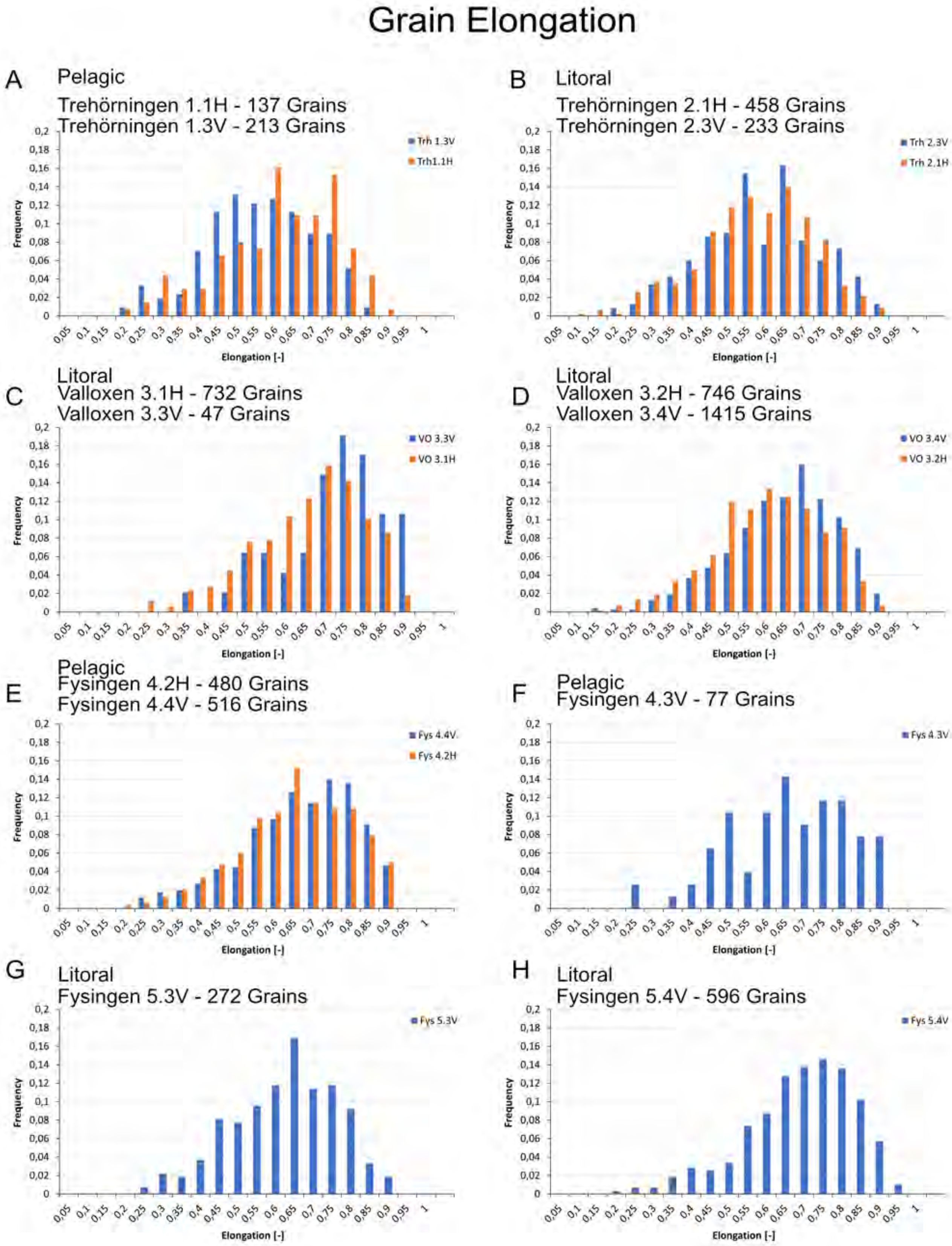

Figure 3.18: A) Elongation distribution and frequency of grains from section Trh1.1H & Trh1.3V. B) Elongation distribution and frequency of grains from section Trh2.1H & Trh2.3V. C) Elongation distribution and frequency of grains from section VO3.1H & VO3.3V. D) Elongation distribution and frequency of grains from section VO3.2H & VO3.4V. E) Elongation distribution and frequency of grains from section Fys4.2H & Fys4.4V. F) Elongation distribution and frequency of grains from section Fys4.3V. G) Elongation distribution and frequency of grains from section Fys 5.3V. H) Elongation distribution and frequency of grains from section Fys5.4V.

Similarly to the elongation, the distribution of Thinnes ratio of the grains in all thin sections display an extended and slightly shifted normal distribution curve.

The Thinnes ratio of grains from section Trh1.1H, VO3.1H, VO3.3V, Fys4.4V and Fys5.4V show a frequency maxima at 0.55-0.65, see Figure 3.19.

Trh1.3V, Trh2.1H, Trh2.3V, VO3.2H, VO3.4V, Fys4.2H and Fys5.3V also display a shifted and extended normal distribution curve, however with a slightly larger maxima ranging from 0.7-0.85. Similarly to the elongation, Fys4.3V display an irregular pattern with a maxima of 0.75, see Figure 3.19.

All thin sections show similar Thinnes ratio characteristics in both vertical and corresponding horizontal section. However in VO3.2H, VO3.4V, Fys4.2H and Fys4.4V, the horizontal sections have a larger maxima.

The aspect ratio distribution from all analysed thin sections show decreasing frequency with increasing aspect ratio to a varying extent.

The aspect ratio of grains from section Trh1.1H, Trh1.3V, Trh2.1H, Trh2.3V and VO3.2H display a strong decrease in frequency with increased aspect ratio, the majority of the grain ranges from 1.15-1.75, see Figure 3.20.

However, VO3.1H, VO3.3V, VO3.4V, Fys4.2H, Fys4.3V, Fys5.3V and Fys 5.4V display a weaker decrease in frequency with aspect ratio and the majority of the grains ranging from 1.15-2.2, see Figure 3.20.

All thin sections show similar aspect ratio characteristics in both vertical and corresponding horizontal section, with the exception of VO3.3V which display an irregular trend.

There is no clear trend in the holes/grain area distribution. All thin sections have a large proportion of grains without any holes, however all large grains which are partly visible have larger proportions of holes/grain area compared to the smaller grains, see Figure 3.21.

The grain orientation distribution show three grain orientation preferences. Trh2.1, VO3.1H, VO3.2H and Fys4.2H indicate an equal grain orientation trend distribution, see Figure 3.22 B, C, G & H. On the contrary, VO3.3V, VO3.4V, Fys4.4V and Fys5.4V display one clear preferred orientation, see Figure 3.22 F, I, J & K. Lastly, Trh1.3V, Trh2.3V, Fys4.3V, Fys5.3V show two distinct preferred grain orientations, see Figure 3.22 D, E, L & M.

Trh1.1H differs from all other sections and indicate an equal orientation trend distribution with absence of grains in one clear orientation, see Figure 3.22 A.

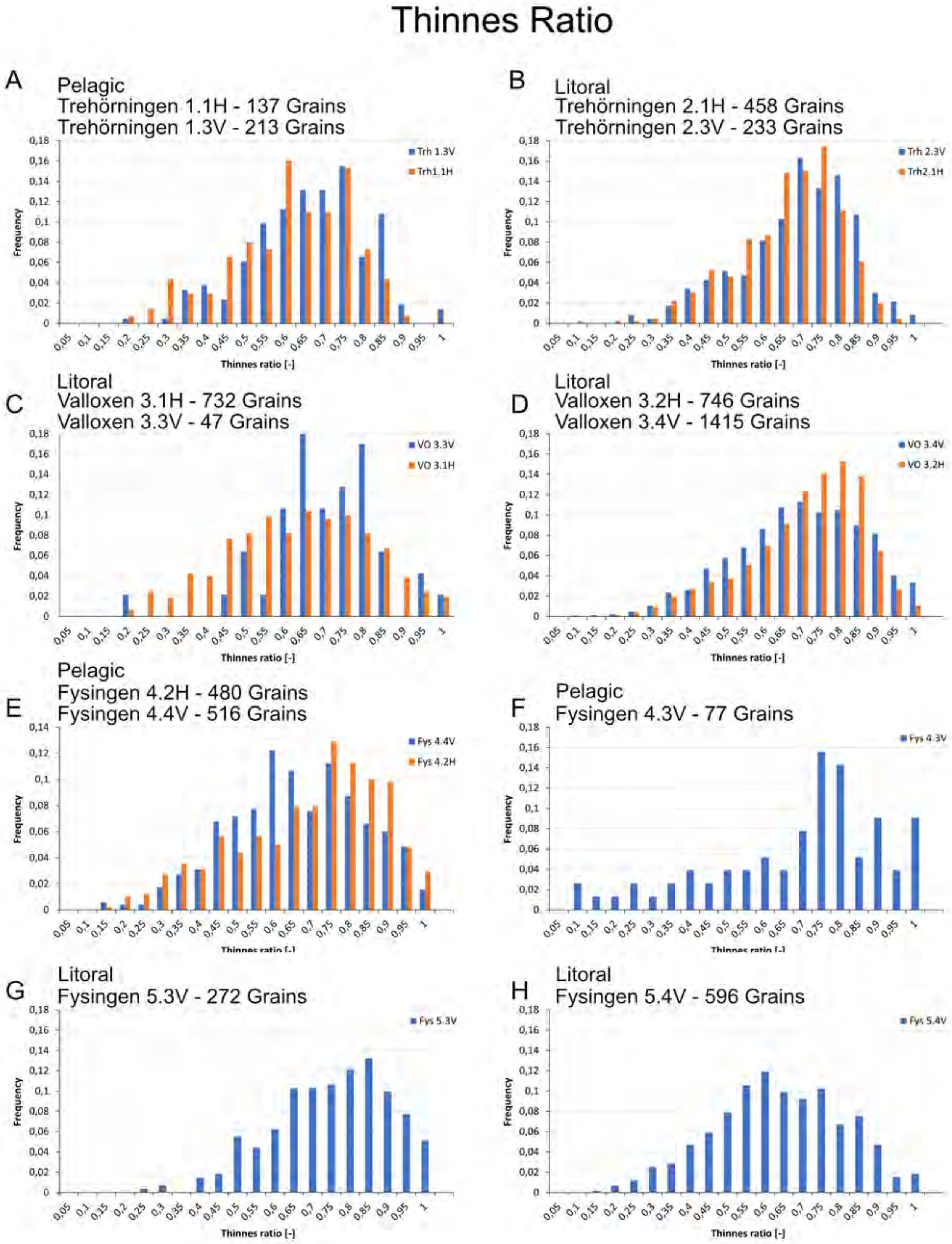

Figure 3.19: A) Thinnes ratio distribution and frequency of grains from section Trh1.1H & Trh1.3V. B) Thinnes ratio distribution and frequency of grains from section Trh2.1H & Trh2.3V. C) Thinnes ratio distribution and frequency of grains from section VO3.1H & VO3.3V. D) Thinnes ratio distribution and frequency of grains from section VO3.2H & VO3.4V. E) Thinnes ratio distribution and frequency of grains from section Fys4.2H & Fys4.4V. F) Thinnes ratio distribution and frequency of grains from section Fys4.3V. G) Thinnes ratio distribution and frequency of grains from section Fys 5.3V. H) Thinnes ratio distribution and frequency of grains from section Fys5.4V.

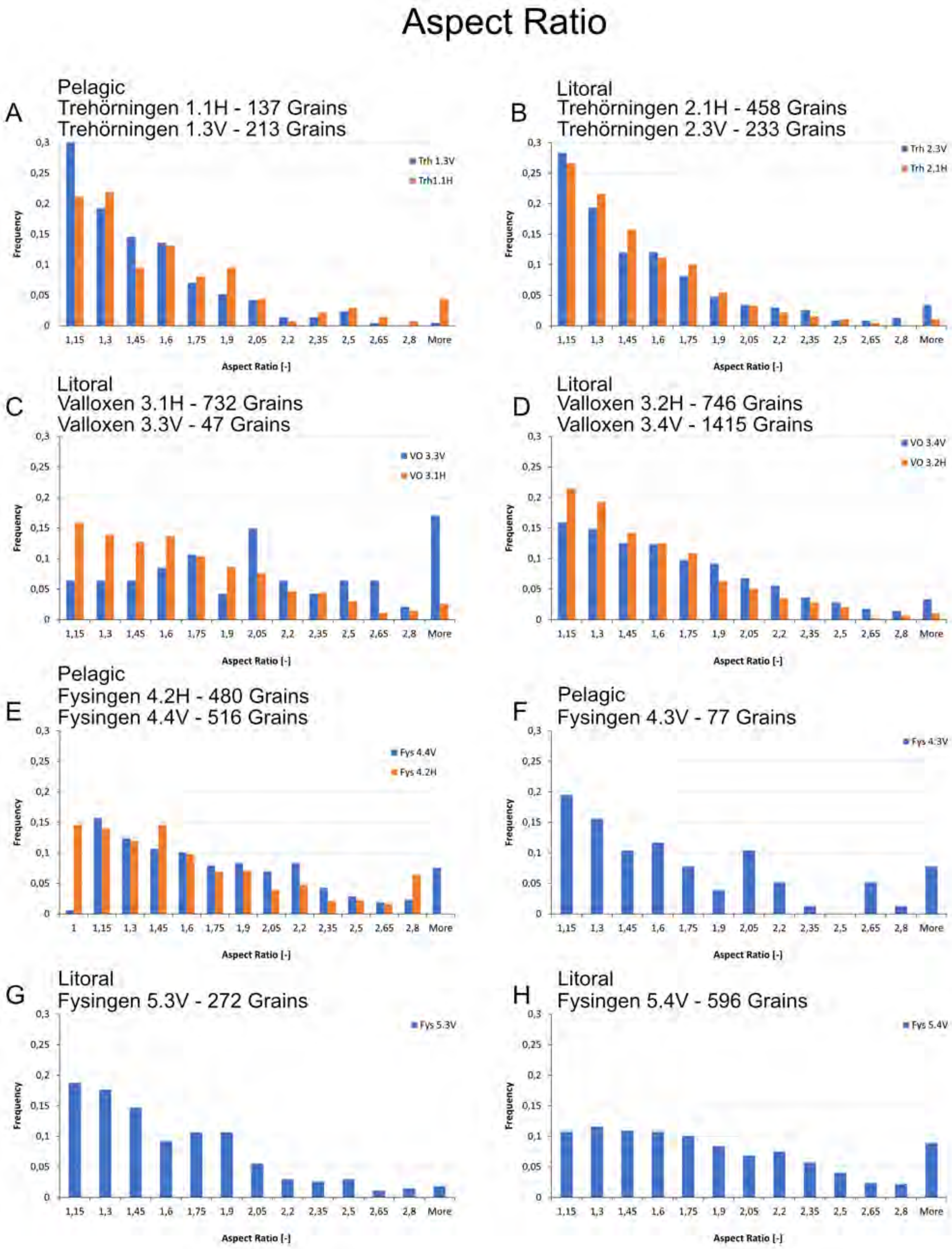

Figure 3.20: A) Aspect ratio distribution and frequency of grains from section Trh1.1H & Trh1.3V. B) Aspect ratio distribution and frequency of grains from section Trh2.1H & Trh2.3V. C) Aspect ratio distribution and frequency of grains from section VO3.1H & VO3.3V. D) Aspect ratio distribution and frequency of grains from section VO3.2H & VO3.4V. E) Aspect ratio distribution and frequency of grains from section Fys4.2H & Fys4.4V. F) Aspect ratio distribution and frequency of grains from section Fys4.3V. G) Aspect ratio distribution and frequency of grains from section Fys 5.3V. H) Aspect ratio distribution and frequency of grains from section Fys5.4V.

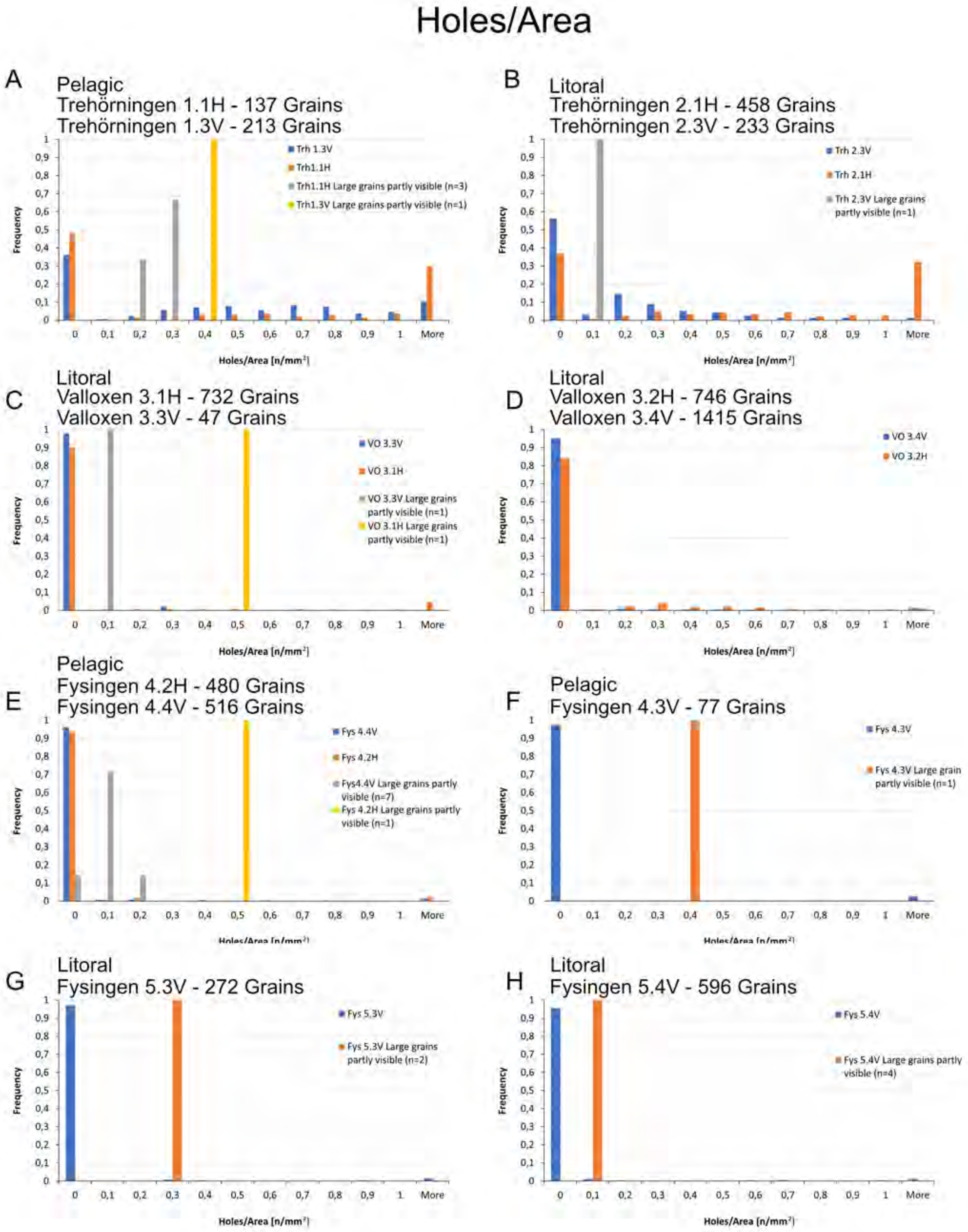

Figure 3.21: A) Holes/area distribution and frequency of grains from section Trh1.1H & Trh1.3V. B) Holes/area distribution and frequency of grains from section Trh2.1H & Trh2.3V. C) Holes/area distribution and frequency of grains from section VO3.1H & VO3.3V. D) Holes/area distribution and frequency of grains from section VO3.2H & VO3.4V. E) Holes/area distribution and frequency of grains from section Fys4.2H & Fys4.4V. F) Holes/area distribution and frequency of grains from section Fys4.3V. G) Holes/area distribution and frequency of grains from section Fys 5.3V. H) Holes/area distribution and frequency of grains from section Fys5.4V.

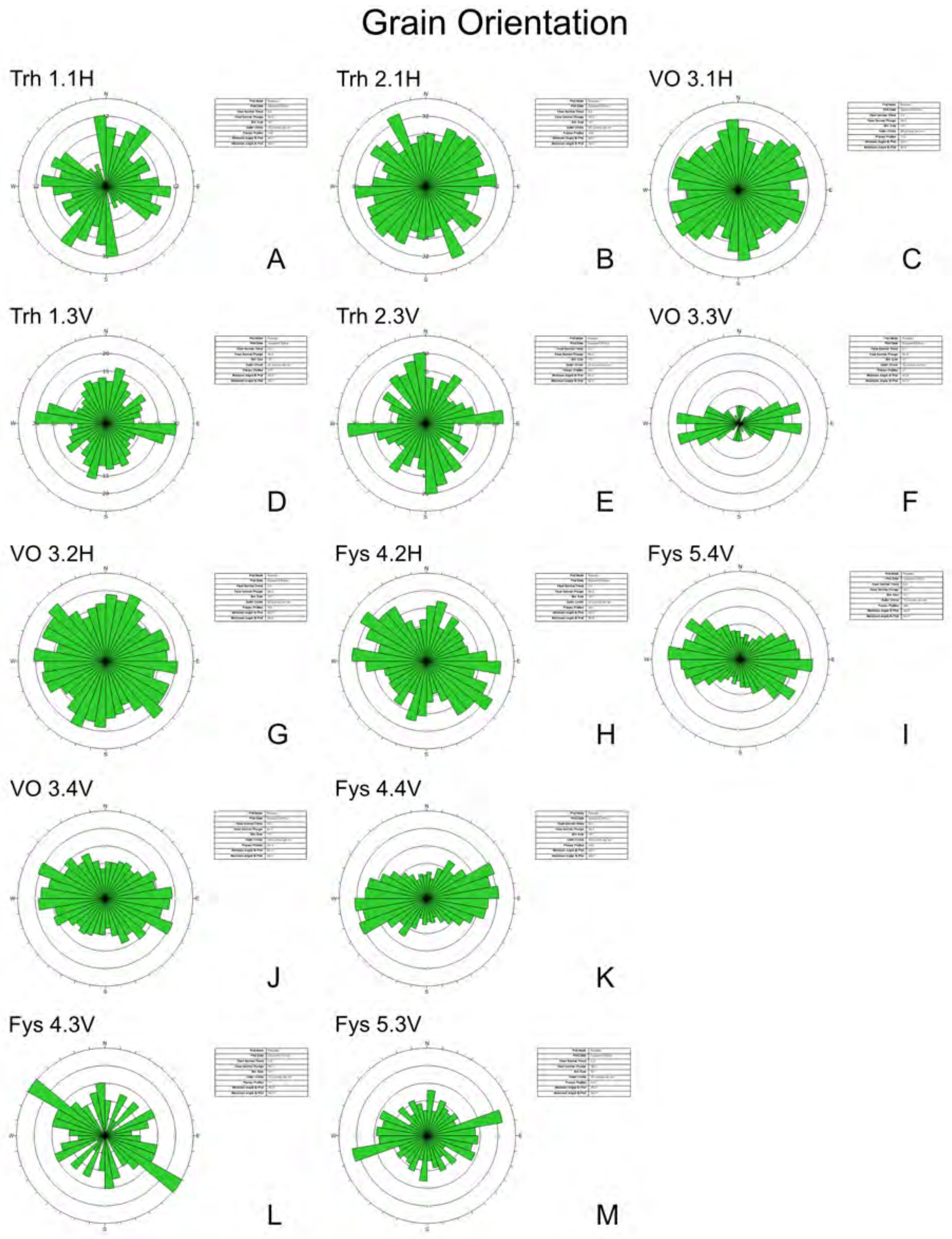

Figure 3.22: Rosediagram of grain orientation of respective thin section, with relative N-S and W-E orientations.

3.2 Mechanical Properties of the Ice Cores

The Uncalibrated compressive strength in all ice core segments ranges from 10.9MPa-34.7MPa with the exponential transducers and 13.55MPa-40.7MPa with the 54kHz transducers. The transparent ice ranges from 14.7MPa-34.7MPa and an average of 20.24MPa with the exponential transducers and with the 54kHz transducers 32.2MPa-37.5MPa with an average of 34.64MPa.

The transition zone was measured to 16.78MPa with the exponential transducers and 35.7MPa with the 54kHz transducers, however there was only one transition zone segment with successful measurements.

The compressive strength of the layered ice ranges from 10.9MPa-16.6MPa with an average of 13.68MPa with the exponential transducers. With the 54kHz transducers the strength rages from 17MPa-40.7MPa with an average of 29.85MPa.

However, segment 1 from Fysingen Pelagic consisted of ice with different layer intensity, the thinner layers consisted of more opaque ice and the thicker layers of more transparent ice. The segment was thus split and measured separately, the thinner layers had a lower compressive strength(13.55MPa) compared to the thicker layers(35.1MPa).

All successful measurements of the uncalibrated compressional strength of the segments are presented in Table 3.1.

Lake	Segment	Ice type	Compressional strength with 54kHz exponential transducers	Compressional strength with 54kHz transducers
Trehörningen Pelagic	2	Transparent ice	14.70MPa	-
Trehörningen Pelagic	3	Transparent ice	15.71MPa	-
Trehörningen Pelagic	4	Transparent ice	15.83MPa	-
Trehörningen Litoral	1	Transition zone	16.78MPa	35.7MPa
Trehörningen Litoral	2	Transparent ice	-	37.5MPa
Trehörningen Litoral	3	Transparent ice	-	35.2MPa
Trehörningen Litoral	5	Transparent ice	34.7MPa	32.2MPa
Trehörningen Litoral	7	Transparent ice	-	32.6MPa
Valloxen Litoral	3	Layered ice	-	34MPa
Valloxen Litoral	4	Layered ice	10.9MPa	40.7MPa
Fysingen Pelagic	1	Layered ice	12.6MPa	-
Fysingen Pelagic	1, thin layers	Layered ice	-	13.55MPa
Fysingen Pelagic	1, thick layers	Layered ice	-	35.1MPa
Fysingen Pelagic	2	Layered ice	-	22.2MPa
Fysingen Pelagic	3	Layered ice	14.6MPa	17MPa
Fysingen Litoral	2	Layered ice	-	24.4MPa
Fysingen Litoral	3	Layered ice	-	35.6MPa
Fysingen Litoral	4	Layered ice	16.6MPa	37.7MPa
Fysingen Litoral	5	Layered ice	-	27.2MPa

Table 3.1: Uncalibrated compressive strength measurements of the ice core segments, measured with ultra sound.

3.3 Mechanical Properties of Ice in Different Orientations

The compressive strength of the 5x5x5cm cubes from Erken ranges from 34.5MPa-58.7MPa and the strengths varies with orientation and locality, see Figure 3.23. Measurements from the litoral locality is generally larger than the pelagic locality.

The pelagic samples display larger compressive strength in the vertical samples (Mdn. 48.6MPa), followed by the 30°(Mdn. 46.9MPa) and horizontal(Mdn. 46.4MPa) samples. The remaining orientations display slightly lower compressive strengths, with the 60° samples with a median of 44.3MPa, the 120° samples with a median of 44.05MPa and the 150° samples with a median of 43.08MPa. Thus, the median strength of the pelagic samples is decreasing with the orientation angle, with the exception of the horizontal samples.

The litoral samples displays smaller variations of compressive strength compared to the pelagic samples. The 60° samples have the largest compressive strength(Mdn. 53.8MPa) followed by the 150° samples (Mdn. 52.5MPa & upper quartile 52.5MPa), the 120° samples (Mdn. 51.1MPa & upper quartile 52.3MPa) and the vertical samples(Mdn. 49.75MPa & upper quartile 53.98MPa). The remaining orientations display slightly lower compressive strengths, where the 120° samples have a median of 49.15MPa and the 30° samples a median of 48.65MPa

The ice from the pelagic locality consists of transparent ice with 3 distinct layers of vertically extending bubbles and 3 additional layers with smaller uniform bubbles, see Figure 3.24. While the litoral locality also consists of transparent ice with layers of bubbles, there are only 2 vertically extending bubble layers and 4 smaller uniform bubble layers.

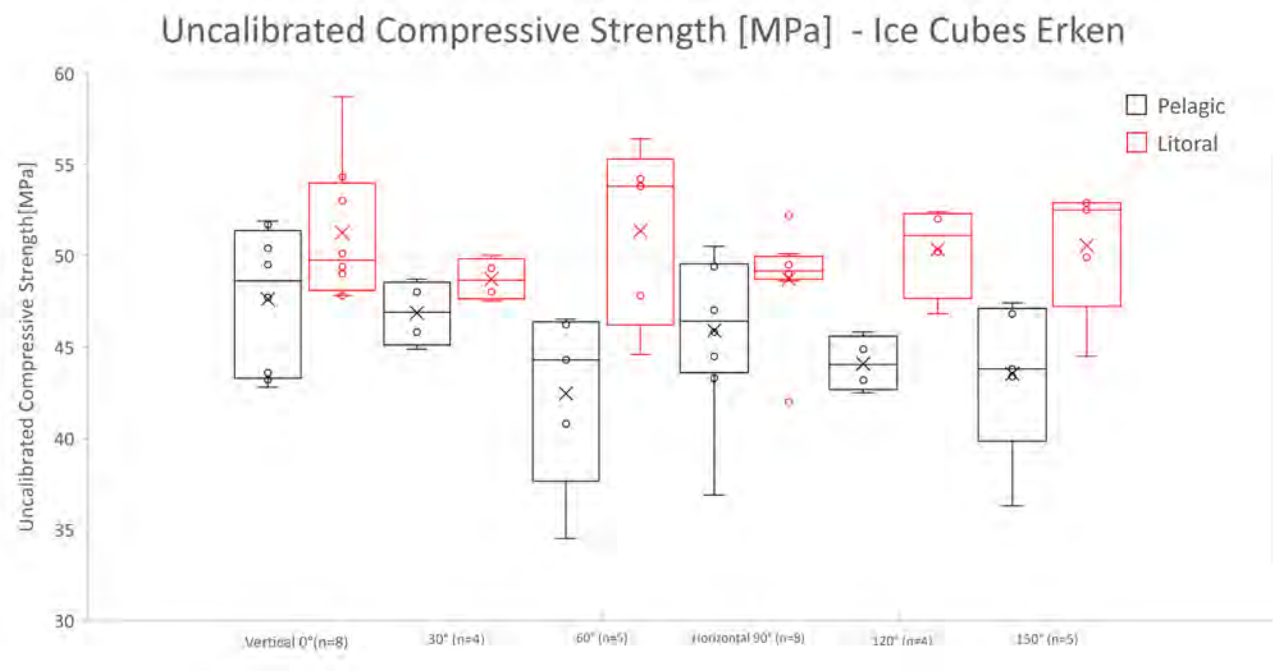

Figure 3.23: Box plot of uncalibrated compressive strengths of ice cubes from Erken in different orientations. Red box plots represent litoral samples and black represent pelagic samples.

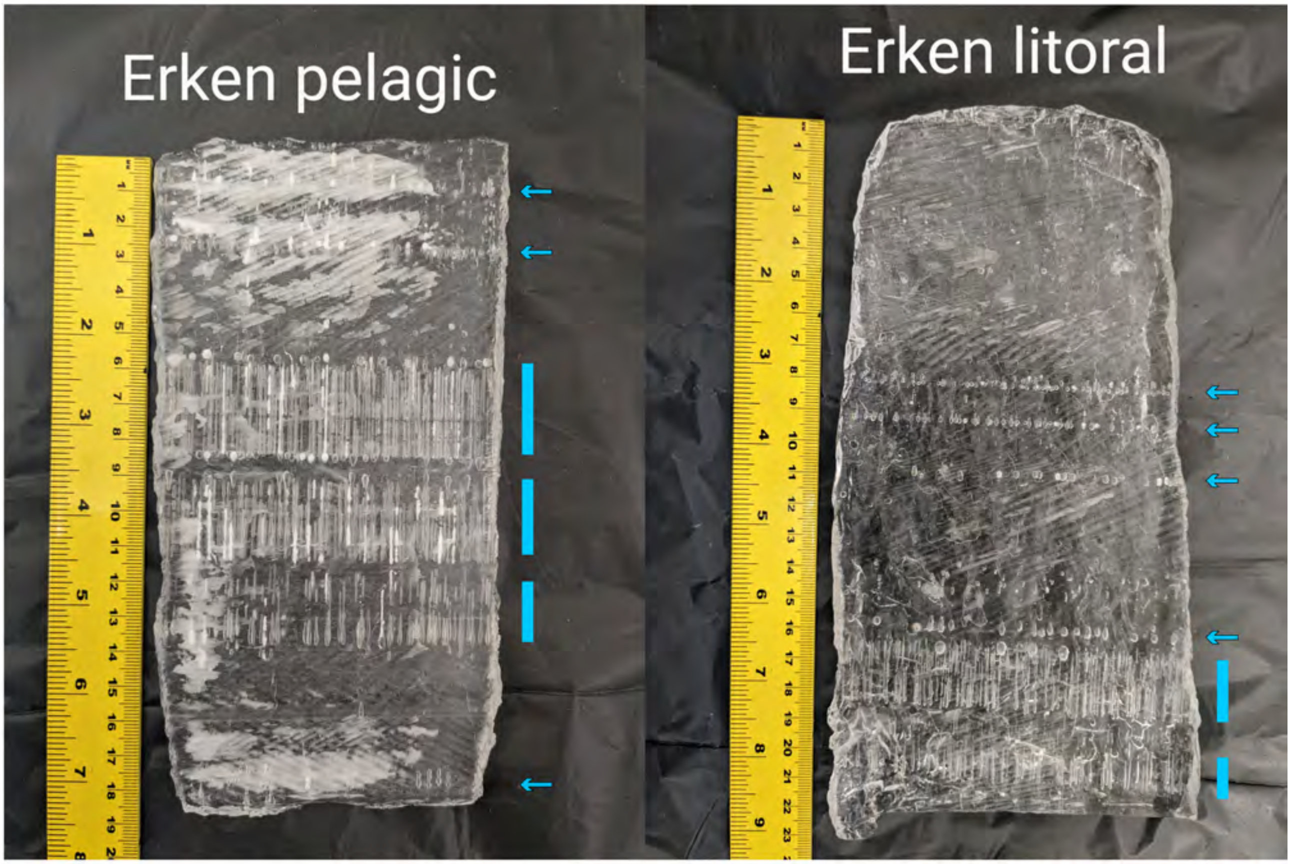

Figure 3.24: Photographs of the vertical section of the ice used for the investigations of compressive strength in different orientations. The blue lines and arrows mark the significant bubble layers.

Chapter 4

Discussion

4.1 Microstructures

The observed structures throughout the 5 ice cores exhibit two distinct overall core characteristics. Both cores from Trehörhingen predominantly consists of large, transparent crystals with a thin layer of small grained opaque ice on top. Meanwhile, the cores from Valloxen and Fysingen mainly consists of layered ice, with larger semispere crystals embedded in layers of smaller grains.

According to SMHI (SMHI & HavsVatten myndigheten, n.d.) the average daily temperature and precipitation, as well as number of days below 0°C during Autumn 2021 - Spring 2022, appear almost identical, see Figure 2.2. The low meteorological variation is most likely due to the proximity of the lakes, this would imply that the structural variation is independent of the average daily temperature and precipitation. Neither is the structural differences due to the sample localities, as the pelagic and the litoral samples from the same lake show similar characteristics.

However, lake Trehörningen is considerably smaller, both in volume and area, than both Fysingen and Valloxen, see Table 2.1. This parameter could thus be a contributing factor to the structural variations, or alternatively influencing another factor contributing to the variation, such as turbulence, wind velocity etc. The different lake volume might also contribute to a shorter time for the water temperature to reach 0°C, consequently influencing the timing of the first lake freezing. Which could mean, the lakes froze at different times with contrasting meteorological conditions.

Another lake property of importance could be the geometry, which separates the quite narrow lake Trehörningen from the more extensive lakes Valloxen and Fysingen.

4.1.1 *c*-axis Orientations

In the thin sections from lake Trehörningen there are mainly two crystal orientation characteristics, transparent ice with vertical *c*-axis orientations and opaque ice with a diffuse and randomly distributed *c*-axis orientation maxima, see Figure 3.6& 3.7 & 3.8 & 3.9. However, in the opaque ice there are also layers of finer grains with a clear vertical *c*-axis orientation, see Figure 3.6E & 3.8E.

According to Michel's(1971) classification both cores from Trehörningen could be described as a superimposed snow ice (T1) on top of a secondary columnar ice with preferred vertical *c*-axis orientation (S1). This would indicate a quiet lake where the initial ice sheet formed without seeding, followed by a later precipitation once the primary ice was already formed.

However, the layers with a preferred vertical *c*-axis orientation within the opaque ice is not in accordance with the T1 ice description. This either suggests this is not snow ice or there are variations of snow ice(T1) which are not described and included in the current classification.

The remaining 3 cores are considerably more complicated as there are larger semisphere grains stacked as layers within a smaller grained matrix, which can not be entirely explained with the complex classification of Michel(1971). All larger grains from Fysingen and Valloxen show a similar strong tendency of vertical *c*-axes, similar to the larger grains from Trehörningen.

Several of the layers with smaller crystals in Fysingen and Valloxen indicate a random *c*-axis distribution, similarly to the snow ice from Trehörningen. However there are also layers with a preferred *c*-axis orientation superimposed on a random orientation. This could possibly be indicative of recrystallization where the recrystallized grains have overprinted an originally random *c*-axis orientation distribution.

However, this information combined with the classification descriptions is not enough to draw any definite conclusions of the formation of the observed layered ice. Furthermore, it is difficult to distinguish weather this is secondary ice or superimposed ice, as no description entirely resemble the discovered structures. The following section will thus discuss plausible formation theories and what speaks for and against them.

Different Formation Models of the Layered Ice

A) Superimposed ice

- One possible explanation could be irregular melting at the surface, resulting in small melting ponds with similar shapes. The melting ponds slowly recrystallize when the temperature decrease, producing larger semispherical crystals with a preferred vertical *c*-axis orientation. This would explain the shape of the observed semispehere crystals, with an almost horizontal top boundary and a rounded base. The melting ponds are alternated with layers of superimposed snow ice, producing the smaller grained layers with a mostly random *c*-axis orientation.

  The layering could thus be a result of several daily or weekly melting and recrystallization cycles. Throughout the winter season 2022 there are observed temperature fluctuations above and bellow 0°, see Figure 2.2, which would support a melting model further.

  However, the layers of smaller crystals with preferred *c*-axis orientation superimposed on a random orientation can not be explained by this model, as of now. There is a possibility that snow ice is also exposed to some, lesser, extent of melting and recrystallization which could overprint the originally random *c*-axis orientation distribution, yet not enough to produce a melting pond. Another explanation would be that the observed smaller grained layers is related to the contact area of the melting ponds and the primary ice.

  Further research of how melting and recrystallization of lake ice change the microstructures, as well as the behaviour of the contact area of primary ice and recrystallized ice, is needed.

- Another potential model would be flooding of fracture systems. The produced secondary ice develop pronounced fractures, which are flooded by snow ice. Consequently there would be remains of larger grains of secondary ice with a prefered vertical *c*-axis orientation, as well as the surrounding smaller grained snow ice with an almost random *c*-axis orientation distribution.

  However, it is highly unlikely there are pervading horizontal fractures throughout a 20cm core as regularly as the observed layers of finer crystals.

  To determine if layered ice can be generated in fractures similarly to Fysingen and Valloxen, further research on how ice recrystallize in fractures is required.

- In Michel's(1971) classification there is a category of superimposed columnar ice(T3), which could possibly explain the larger grains observed in the layered cores. However, there is no description of their formation conditions or their characteristics.

  Further research of the formation of superimposed columnar ice and their characteristics, as well as what differentiates them from ordinary columnar ice, is needed.

- If flooding of lake ice can produce large crystals, there is a possibility of several flooding events of an uneven surface, alternated with accumulation of snow ice could produce the observed layered ice.

  However, there is a lack of documentation and illustrations of the characteristics of ice formed by flooding. It is thus difficult to recognize if this could even be remotely associated with flooding ice.

B) Secondary ice

- Michel (1971) describes a congealed frazil slush (S4), where layers of frazil ice can flow underneath the secondary ice and attach to the columnar ice. Occasional turbulent water could thus feed the columnar ice with layers of frazil ice.

  However, the only provided photograph of S4 ice does not look remotely similar to the observed layering. Furthermore, the images of frazil ice from other lakes mostly appear differently compared to the observed crystals within the small grained layers.

C) Agglomerate ice

- Agglomerate ice is described by Michel(1971) as a variation of different ice types, which could be the case for the different layers of larger crystals and a smaller grained matrix.

  However, usually the different ice variations are very irregular and not as consistently layered as observed in these cores.

None of the presented models can comprehensively explain the variety of structures observed in the few samples investigated in this thesis. This demonstrates the importance of further research of microstructures in lake ice, to improve characterization models as well as the formation processes.

4.1.2 Grain Geometry

The geometries of grains from Valloxen and Fysingen show similar characteristics, with an exception from the grain orientation. However, similarly to the structures there are geometrical differences between grains from Trehörningen compared to Valloxen and Fysingen, see Figure 3.16, 3.17 & 3.18.

This suggests different ice varieties, even though the *c*-axis distribution of the smaller grains indicate random orientations for samples from all cores. Furthermore, this supports the models where the smaller grains within the layered ice is derived from a separate process, for example recrystallization, and not from the same formation process as the interpreted T1 ice.

4.2 Uncalibrated Compressive Strength of Lake Ice

4.2.1 Compressive Strength of Different Ice Varieties

The uncalibrated compressive strength was successfully measured in 3 ice varieties, transparent ice(S1), the transition zone between transparent ice(S1) and opaque ice(T1), and layered ice. The transition zone, which consisted of both opaque ice and transparent ice, indicated lower uncalibrated compressive strength than the transparent ice, see Table 3.1. This indicate a larger compressive strength in transparent ice than opaque ice, which would be consistent with previous research demonstrating how transparent ice is stronger than opaque ice (Butkovich, 1954b, 1954a). However, there are too few measurements from transition zone segments in this thesis to make any definite conclusions.

The layered ice display a wide range of uncalibrated strengths, both larger and smaller than the transparent ice. This implies the strength of layered ice is dependent on the characteristics within each layer.

4.2.2 Compressive Strength of Ice from Different Localities

The ice cores show a distinct trend of larger uncalibrated compressive strength in the litoral samples compared to the pelagic samples, independent of ice types3.1.

The investigated cubes show a similar trend of larger uncalibrated compressive strengths in all litoral samples compared to the pelagic samples, 3.23. A possible contributing factor to the lower compressive strength of the pelagic samples from Erken could be the proportion of bubbles. Both the litoral and the pelagic samples from Erken encompass 6 bubble layers, however there is an additional vertically extended layer in the pelagic samples which increases the areal proportion of bubbles. This is consistent with litterature indicating increased area of impurities entail a significant decrease in compressive strength (Qi et al., 2017).

However, the tendency of increased number of impurities have not been observed in the pelagic ice cores. Indicating there is an additional factor decreasing the strength of the pelagic ice, or increasing the strength of the litoral ice.

4.2.3 Compressive Strength in Different Orientations

When comparing the uncalibrated compressive strengths of different orientations there is not a clear trend of larger or smaller compressive strengths. However, the vertical compressive strength is generally slightly larger than most orientations in both pelagic and litoral samples, which is consistent with previous research comparing vertical and horizontal strengths of ice (Lian et al., 2017).

An interesting trend is the large differences in compressive strength between the coupled 90° orientations at both localities, i.e. 30°-120°, 60°-150° and 0°-90°.

If we expect the crystals of the transparent ice to mainly grow vertically or horizontally we would expect different strengths of the vertical(0°) and the horizontal(90°) orientations. Accordingly, due to symmetry, the 30° orientation and 120° orientation should show similar strengths, as well as the 60° orientation and the 150° orientation.

However, in several instances the measurements show considerably large differences in uncalibrated compressive strength between these 90° coupled angles. This indicate there is no 90° symmetry which further implies the grain boundaries are not straight. This could possibly be the result of grain boundary migration due to local variations of internal stress of the ice.

Chapter 5

Conclusion

- The investigated cores show two distinct structural patterns, the cores from Trehörningen consists of a transparent S1 ice topped with a thin layer of a superimposed T1 snowice. The cores from Valloxen and Fysingen consists of layers of larger semisphere ice crystals in a fine grained matrix, which can not be explained with current formation models. Further research of microstructures in lake ice is required to complement current ice characterization.

- The measured uncalibrated compressive strength of the investigated ice cores indicate a larger strength in the transparent ice compared to the opaque ice transition zone, which is consistent with previous research (Butkovich, 1954b, 1954a).

  Additionally, the uncalibrated compressive strengths from both ice cores and cubes indicate a larger compressive strength in litoral samples compared to pelagic samples.

  There are also tendencies of slightly larger uncalibrated compressive strength in the vertical orientation compared to horizontal, 30°, 60°, 120° and 150°.

  However, all uncalibrated strength measurements preformed with the ultrasound requires calibration with rebound number and lab based uniaxial compression tests.

Acknowledgements

Firstly I would like to thank my supervisors Mark Peternell and Kevin Vikström, for supporting me and always showing great interest in my thesis work. I would also like to thank Carina Liebl for helping me with equipment and instrument handling. I also thank my opponent Sofía Rodas and my examinator Philipp Wanner for constructive comments.

References

Ashton, G. D. (1986). *River and lake ice engineering*. Water Resources Publication.

Barrette, P. D. (2011). A laboratory study on the flexural strength of white ice and clear ice from the rideau canal skateway. *Canadian Journal of Civil Engineering*, *38*(12), 1435–1439.

Bengtsson, L. (1986). Spatial variability of lake ice covers. *Geografiska Annaler: Series A, Physical Geography*, *68*(1-2), 113–121.

Brockamp, B., & Querfurth, H. (1964). Untersuchungen über die elastizitätskonstanten von see-und kunsteis. *Polarforschung*, *34*(1/2), 253–262.

Butkovich, T. R. (1954a). *Hardness of single ice crystals* (Vol. 9). Snow, Ice and Permafrost Research Establishment, Corps of Engineers, US Army.

Butkovich, T. R. (1954b). *Ultimate strength of ice* (Vol. 11). Snow, Ice and Permafrost Research Establishment, Corps of Engineers, US Army.

Delesky, E. A., & Srubar, W. V. (2022). Ice-binding proteins and bioinspired synthetic mimics in non-physiological environments. *Iscience*.

Desideri, U., Proietti, S., & Sdringola, P. (2009). Solar-powered cooling systems: Technical and economic analysis on industrial refrigeration and air-conditioning applications. *Applied Energy*, *86*(9), 1376–1386.

Gow, A. J. (1986). Orientation textures in ice sheets of quietly frozen lakes. *Journal of crystal growth*, *74*(2), 247–258.

Green Jr, R. E., & Mackinnon, L. (1956). Determination of the elastic constants of ice single crystals by an ultrasonic pulse method. *The Journal of the Acoustical Society of America*, *28*(6), 1292–1292.

Haji-Akbari, A. (2020). Ice and its formation. *Antifreeze Proteins Volume 1: Environment, Systematics and Evolution*, 13–51.

Hammes, D. M., & Peternell, M. (2016). Fame: Software for analysing rock microstructures. *Computers & Geosciences*, *90*, 24–33.

Hanley, T., & Rao, S. (1982). *Acoustic detector for frazil* (Vol. 1).

Hellmann, S., Grab, M., Kerch, J., Löwe, H., Bauder, A., Weikusat, I., & Maurer, H. (2021). Acoustic velocity measurements for detecting the crystal orientation fabrics of a temperate ice core. *The Cryosphere*, *15*(7), 3507–3521.

Kirillin, G., Leppäranta, M., Terzhevik, A., Granin, N., Bernhardt, J., Engelhardt, C., … others (2012). Physics of seasonally ice-covered lakes: a review. *Aquatic sciences*, *74*, 659–682.

Kivisild, H., & Iyer, S. (1976). In situ tests for ice strength measurements. *Ocean Engineering*, *3*(5), 329–342.

Leppäranta, M. (2014). *Freezing of lakes and the evolution of their ice cover*. Springer Science & Business Media.

Lian, J., Ouyang, Q., Zhao, X., Liu, F., & Qi, C. (2017). Uniaxial compressive strength and fracture mode of lake ice at moderate strain rates based on a digital speckle correlation method for deformation measurement. *Applied Sciences*, *7*(5), 495.

Masterson, D. (1996). Interpretation of in situ borehole ice strength measurement tests. *Canadian Journal of Civil Engineering*, *23*(1), 165–179.

Michel, B. (1978). Ice mechanics.

Michel, B., & Ramseier, R. O. (1971). Classification of river and lake ice. *Canadian Geotechnical Journal*, *8*(1), 36–45.

Müller-Stoffels, M., Langhorne, P. J., Petrich, C., & Kempema, E. W. (2009). Preferred crystal orientation in fresh water ice. *Cold regions science and technology*, *56*(1), 1–9.

Murat, J., Ladanyi, B., & Huneault, P. (1989). In situ determination of creep properties of sea ice with the pressuremeter. *Canadian Geotechnical Journal*, *26*(4), 575–594.

Peternell, M., Kohlmann, F., Wilson, C. J., Seiler, C., & Gleadow, A. J. (2009). A new approach to crystallographic orientation measurement for apatite fission track analysis: effects of crystal morphology and implications for automation. *Chemical Geology*, *265*(3-4), 527–539.

Peternell, M., Russell-Head, D., & Wilson, C. (2011). A technique for recording polycrystalline structure and orientation during in situ deformation cycles of rock analogues using an automated fabric analyser. *Journal of Microscopy*, *242*(2), 181–188.

Petrenko, V. F., & Whitworth, R. W. (1999). *Physics of ice*. OUP Oxford.

Qi, C., Lian, J., Ouyang, Q., & Zhao, X. (2017). Dynamic compressive strength and failure of natural lake ice under moderate strain rates at near melting point temperature. *Latin American journal of solids and structures*, *14*, 1669–1694.

Ramløv, H., & Friis, D. S. (2020). *Antifreeze proteins volume 1: Environment, systematics and evolution.* Springer Nature.

Roethlisberger, H. (1966). Ultrasonic pulse measurements in anisotropic lake ice.

Schwarz, J., Frederking, R., Gavrillo, V., Petrov, I., Hirayama, K.-I., Mellor, M., … Vaudrey, K. (1981). Standardized testing methods for measuring mechanical properties of ice. *Cold Regions Science and Technology*, *4*(3), 245–253.

Selçuk, L., & Nar, A. (2016). Prediction of uniaxial compressive strength of intact rocks using ultrasonic pulse velocity and rebound-hammer number..

Sharma, S., Blagrave, K., Magnuson, J. J., O'Reilly, C. M., Oliver, S., Batt, R. D., … others (2019). Widespread loss of lake ice around the northern hemisphere in a warming world. *Nature Climate Change*, *9*(3), 227–231.

Sharma, S., Blagrave, K., Watson, S. R., O'Reilly, C. M., Batt, R., Magnuson, J. J., … others (2020). Increased winter drownings in ice-covered regions with warmer winters. *PLoS One*, *15*(11), e0241222.

SMHI. (n.d.). *PTHBV Database.* Retrieved Retrieved 2023-04-13, from `https://www.smhi.se/data/ladda-ner-data/griddade-nederbord-och-temperaturdata-pthbv`

SMHI & HavsVatten myndigheten. (n.d.). *Damm- och sjöregister.* Retrieved Retrieved 2023-04-18, from `https://vattenwebb.smhi.se/svarwebb/`

Weyhenmeyer, G. A., Obertegger, U., Rudebeck, H., Jakobsson, E., Jansen, J., Zdorovennova, G., … others (2022). Towards critical white ice conditions in lakes under global warming. *Nature communications*, *13*(1), 4974.

Wilson, C. J., RUSSELL-HEAD, D. S., Kunze, K., & Viola, G. (2007). The analysis of quartz c-axis fabrics using a modified optical microscope. *Journal of Microscopy*, *227*(1), 30–41.

Appendix A - Grain Geometry Analysis

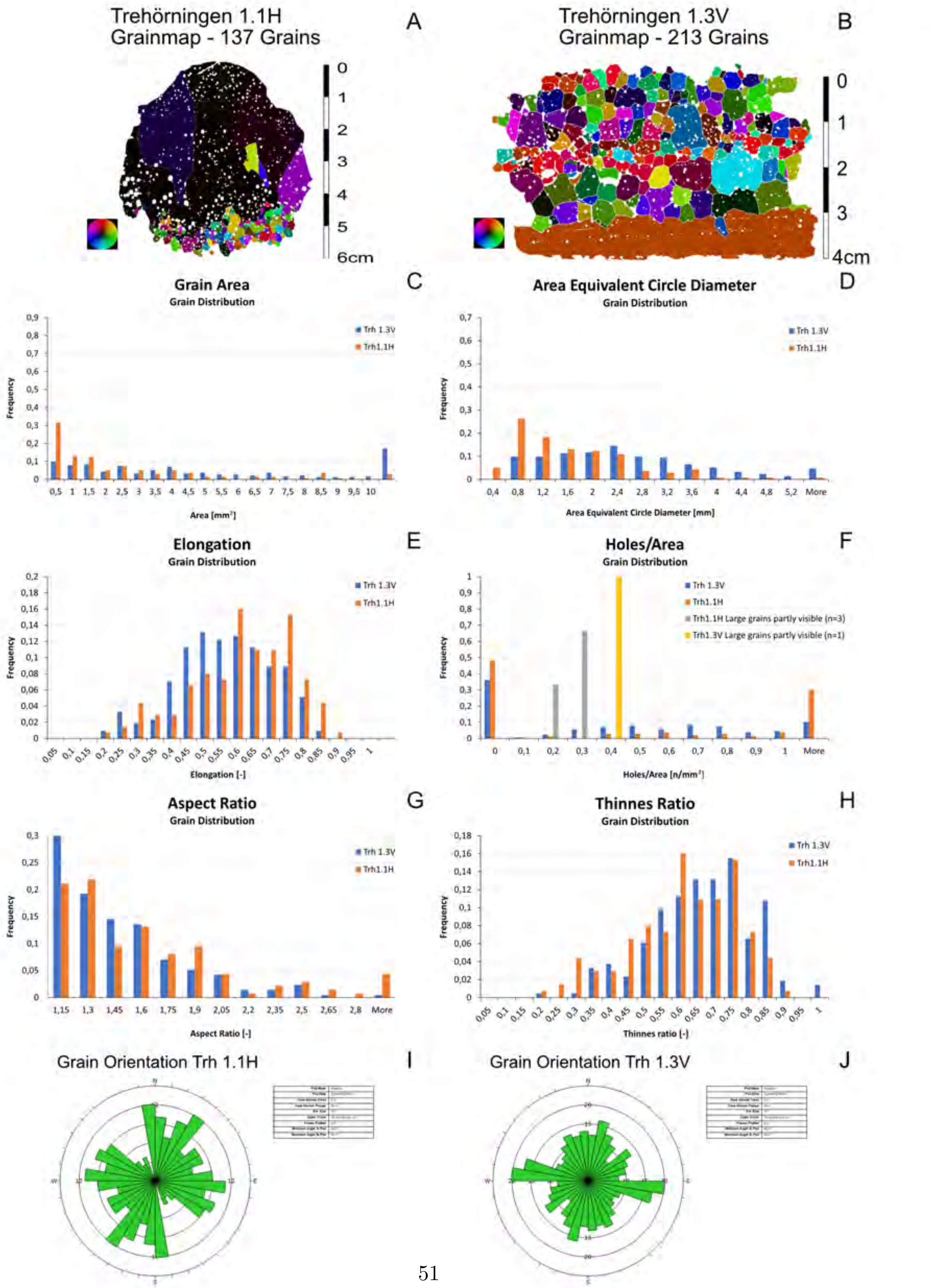

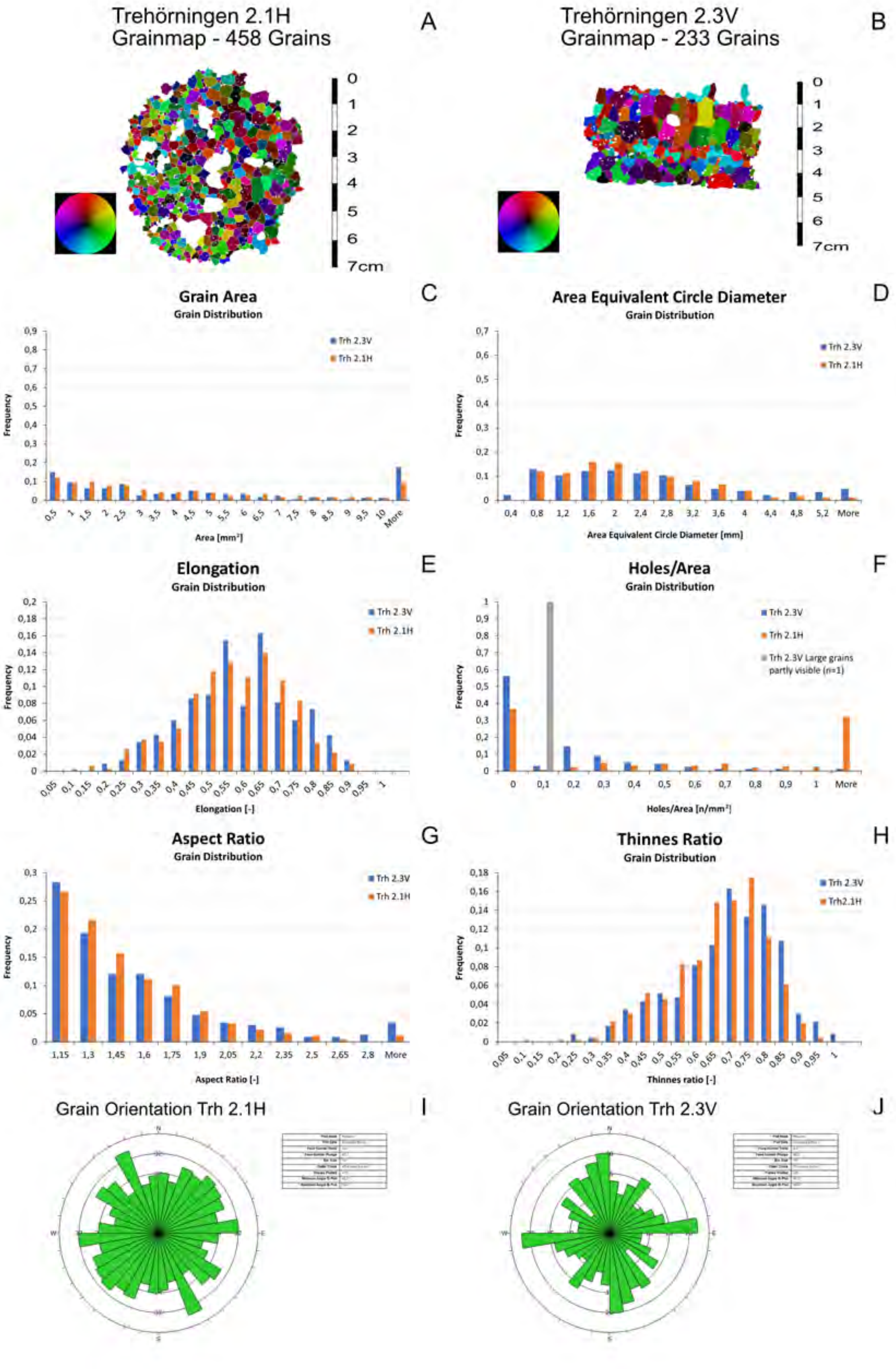

Figure 5.2: A) Grainmap of thin section Trehörningen 2.1H. B) Grainmap of corresponding vertical thin section Trehörningen 2.3V C) Area distribution and frequency of grains from section Trh2.1H & Trh2.3V D) The equal area diameter(EAD) distribution and frequency of the grains from section Trh2.1H & Trh2.3V. E) The elongation distribution and frequency of the grains from section Trh2.1H & Trh2.3V. F) The distribution and frequency of holes/area in the grains from section Trh2.1H & Trh2.3V, separated by grains who are entirely in the section and grains partly included in the section. G) The aspect ratio distribution and frequency of the grains from section Trh2.1H & Trh2.3V. H) The Thinnes ratio distribution and frequency of the grains from section Trh2.1H & Trh2.3V. I) Rosediagram of grain orientation distribution & frequency of grains from section Trh 2.1H. J) Rosediagram of grain orientation distribution & frequency of grains from section Trh 2.3V.

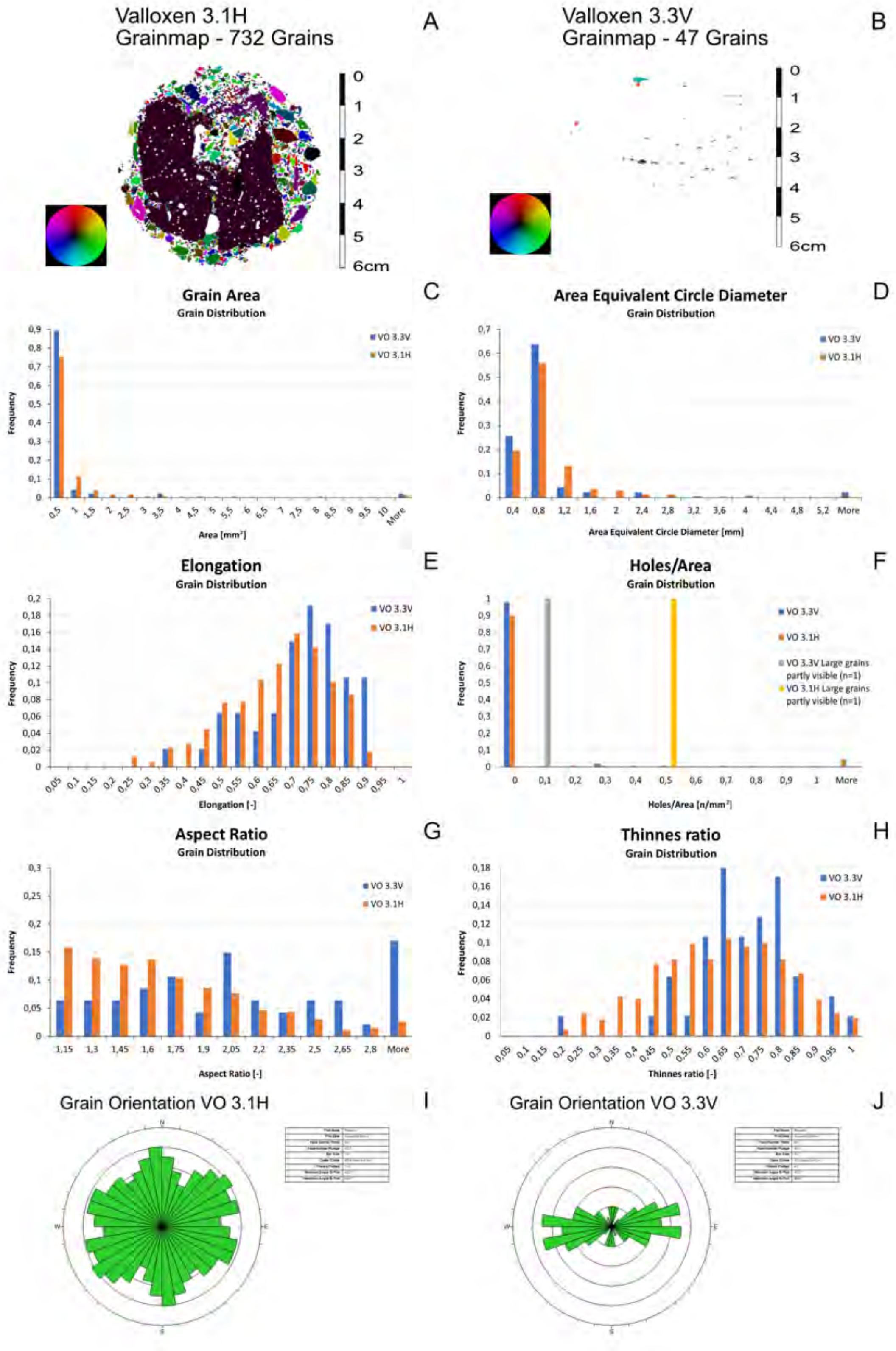

Figure 5.3: A) Grainmap of thin section Valloxen 3.1H. B) Grainmap of corresponding vertical thin section Valloxen 3.3V C) Area distribution and frequency of grains from section VO3.1H & VO3.3V D) The equal area diameter(EAD) distribution and frequency of the grains from section VO3.1H & VO3.3V. E) The elongation distribution and frequency of the grains from section VO3.1H & VO3.3V. F) The distribution and frequency of holes/area in the grains from section VO3.1H & VO3.3V, separated by grains who are entirely in the section and grains partly included in the section. G) The aspect ratio distribution and frequency of the grains from section VO3.1H & VO3.3V. H) The Thinnes ratio distribution and frequency of the grains from section VO3.1H & VO3.3V. I) Rosediagram of grain orientation distribution & frequency of grains from section VO3.1H. J) Rosediagram of grain orientation distribution & frequency of grains from section VO3.3V.

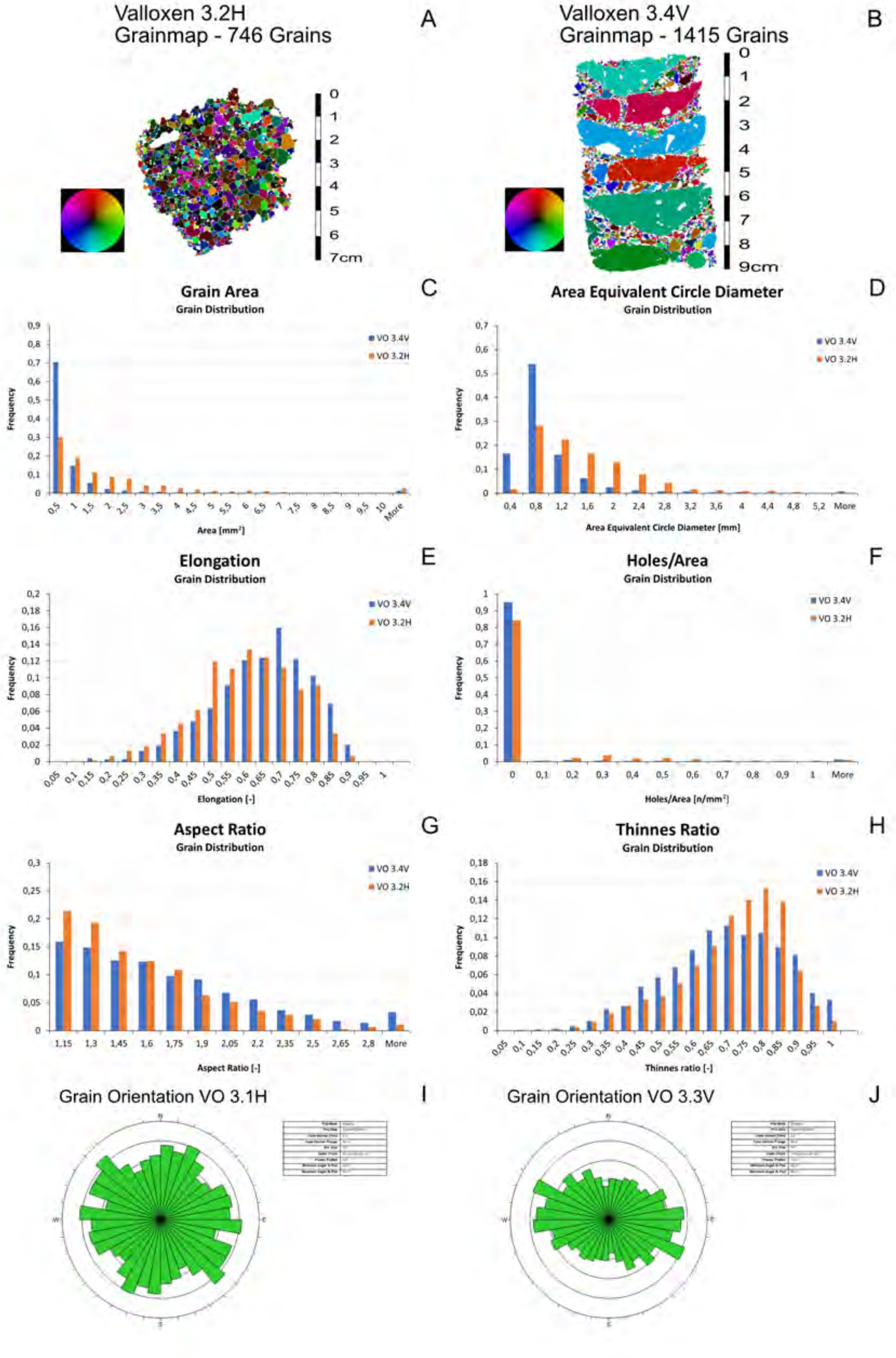

Figure 5.4: A) Grainmap of thin section Valloxen 3.2H. B) Grainmap of corresponding vertical thin section Valloxen 3.4V C) Area distribution and frequency of grains from section VO3.2H & VO3.4V D) The equal area diameter(EAD) distribution and frequency of the grains from section VO3.2H & VO3.4V. E) The elongation distribution and frequency of the grains from section VO3.2H & VO3.4V. F) The distribution and frequency of holes/area in the grains from section VO3.2H & VO3.4V. G) The aspect ratio distribution and frequency of the grains from section VO3.2H & VO3.4V. H) The Thinnes ratio distribution and frequency of the grains from section VO3.2H & VO3.4V. I) Rosediagram of grain orientation distribution & frequency of grains from section VO3.2H. J) Rosediagram of grain orientation distribution & frequency of grains from section VO3.4V.

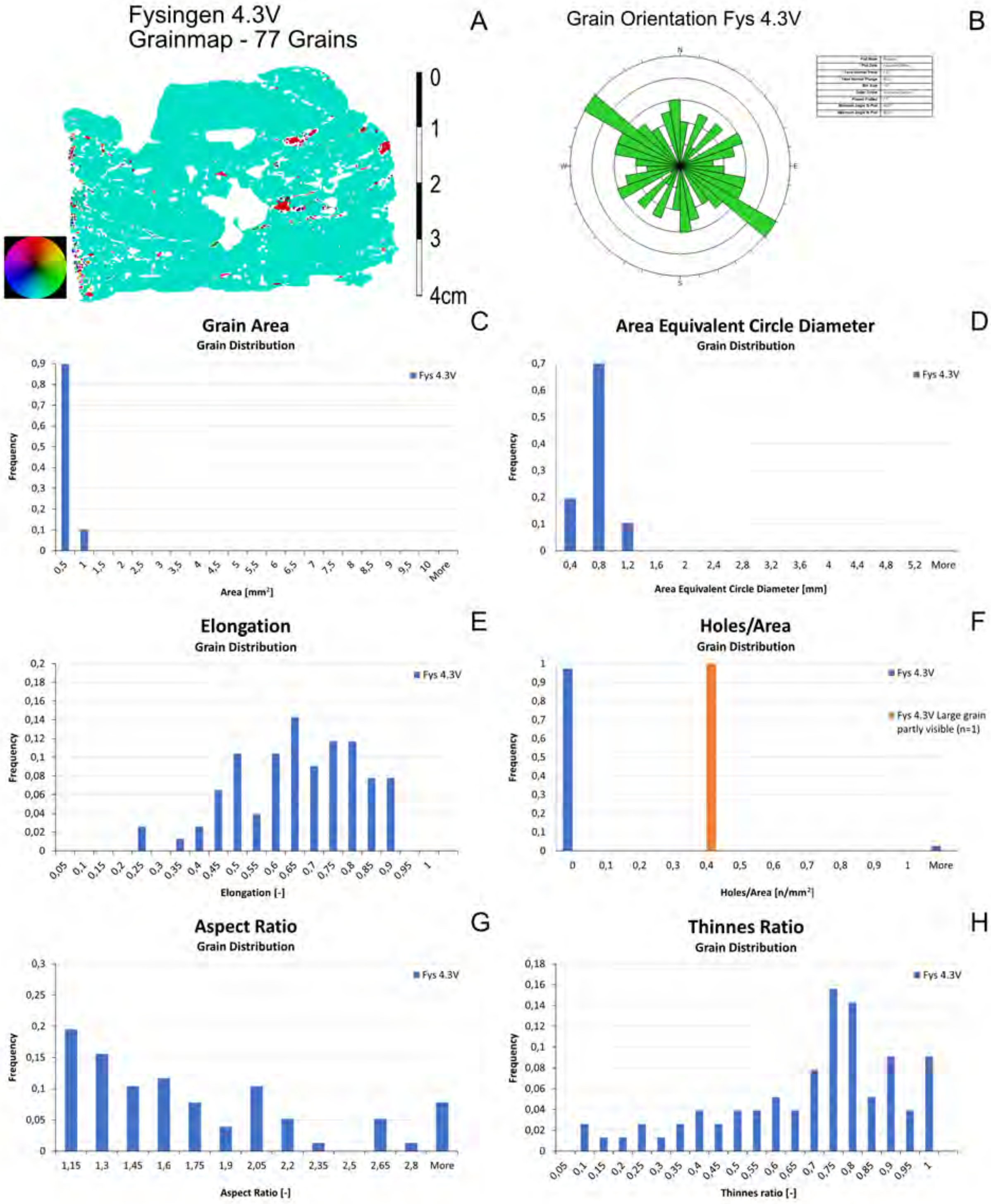

Figure 5.5: A) Grainmap of thin section Fysingen 4.3v. B) Rosediagram of grain orientation distribution & frequency of grains from section Fys4.3V. C) Area distribution and frequency of grains from section Fys4.3V. D) The equal area diameter(EAD) distribution and frequency of the grains from section Fys4.3V. E) The elongation distribution and frequency of the grains from section Fys4.3V. F) The distribution and frequency of holes/area in the grains from section Fys4.3V, separated by grains who are entirely in the section and grains partly included in the section. G) The aspect ratio distribution and frequency of the grains from section Fys4.3V. H) The Thinnes ratio distribution and frequency of the grains from section Fys4.3V.

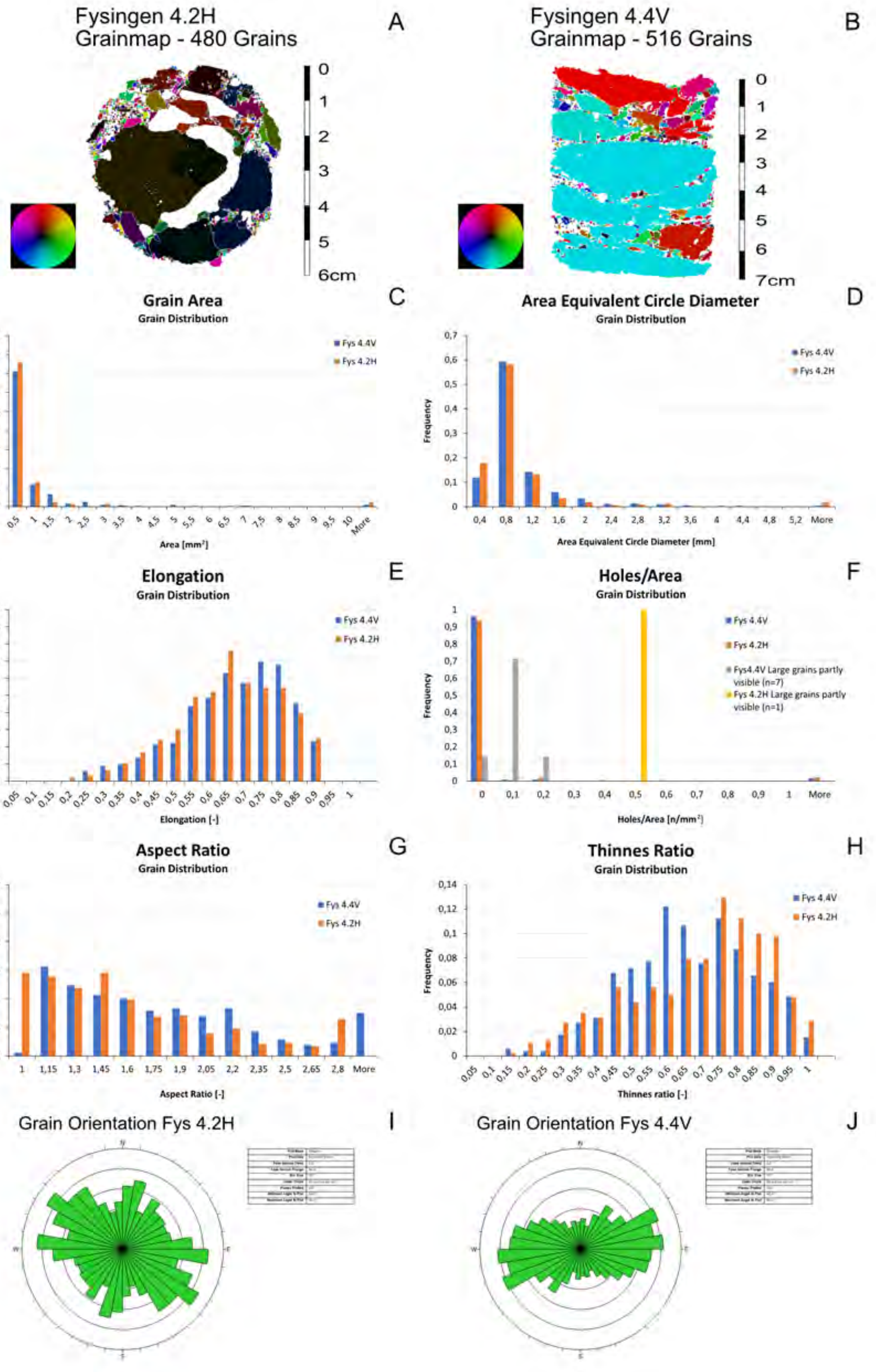

Figure 5.6: A) Grainmap of thin section Fysingen 4.2H. B) Grainmap of corresponding vertical thin section Fysingen 4.4V. C) Area distribution and frequency of grains from section Fys4.2H & Fys4.4V. D) The equal area diameter(EAD) distribution and frequency of the grains from section Fys4.2H & Fys4.4V. E) The elongation distribution and frequency of the grains from section Fys4.2H & Fys4.4V. F) The distribution and frequency of holes/area in the grains from section Fys4.2H & Fys4.4V. G) The aspect ratio distribution and frequency of the grains from section Fys4.2H & Fys4.4V. H) The Thinnes ratio distribution and frequency of the grains from section Fys4.2H & Fys4.4V. I) Rosediagram of grain orientation distribution & frequency of grains from section Fys4.2H. J) Rosediagram of grain orientation distribution & frequency of grains from section Fys4.4V.

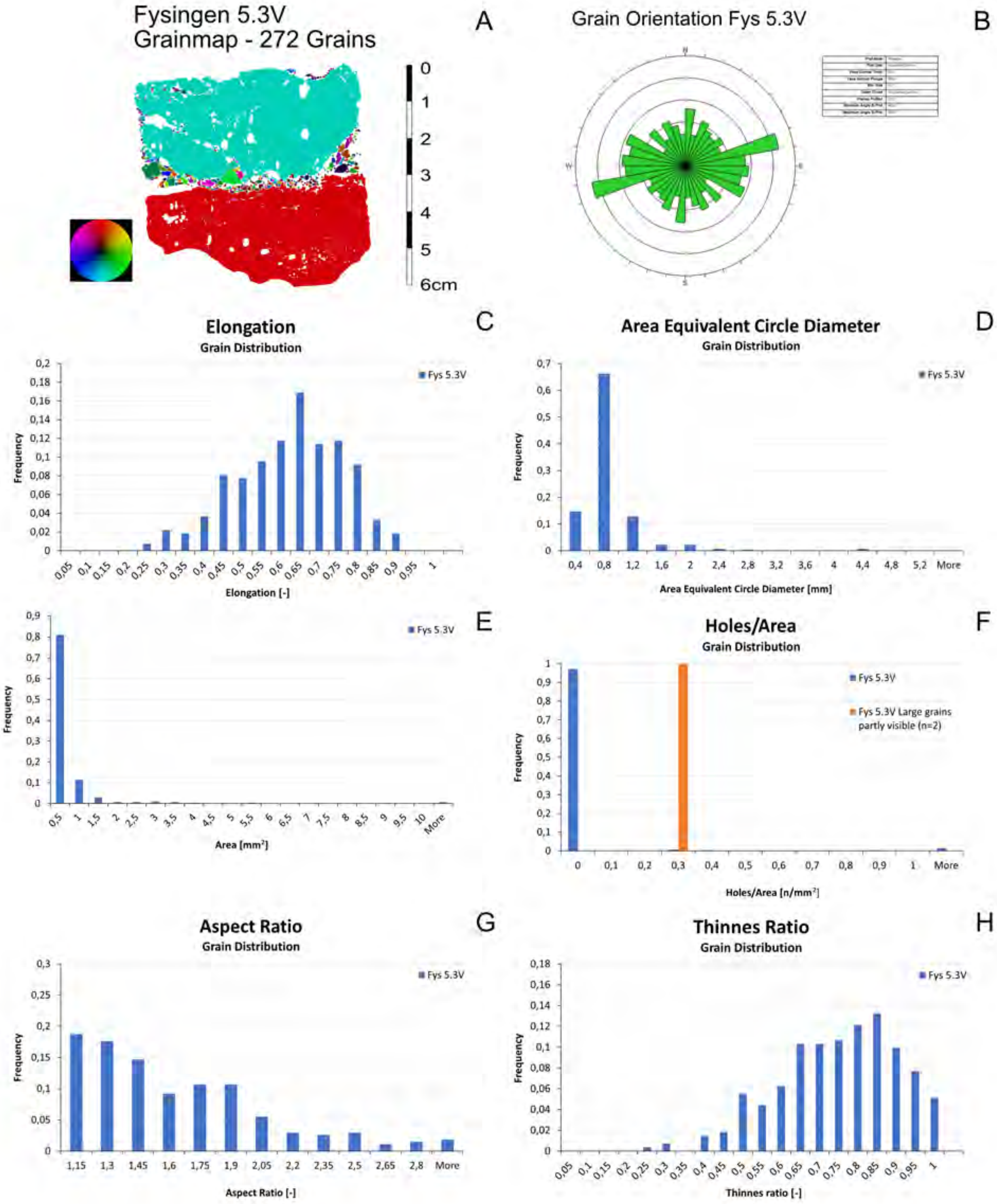

Figure 5.7: A) Grainmap of thin section Fysingen 5.3V. B) Rosediagram of grain orientation distribution & frequency of grains from section Fys5.3V. C) Area distribution and frequency of grains from section Fys5.3V. D) The equal area diameter(EAD) distribution and frequency of the grains from section Fys5.3V. E) The elongation distribution and frequency of the grains from section Fys5.3V. F) The distribution and frequency of holes/area in the grains from section Fys5.3V, separated by grains who are entirely in the section and grains partly included in the section. G) The aspect ratio distribution and frequency of the grains from section Fys5.3V. H) The Thinnes ratio distribution and frequency of the grains from section Fys5.3V.

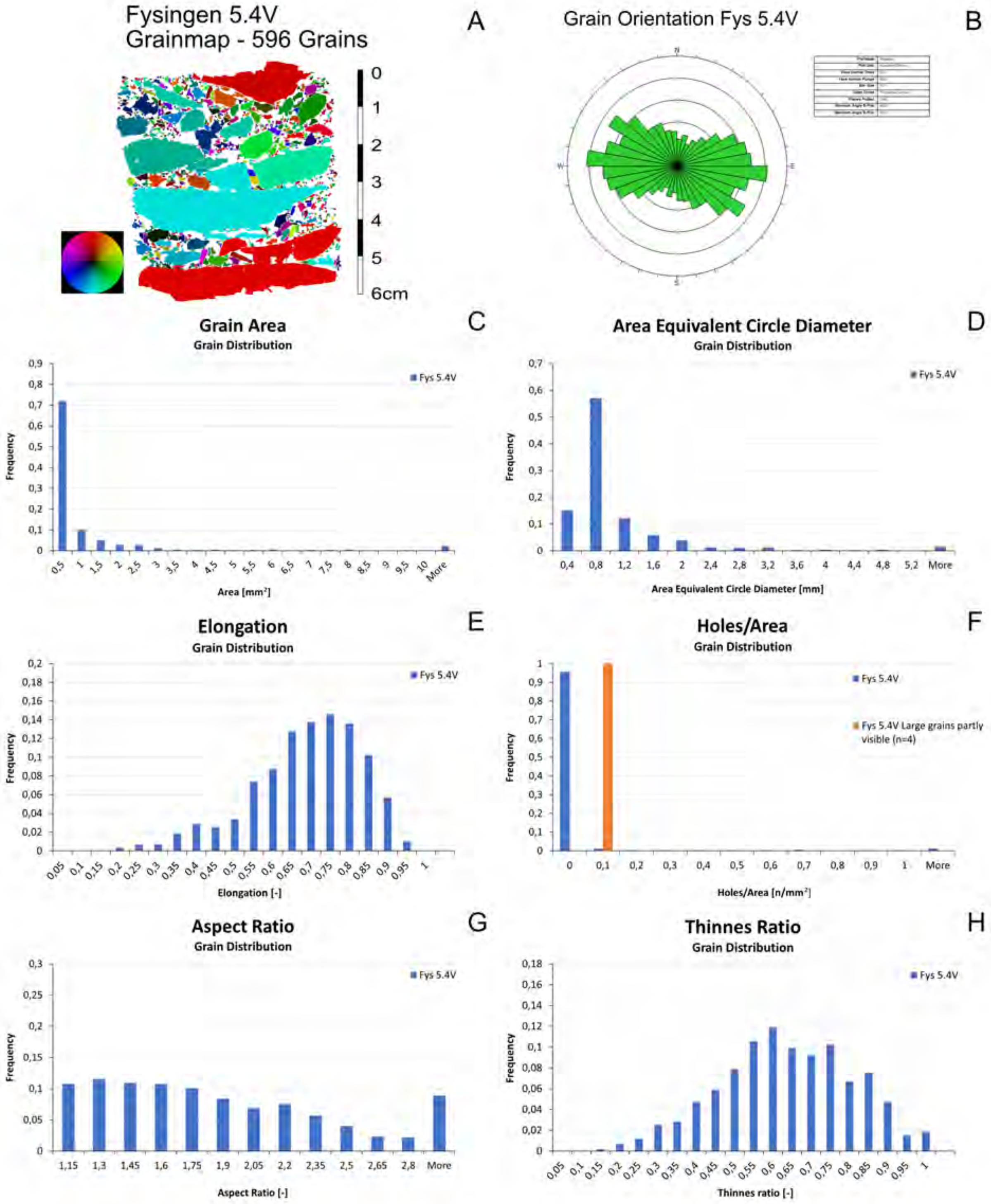

Figure 5.8: A) Grainmap of thin section Fysingen 5.4V. B) Rosediagram of grain orientation distribution & frequency of grains from section Fys5.4V. C) Area distribution and frequency of grains from section Fys5.4V. D) The equal area diameter(EAD) distribution and frequency of the grains from section Fys5.4V. E) The elongation distribution and frequency of the grains from section Fys5.4V. F) The distribution and frequency of holes/area in the grains from section Fys5.4V, separated by grains who are entirely in the section and grains partly included in the section. G) The aspect ratio distribution and frequency of the grains from section Fys5.4V. H) The Thinnes ratio distribution and frequency of the grains from section Fys5.4V.

Appendix B - High Resolution Photos

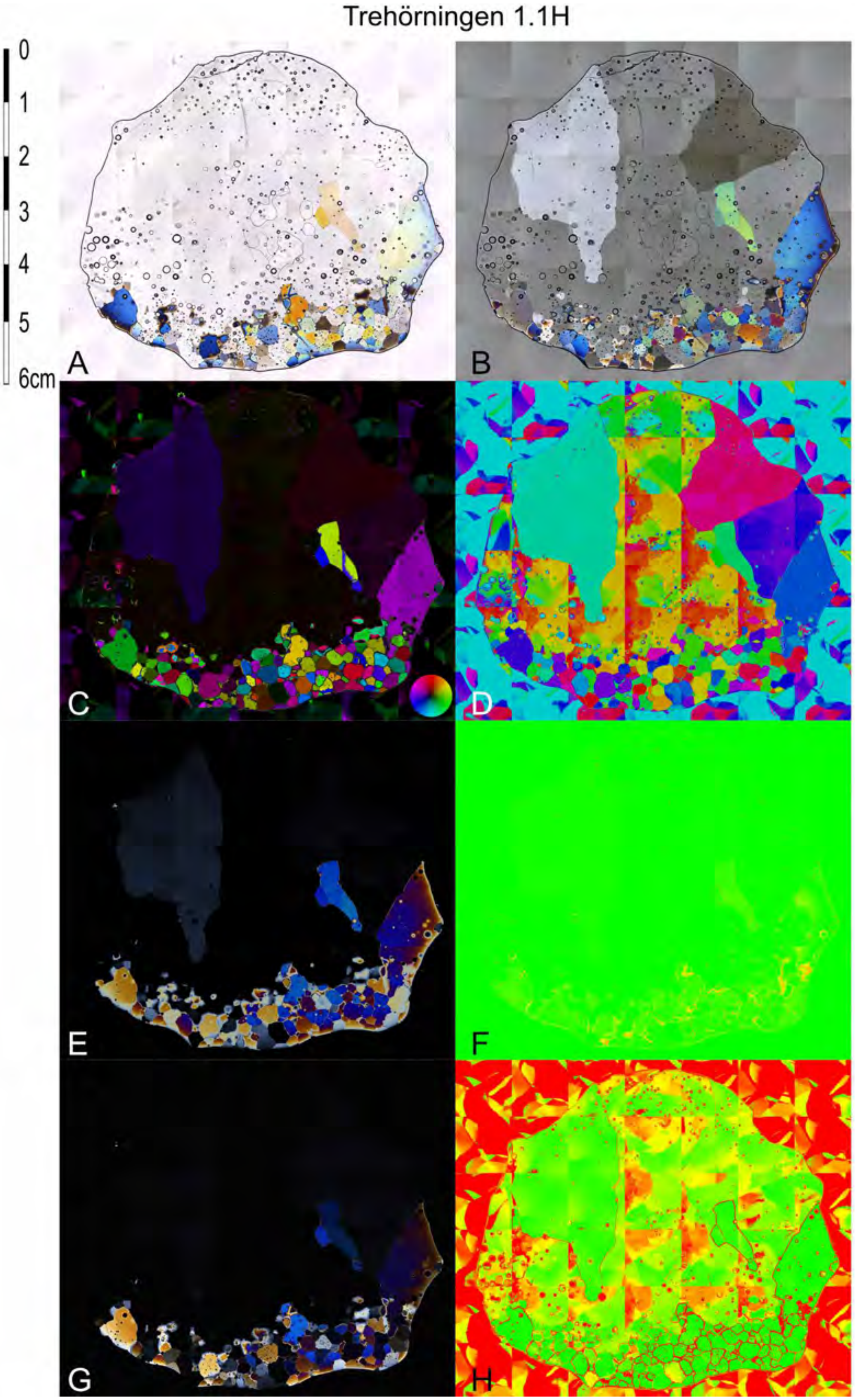

Figure 5.9: A) Plain polarized photo. B) Lambda 0 photo. C) c-axis orientation photo D) Flat trend c-axis orientation photo. E) Retardation photo. F) Retardation quality photo. G) Cross polarized photo. H) Geometric quality photo.

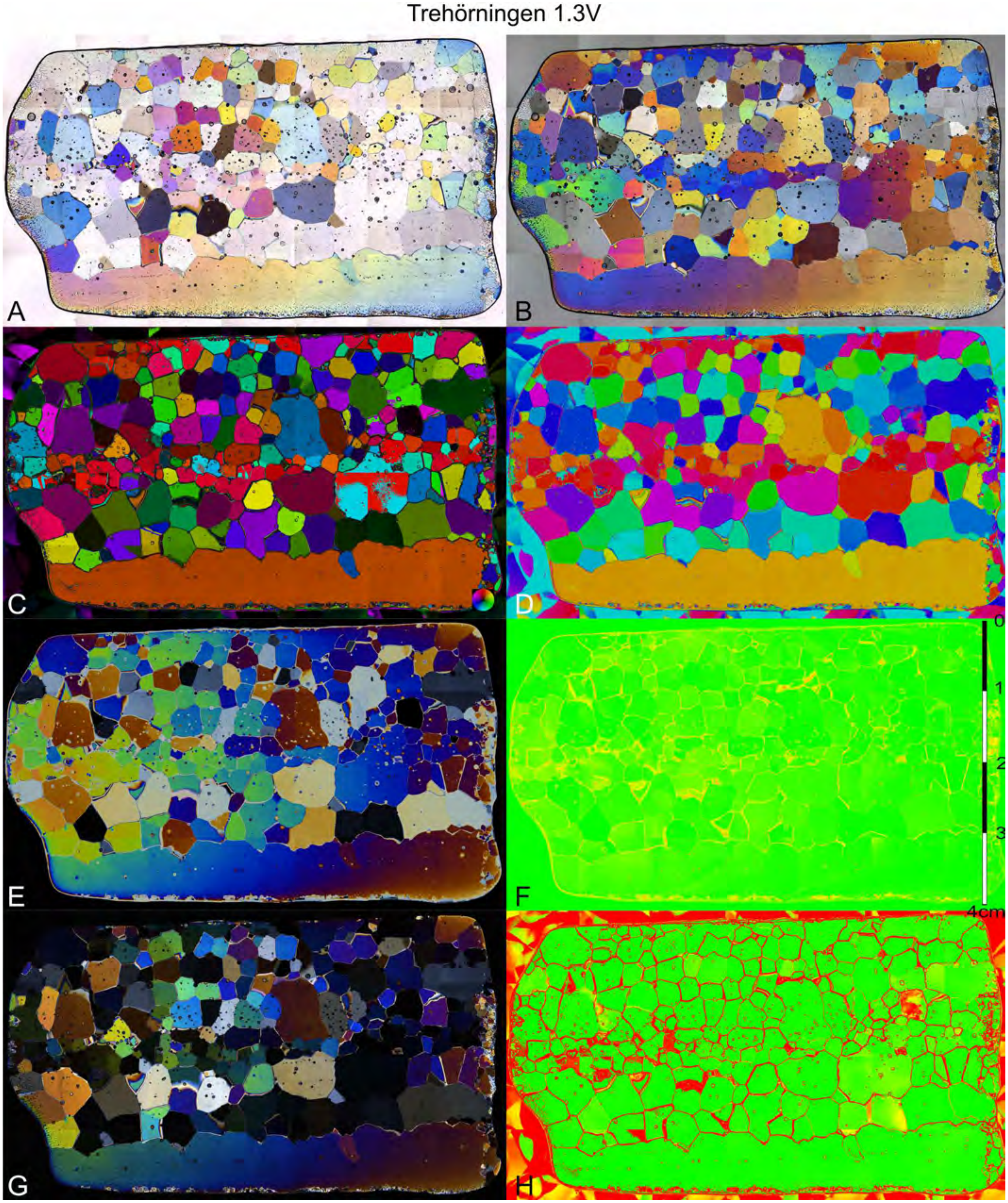

Figure 5.10: A) Plain polarized photo. B) Lambda 0 photo. C) c-axis orientation photo D) Flat trend c-axis orientation photo. E) Retardation photo. F) Retardation quality photo. G) Cross polarized photo. H) Geometric quality photo.

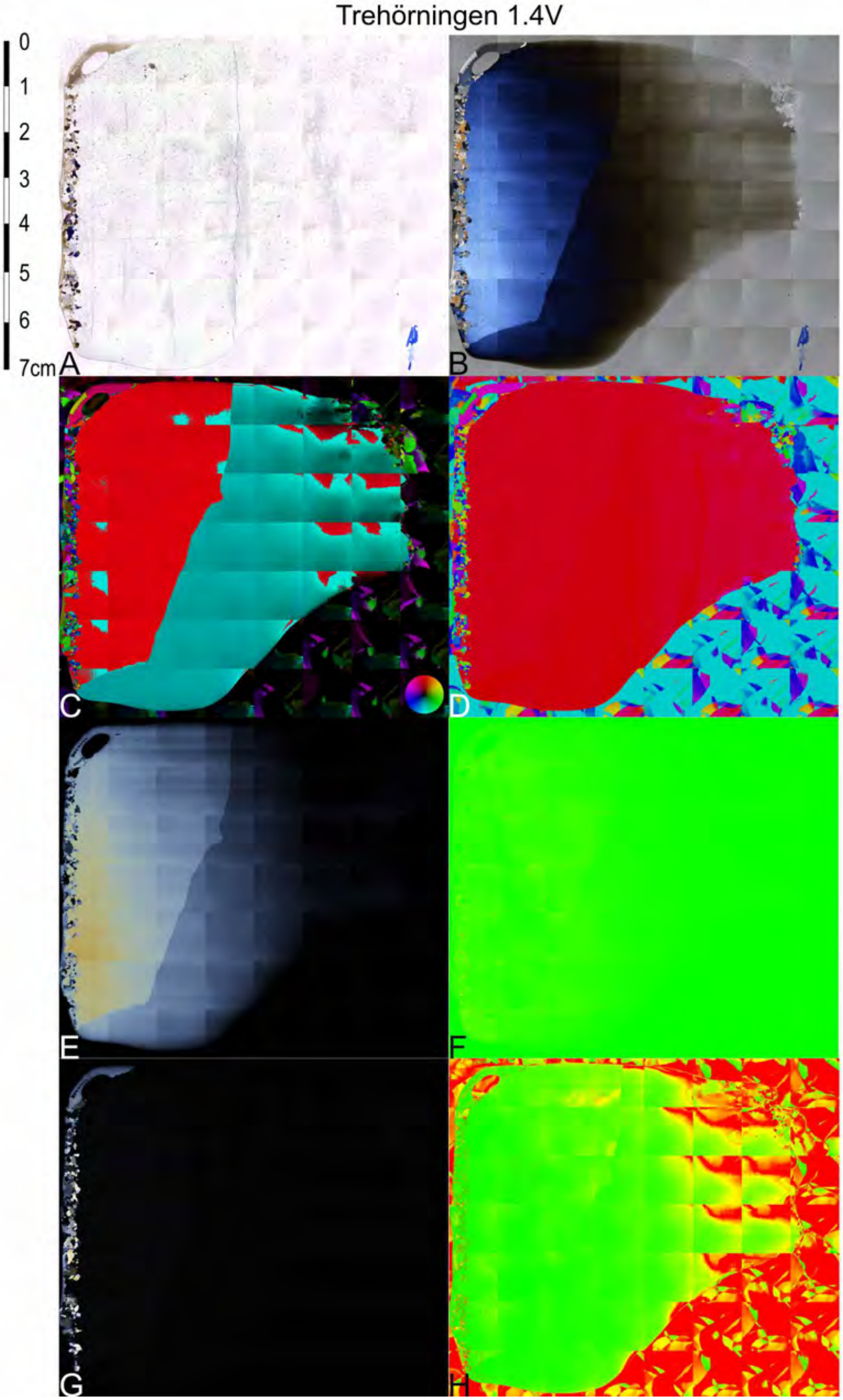

Figure 5.11: A) Plain polarized photo. B) Lambda 0 photo. C) c-axis orientation photo D) Flat trend c-axis orientation photo. E) Retardation photo. F) Retardation quality photo. G) Cross polarized photo. H) Geometric quality photo.

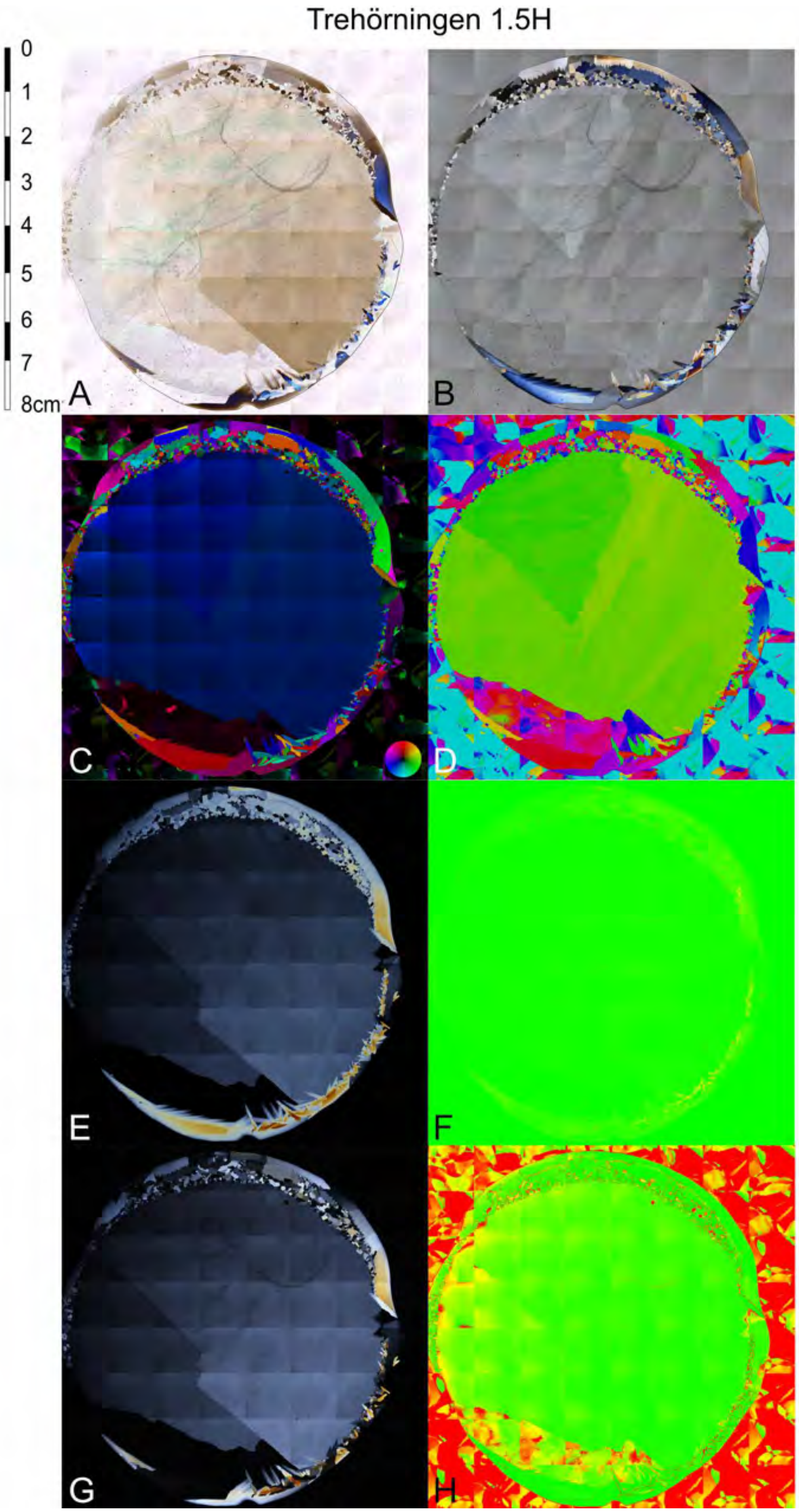

Figure 5.12: A) Plain polarized photo. B) Lambda 0 photo. C) c-axis orientation photo D) Flat trend c-axis orientation photo. E) Retardation photo. F) Retardation quality photo. G) Cross polarized photo. H) Geometric quality photo.

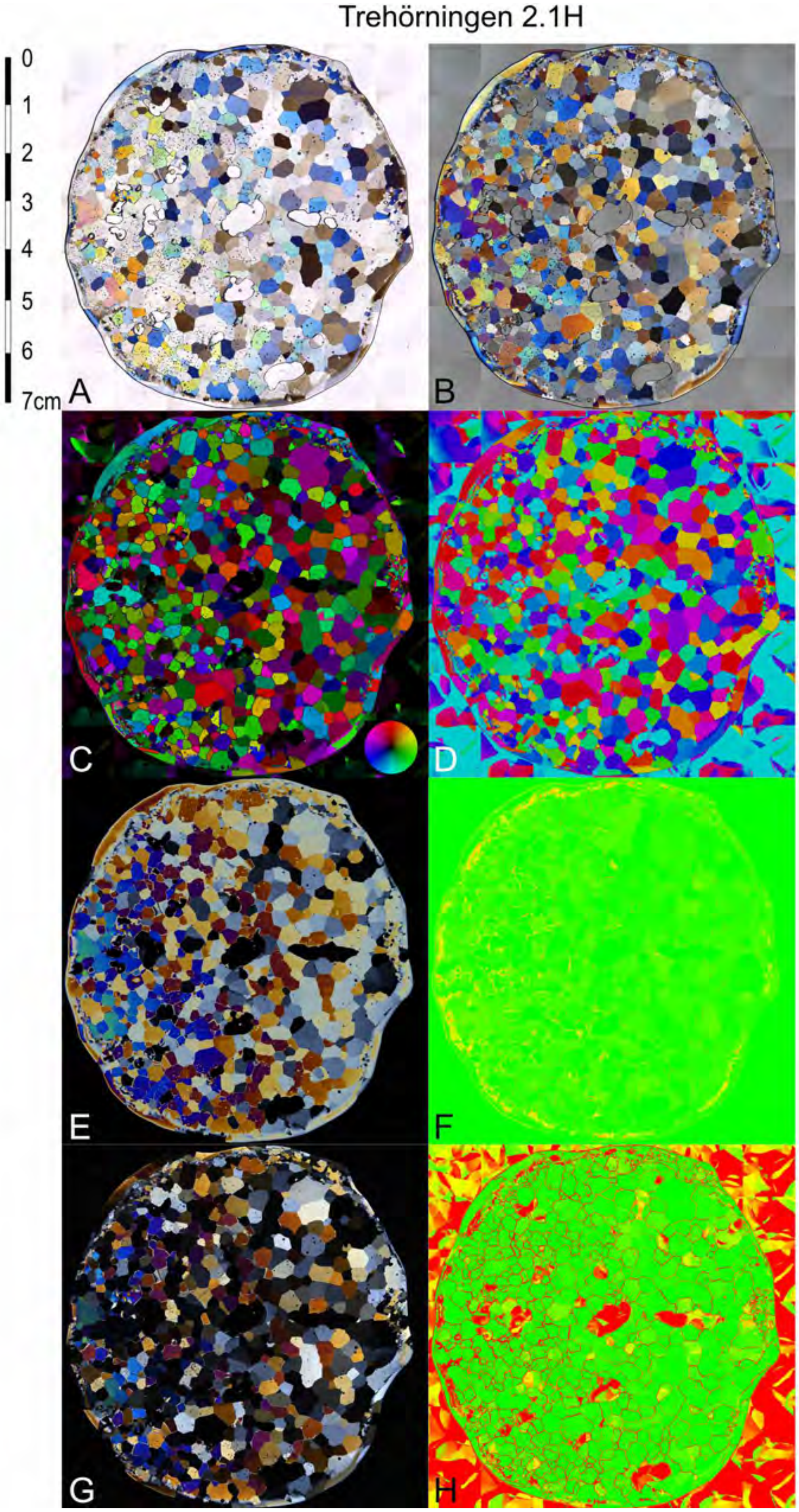

Figure 5.13: A) Plain polarized photo. B) Lambda 0 photo. C) c-axis orientation photo D) Flat trend c-axis orientation photo. E) Retardation photo. F) Retardation quality photo. G) Cross polarized photo. H) Geometric quality photo.

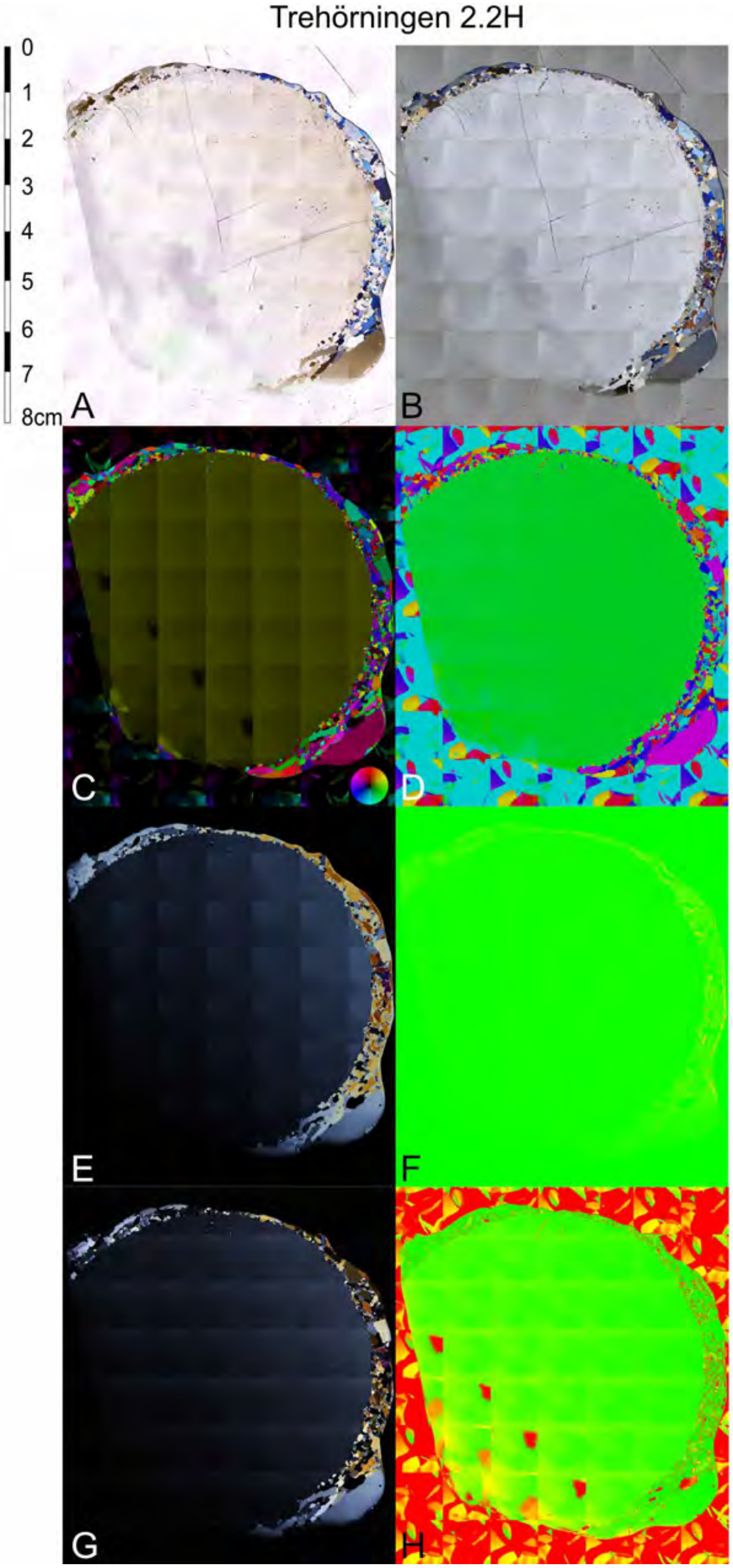

Figure 5.14: A) Plain polarized photo. B) Lambda 0 photo. C) c-axis orientation photo D) Flat trend c-axis orientation photo. E) Retardation photo. F) Retardation quality photo. G) Cross polarized photo. H) Geometric quality photo.

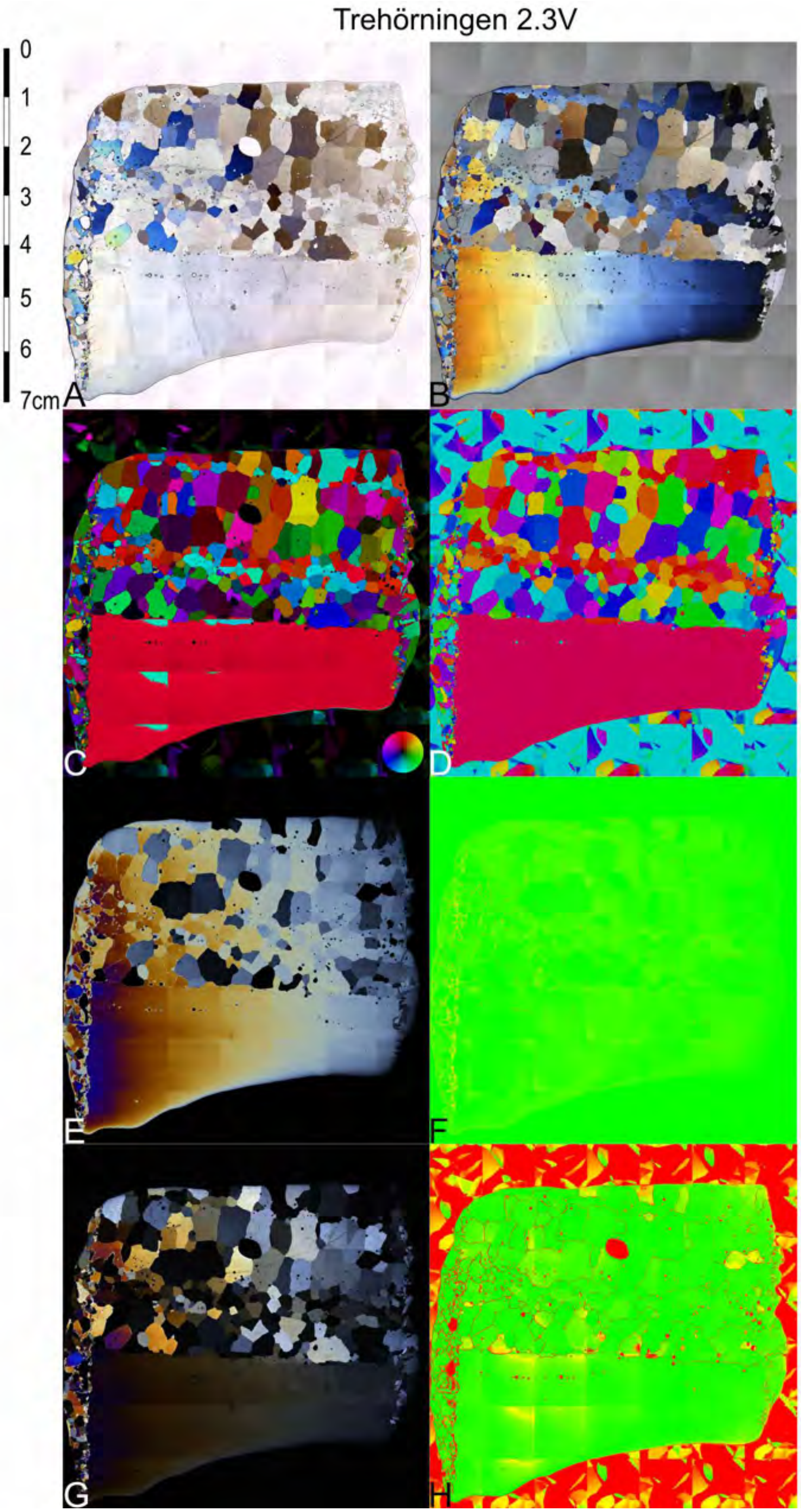

Figure 5.15: A) Plain polarized photo. B) Lambda 0 photo. C) c-axis orientation photo D) Flat trend c-axis orientation photo. E) Retardation photo. F) Retardation quality photo. G) Cross polarized photo. H) Geometric quality photo.

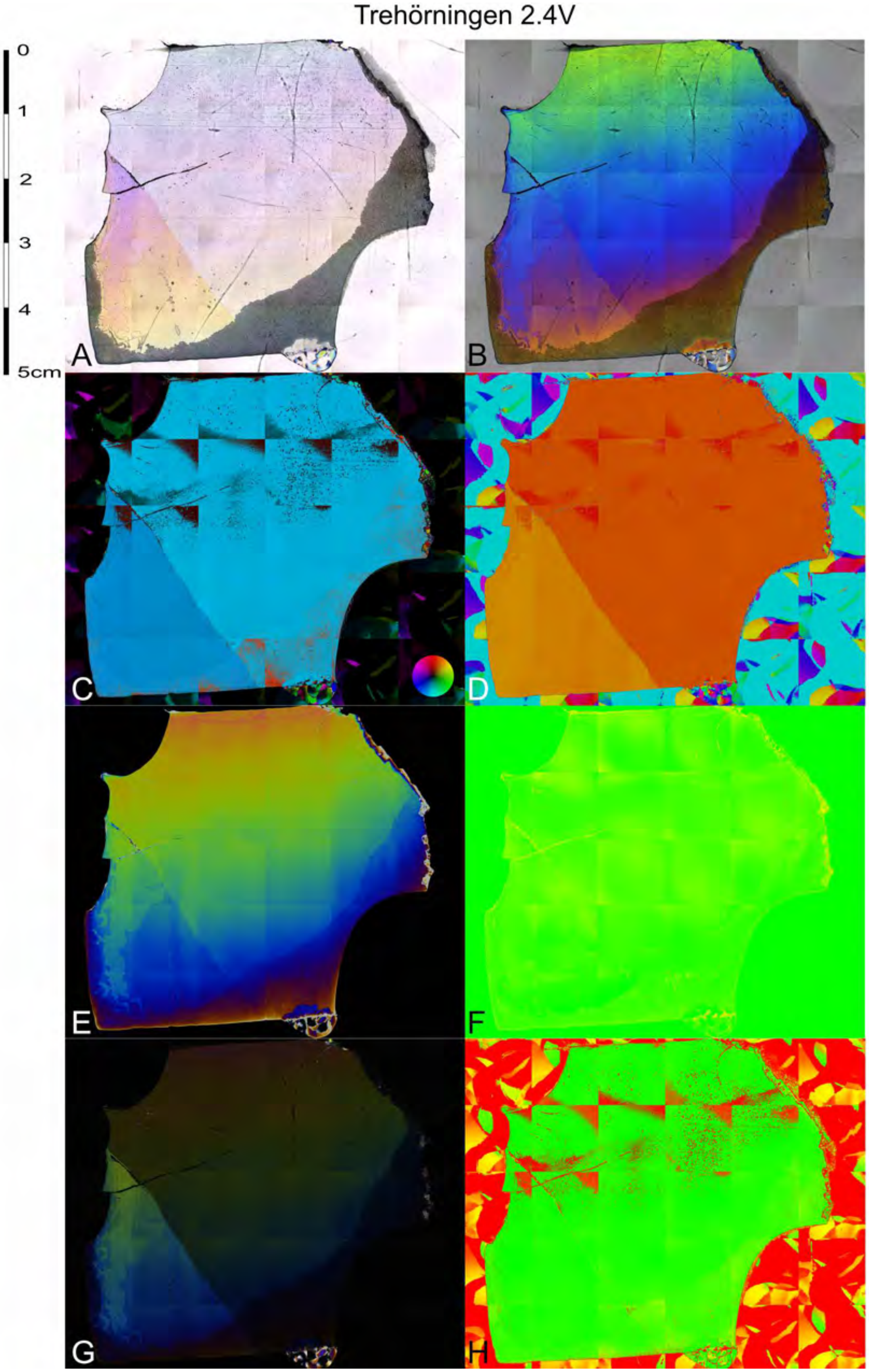

Figure 5.16: A) Plain polarized photo. B) Lambda 0 photo. C) c-axis orientation photo D) Flat trend c-axis orientation photo. E) Retardation photo. F) Retardation quality photo. G) Cross polarized photo. H) Geometric quality photo.

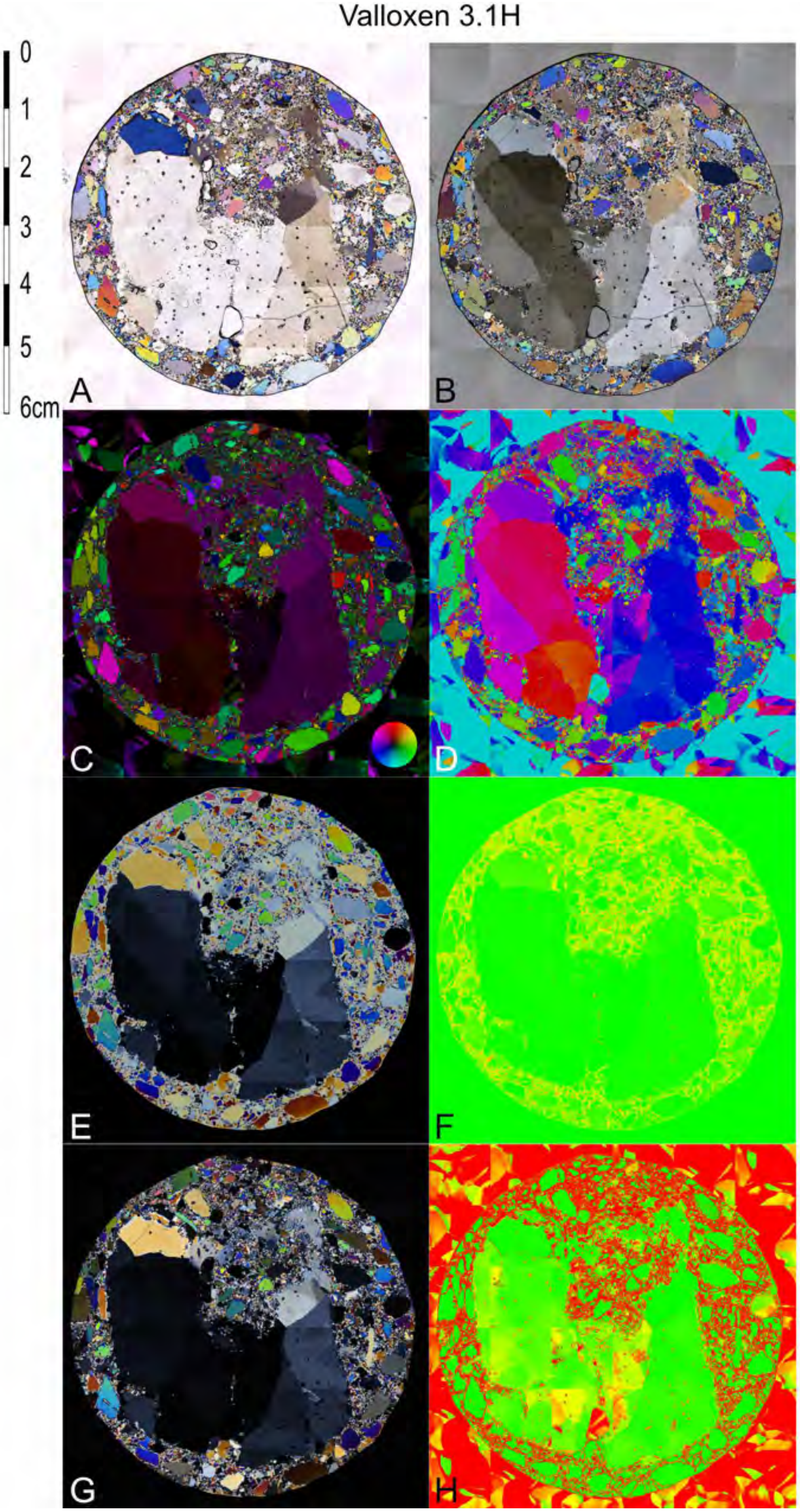

Figure 5.17: A) Plain polarized photo. B) Lambda 0 photo. C) c-axis orientation photo D) Flat trend c-axis orientation photo. E) Retardation photo. F) Retardation quality photo. G) Cross polarized photo. H) Geometric quality photo.

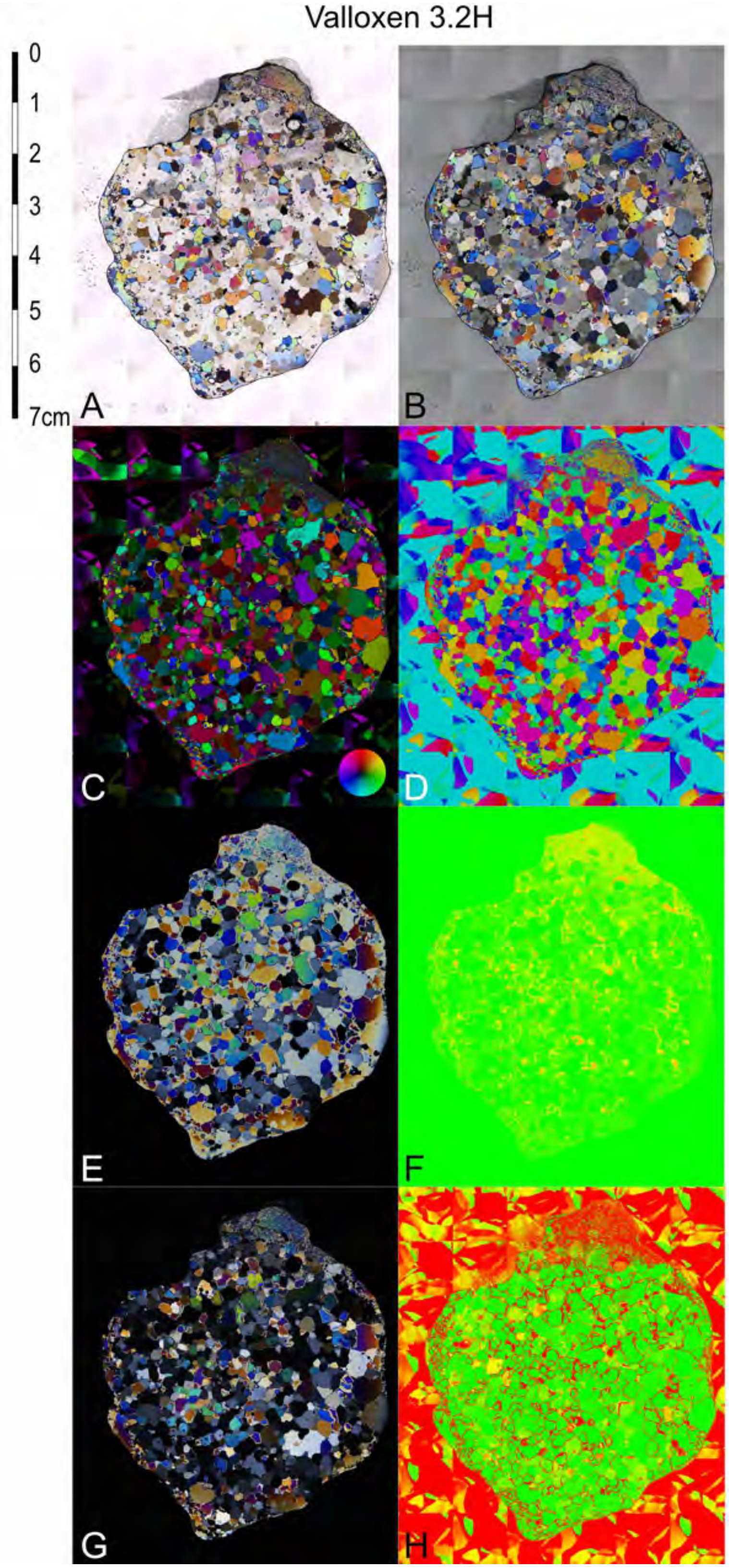

Figure 5.18: A) Plain polarized photo. B) Lambda 0 photo. C) c-axis orientation photo D) Flat trend c-axis orientation photo. E) Retardation photo. F) Retardation quality photo. G) Cross polarized photo. H) Geometric quality photo.

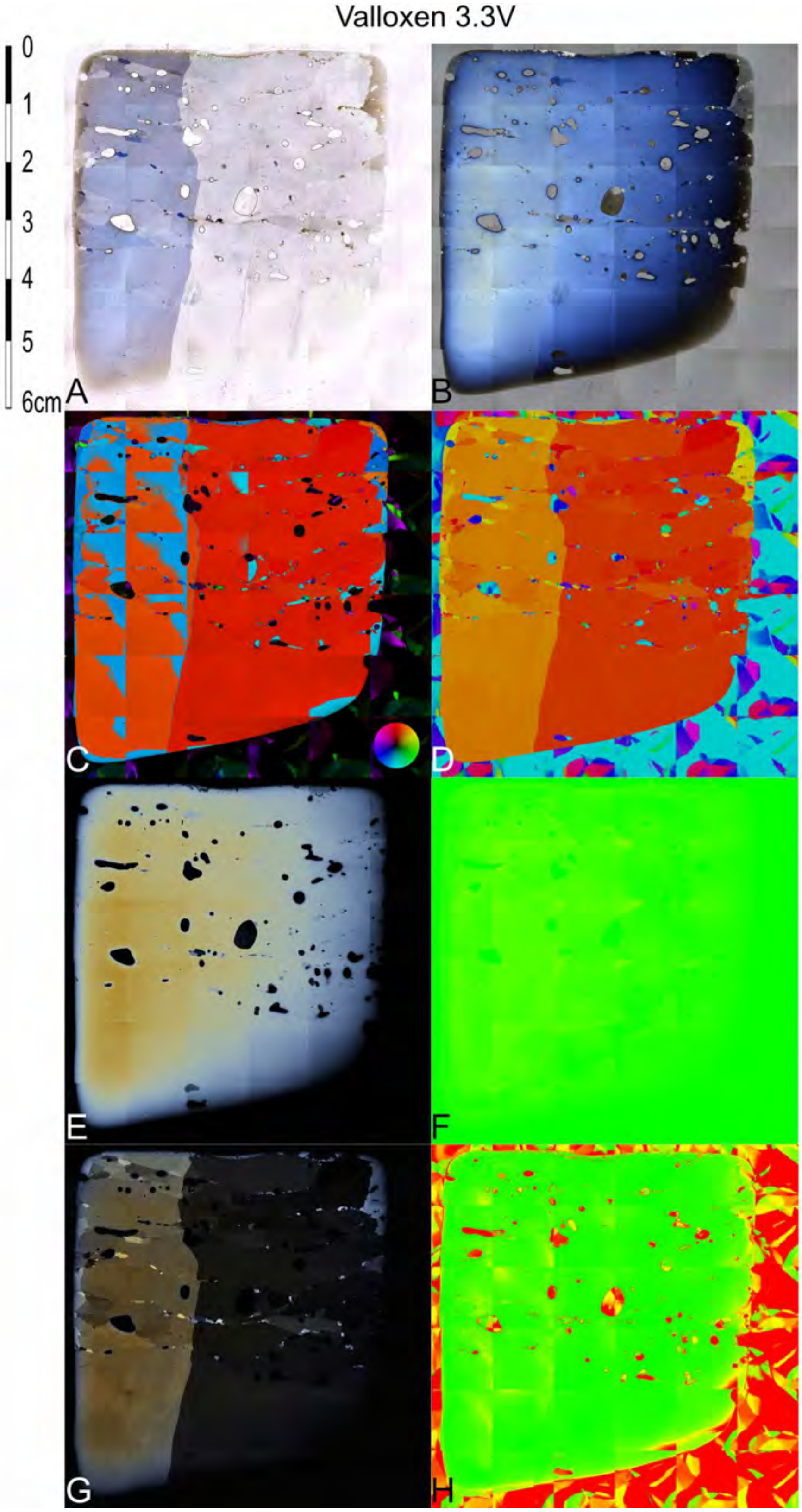

Figure 5.19: A) Plain polarized photo. B) Lambda 0 photo. C) c-axis orientation photo D) Flat trend c-axis orientation photo. E) Retardation photo. F) Retardation quality photo. G) Cross polarized photo. H) Geometric quality photo.

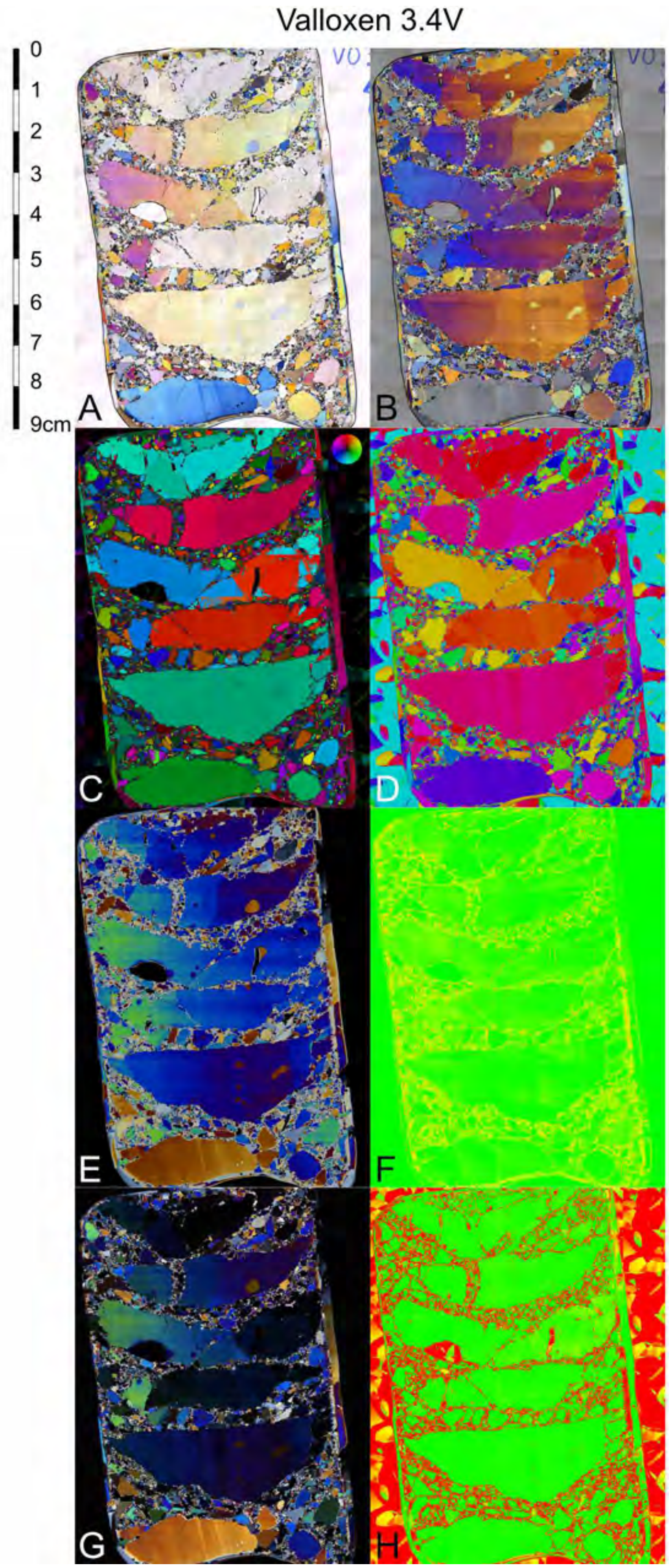

Figure 5.20: A) Plain polarized photo. B) Lambda 0 photo. C) c-axis orientation photo D) Flat trend c-axis orientation photo. E) Retardation photo. F) Retardation quality photo. G) Cross polarized photo. H) Geometric quality photo.

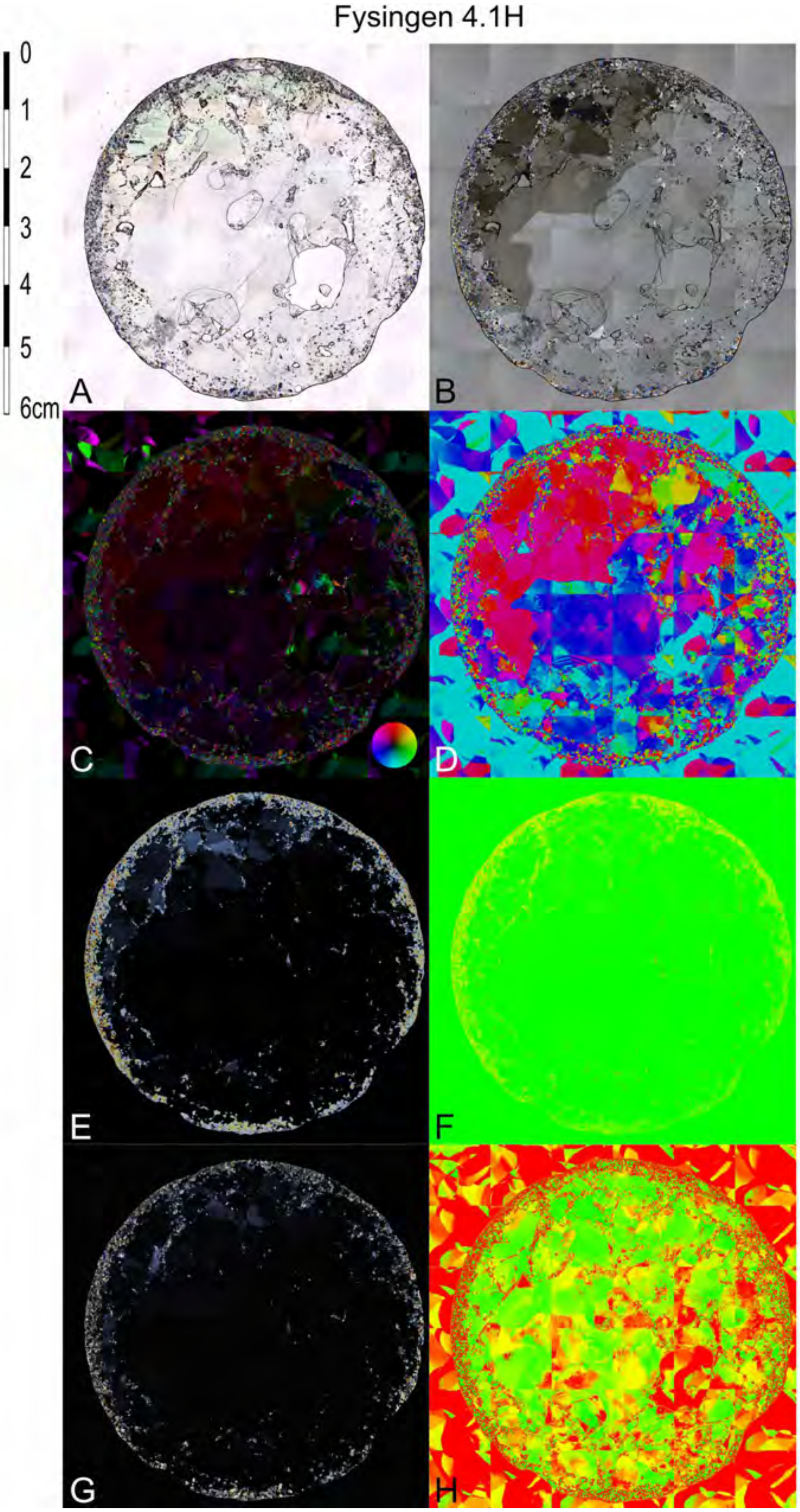

Figure 5.21: A) Plain polarized photo. B) Lambda 0 photo. C) c-axis orientation photo D) Flat trend c-axis orientation photo. E) Retardation photo. F) Retardation quality photo. G) Cross polarized photo. H) Geometric quality photo.

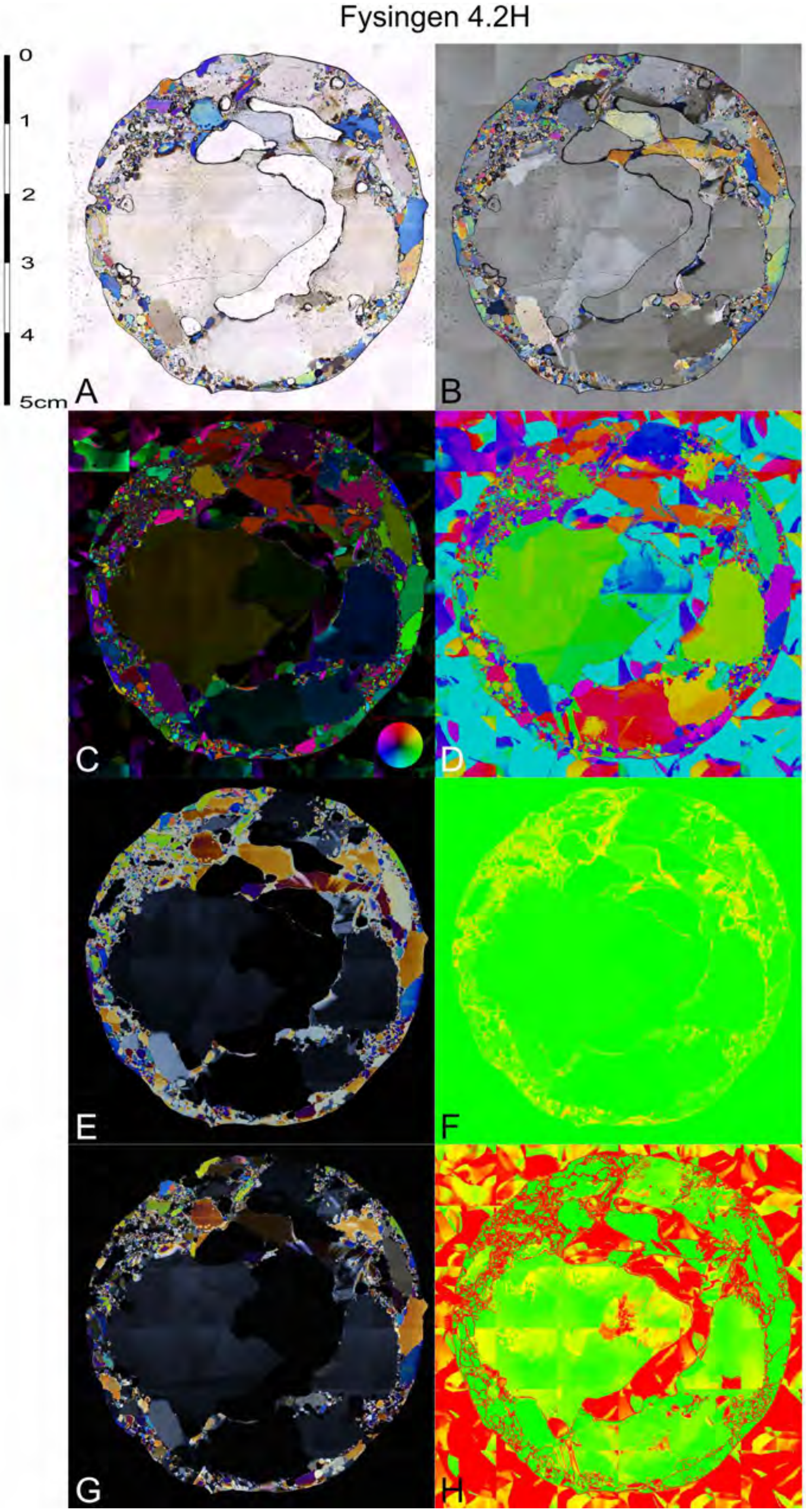

Figure 5.22: A) Plain polarized photo. B) Lambda 0 photo. C) c-axis orientation photo D) Flat trend c-axis orientation photo. E) Retardation photo. F) Retardation quality photo. G) Cross polarized photo. H) Geometric quality photo.

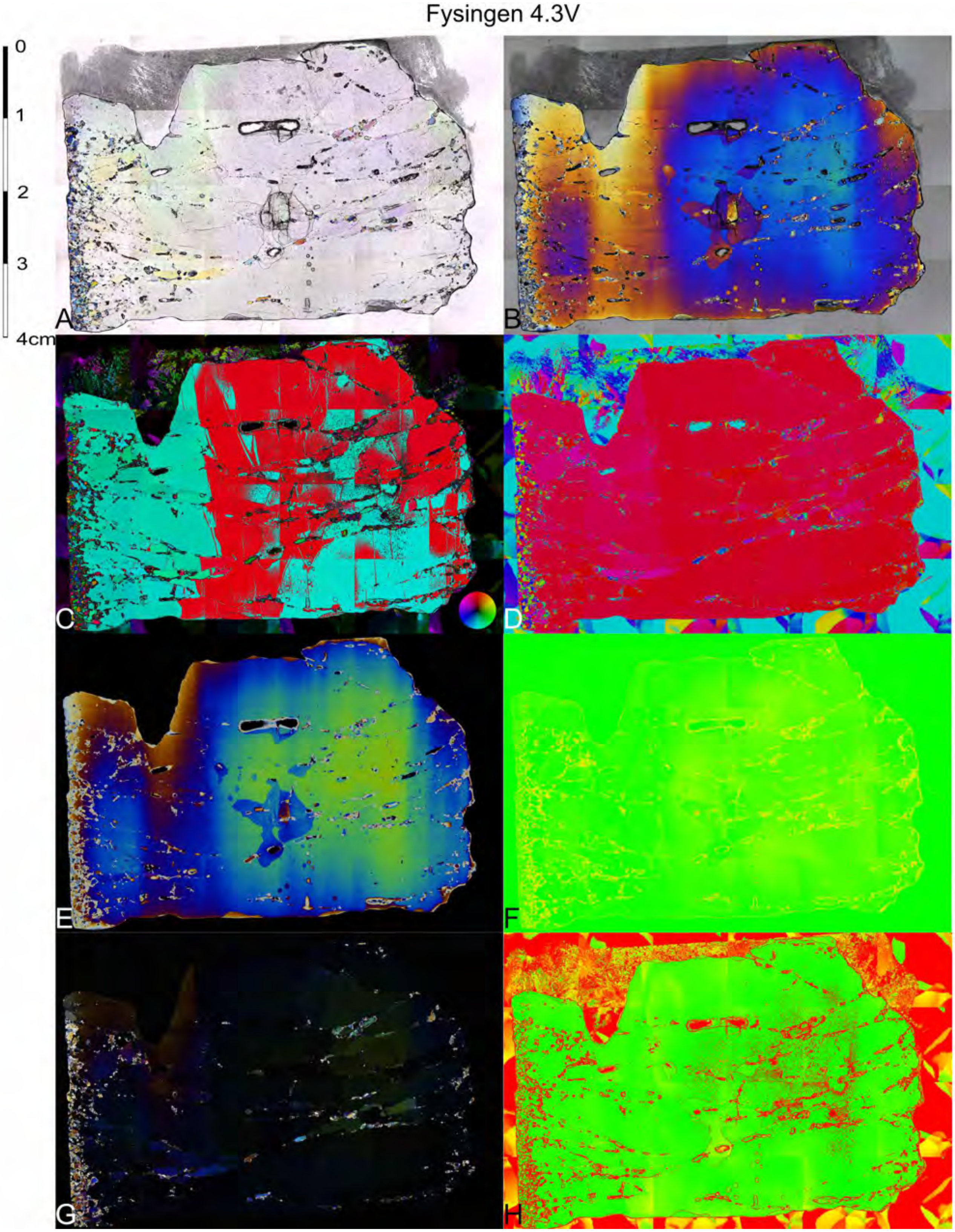

Figure 5.23: A) Plain polarized photo. B) Lambda 0 photo. C) c-axis orientation photo D) Flat trend c-axis orientation photo. E) Retardation photo. F) Retardation quality photo. G) Cross polarized photo. H) Geometric quality photo.

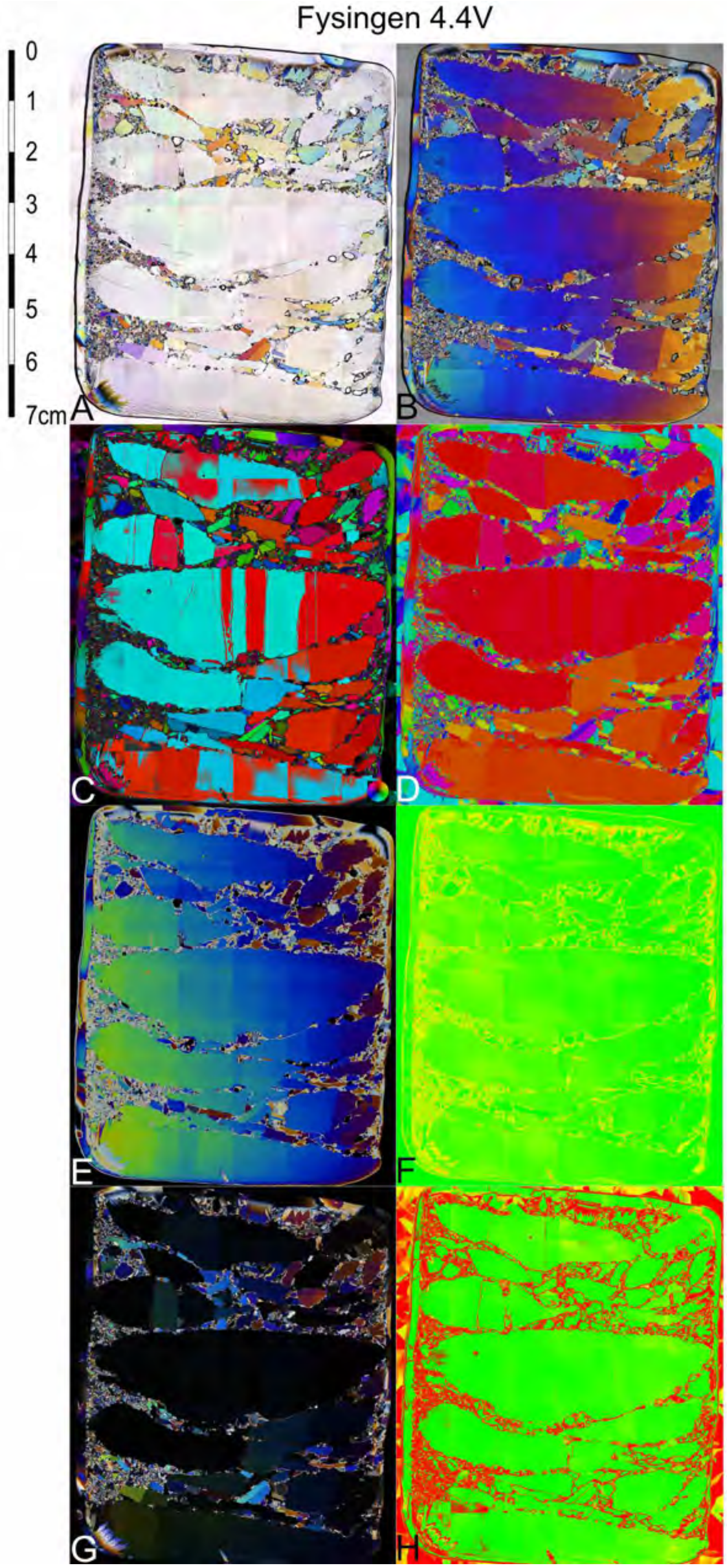

Figure 5.24: A) Plain polarized photo. B) Lambda 0 photo. C) c-axis orientation photo D) Flat trend c-axis orientation photo. E) Retardation photo. F) Retardation quality photo. G) Cross polarized photo. H) Geometric quality photo.

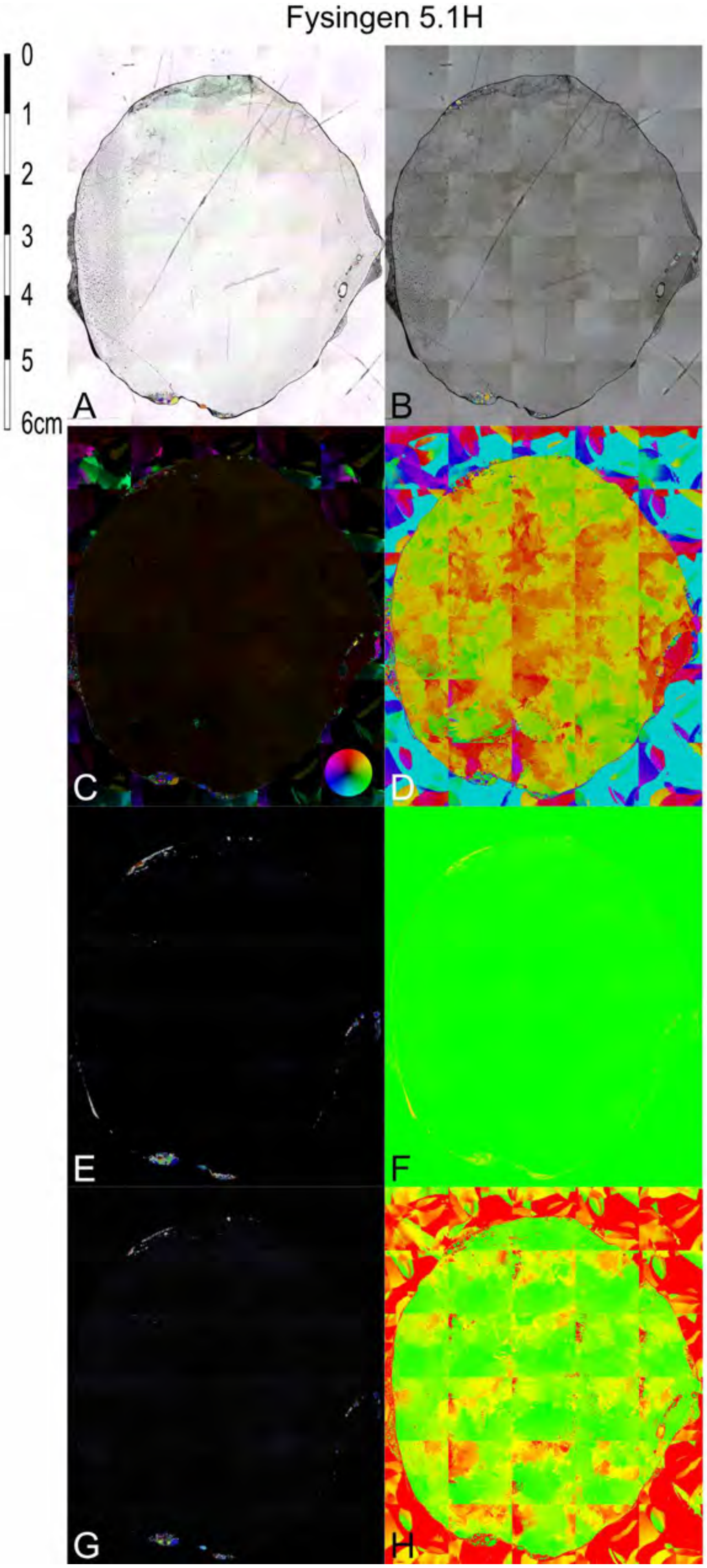

Figure 5.25: A) Plain polarized photo. B) Lambda 0 photo. C) c-axis orientation photo D) Flat trend c-axis orientation photo. E) Retardation photo. F) Retardation quality photo. G) Cross polarized photo. H) Geometric quality photo.

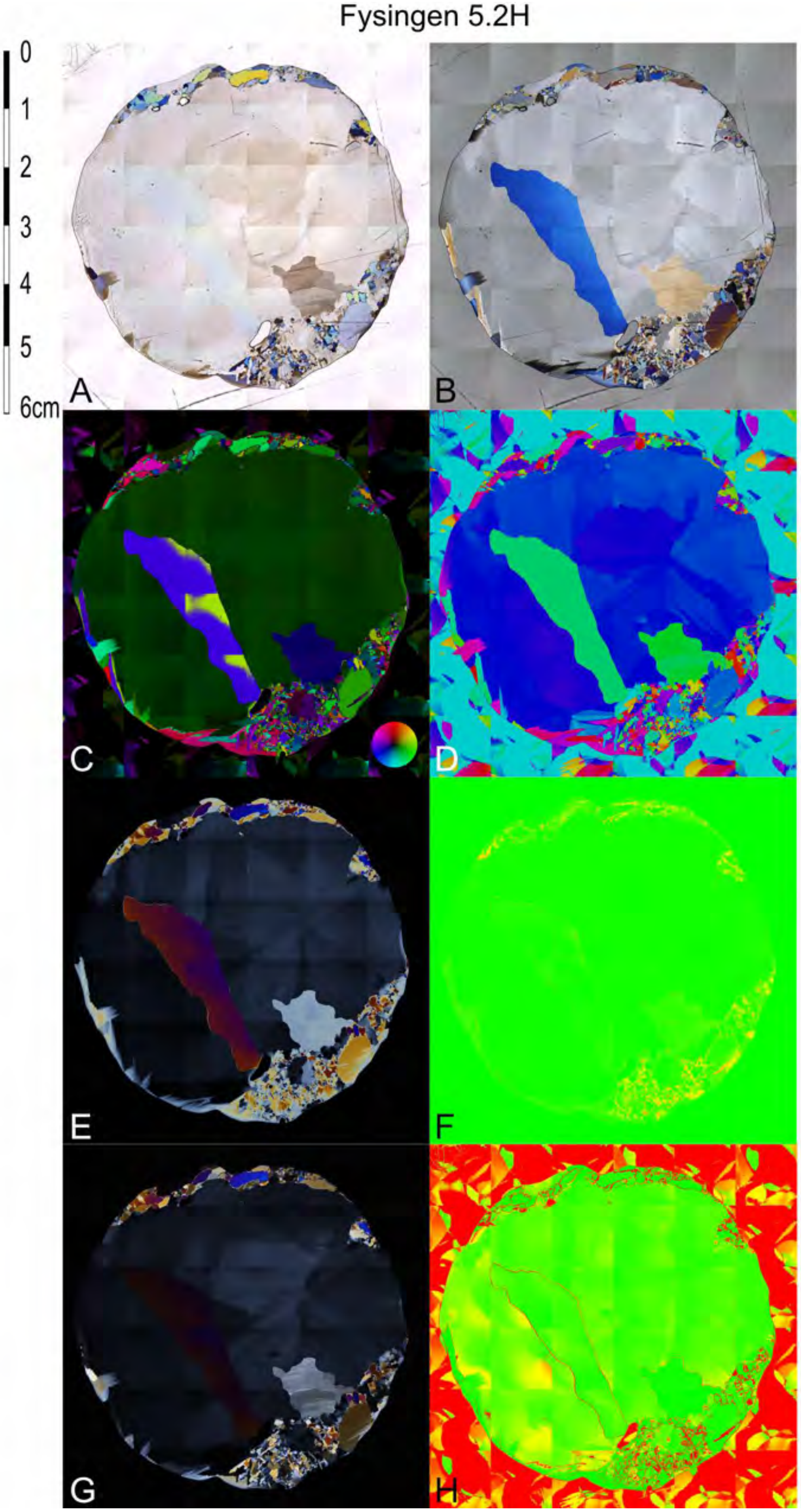

Figure 5.26: A) Plain polarized photo. B) Lambda 0 photo. C) c-axis orientation photo D) Flat trend c-axis orientation photo. E) Retardation photo. F) Retardation quality photo. G) Cross polarized photo. H) Geometric quality photo.

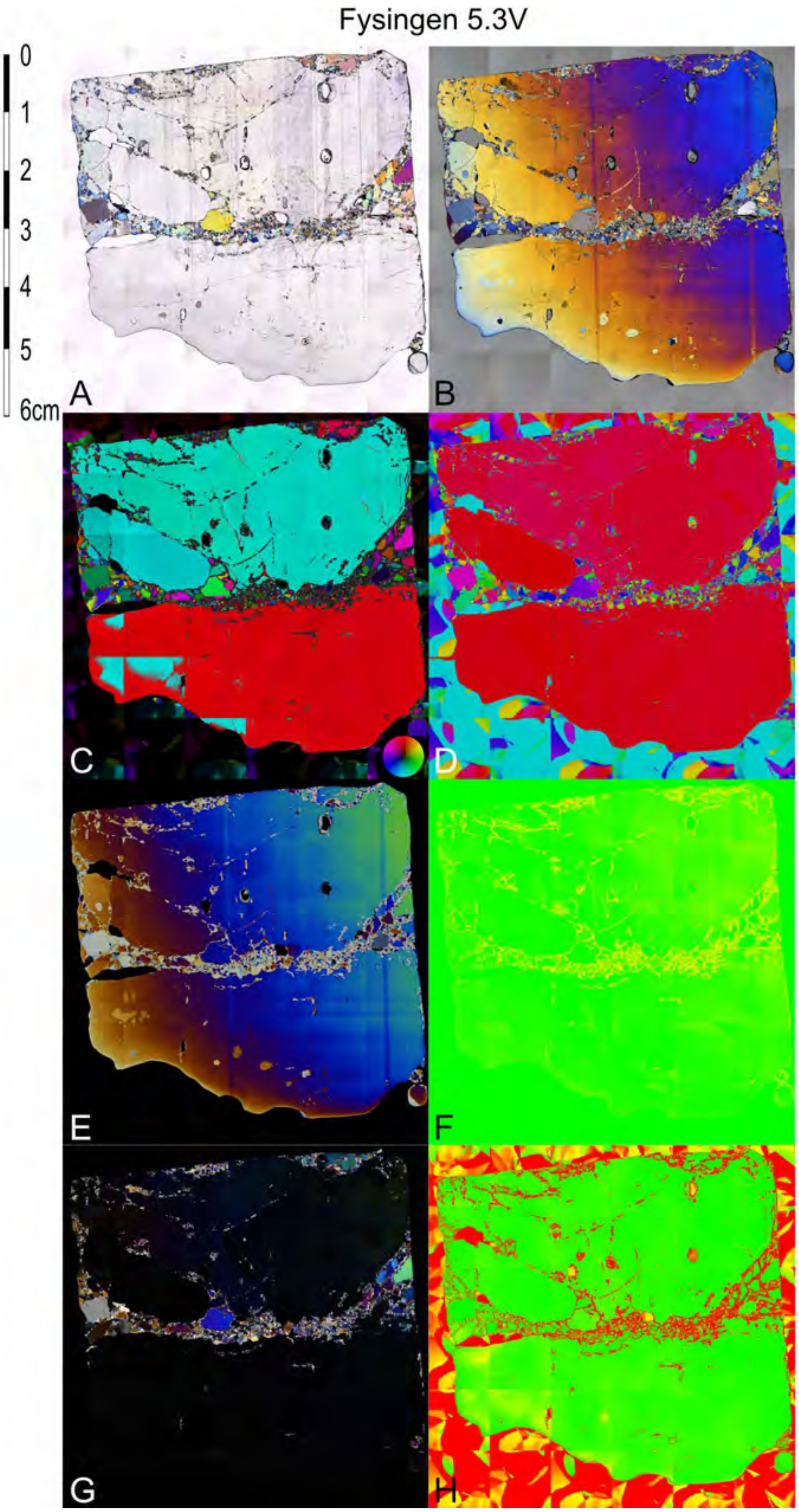

Figure 5.27: A) Plain polarized photo. B) Lambda 0 photo. C) c-axis orientation photo D) Flat trend c-axis orientation photo. E) Retardation photo. F) Retardation quality photo. G) Cross polarized photo. H) Geometric quality photo.

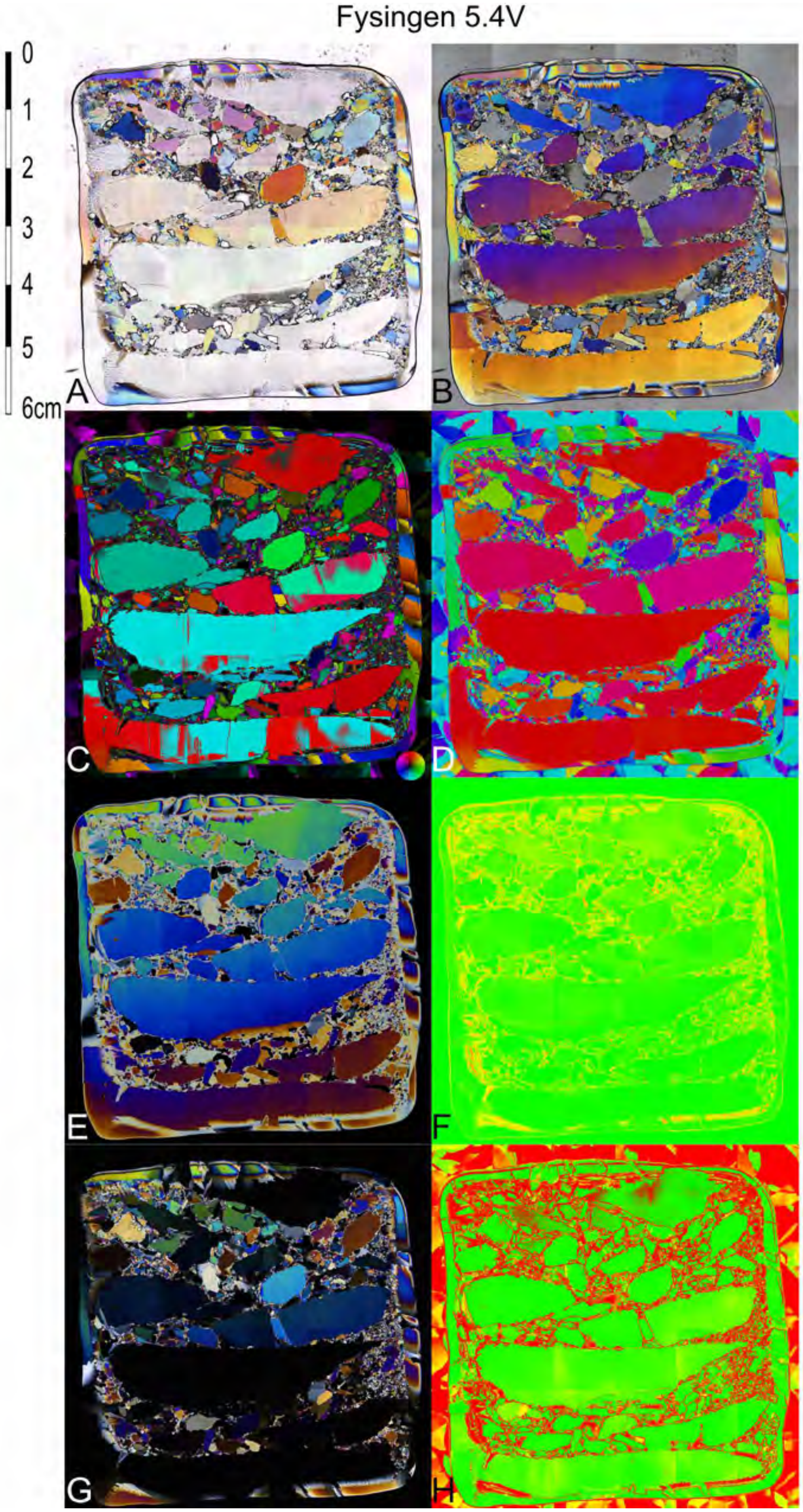

Figure 5.28: A) Plain polarized photo. B) Lambda 0 photo. C) c-axis orientation photo D) Flat trend c-axis orientation photo. E) Retardation photo. F) Retardation quality photo. G) Cross polarized photo. H) Geometric quality photo.